Experimental and numerical modelling of PVB foil

by

Barbora Hálková

A thesis submitted in partial fulfillment for the
degree of Master

in the
Faculty of civil engineering
Department of mechanics

January 2024

ČESKÉ VYSOKÉ UČENÍ TECHNICKÉ V PRAZE
Fakulta stavební
Thákurova 7, 166 29 Praha 6

ZADÁNÍ DIPLOMOVÉ PRÁCE

I. OSOBNÍ A STUDIJNÍ ÚDAJE

Příjmení: Hálková   Jméno: Barbora   Osobní číslo: 484410

Zadávající katedra: 11132 - katedra mechaniky

Studijní program: N3607 - Stavební inženýrství

Stud. obor/ spec.: 3607T009 - Konstrukce a dopravní stavby

II. ÚDAJE K DIPLOMOVÉ PRÁCI

Název diplomové práce: Experimentální a numerické modelování PVB folie

Název diplomové práce anglicky: Experimental and numerical modelling of PVB foil

Pokyny pro vypracování:
Experimentální stanovení frekven ního (asového) a teplotního chování PVB folie.
Numerická studie chování viskoelastického matriálového modelu založeného na zlomkových derivacích.
Posouzení statické a dynamické odezvy.
V p ípad asových možností, kalibrace navrženého viskoeleastického modelu na základ m ených dat.

Seznam doporučené literatury:
Skriptum "P etvá ení a porušování materiál ", auto i M. Jirásek a J. Zeman, ES VUT 2006 (dotisk 2010, 2. vydání 2012)
Skriptum "Numerické metody mechaniky", auto i Z. Bittnar a J. Šejnoha, VUT 1992

Jméno vedoucího diplomové práce: prof. Ing. Michal Šejnoha, Ph.D., DSc.

Datum zadání diplomové práce: 26. 9. 2023   Termín odevzdání DP v IS KOS: 8. 1. 2024
Údaj uveďte v souladu s datem v časovém plánu příslušného ak. roku

_____   _____
Podpis vedoucího práce   Podpis vedoucího katedry

III. PŘEVZETÍ ZADÁNÍ

Beru na vědomí, že jsem povinen vypracovat diplomovou práci samostatně, bez cizí pomoci, s výjimkou poskytnutých konzultací. Seznam použité literatury, jiných pramenů a jmen konzultantů je nutné uvést v diplomové práci a při citování postupovat v souladu s metodickou příručkou ČVUT „Jak psát vysokoškolské závěrečné práce" a metodickým pokynem ČVUT „O dodržování etických principů při přípravě vysokoškolských závěrečných prací".

_____   _____
Datum převzetí zadání   Podpis studenta(ky)

Declaration of Authorship

I, Barbora Hálková, declare that this thesis titled *Experimental and numerical modelling of PVB foil* and the work presented in it are my own. I confirm that:

- This work was done wholly or mainly while in candidature for a research degree at this University.

- Where any part of this thesis has previously been submitted for a degree or any other qualification at this University or any other institution, this has been clearly stated.

- Where I have consulted the published work of others, this is always clearly attributed.

- Where I have quoted from the work of others, the source is always given. With the exception of such quotations, this thesis is entirely my own work.

- I have acknowledged all main sources of help.

- Where the thesis is based on work done by myself jointly with others, I have made clear exactly what was done by others and what I have contributed myself.

Signed:

_____

Date:

_____

"The test of all knowledge is experiment.
Experiment is the sole judge of scientific truth."

Richard P. Feynman

CZECH TECHNICAL UNIVERSITY IN PRAGUE

Abstract

Faculty of civil engineering
Department of mechanics

Master's degree

by Barbora Hálková

Laminated glass is a composite material made of glass plates and polymer interlayers which ensure binding of the plates and have an important safety function. The most commonly used material for the interlayer is polyvinyl butyral (PVB), a polymer with significantly time and temperature dependent properties. Due to its time dependent behaviour the material can be described as viscoelastic. To describe a viscoelastic material the models consisting of elastic springs and viscous dashpots are used. The description can be also provided using the fractional viscoelasticity which bases on the theory of derivatives and integrals of non-integer order. Fractional viscoelasticity introduces another rheological element, a springpot. This element behaves as viscoelastic itself and its connection with more elastic or viscous elements opens the door to other, more advanced, models to describe viscoelastic materials. This thesis mainly focuses on the generalized Maxwell model in its standard as well as its fractional form. Behaviour of these two models is examined during the numerical analysis using the finite difference method for several loading cases and for varying model parameters. To describe the response of a real material the parameters of the models need to be calibrated. To this end, an extensive experimental program was executed. The viscoelastic behaviour of PVB was examined using the dynamic shear rheometer. The acquired measurements were then adopted in the optimization process of material parameters of both models to provide predictions which match the response of PVB observed experimentally.

Keywords

Viscoelasticity, fractional viscoelasticity, springpot, generalized Maxwell model, numerical analysis, experimental analysis, finite difference method, dynamic shear rheometer, polymer interlayer, polyvinyl butyral

ČESKÉ VYSOKÉ UČENÍ TECHNICKÉ V PRAZE

Abstrakt

Fakulta Stavební
Katedra mechaniky

Magisterský stupeň

Barbora Hálková

Lepené sklo je kompozitní materiál sestávající ze skleněných tabulí a polymerních mezivrstev, které jednak zajišťují spolupůsobení skel a jednak mají důležitou bezpečnostní funkci. Nejhojněji využívaným materiálem pro tyto mezivrstvy je polyvinyl butyral (PVB), polymer, jehož chování vykazuje výraznou časovou a teplotní závislost. Na základě těchto vlastností můžeme materiál klasifikovat jako vazkopružný. K popisu vazkopružného materiálu jsou běžně využívány modely složené z pružin a vazkých tlumičů. Další možnosti modelování přináší zlomková vazkopružnost založená na derivacích a integrálech neceločíselného řádu. Zlomková vazkopružnost zavádí další reologický prvek, springpot. Tento prvek se už ze své podstaty chová vazkopružně a jeho spojení s pružnými nebo vazkými články přináší další modely pro popis vazkopružných materiálů. V této práci se soustředíme zejména na Maxwellův řetězec, a to jak v jeho standardní, tak i zlomkové variantě. V rámci numerické analýzy využívající metodu konečných diferencí je zkoumáno chování těchto modelů v závislosti na zatížení a na proměnných parametrech modelů. Pro praktické využití je nutno tyto parametry naladit na základě skutečného materiálu. Za tímto účelem byla provedena série experimentů, při kterých bylo zkoumáno chování PVB s využitím dynamického smykového reometru. Na základě těchto experimentů proběhla optimalizace parametrů obou modelů tak, aby výsledné chování modelu co nejlépe vystihovalo experimentálně zjištěné chování PVB.

Klíčová slova

Vazkopružnost, zlomková vazkopružnost, springpot, zobecněný Maxwellův model, numerická analýza, experimentální analýza, metoda konečných diferencí, dynamický smykový reometr, polymerní mezivrstva, polyvinyl butyral

Acknowledgements

I would like to express my deepest gratitude to my supervisor, prof. Ing. Michal Šejnoha, Ph.D., DSc., for his help and patience throughout the process of researching and writing this thesis. The door to his office was always open to answer my questions and point me in the right direction whenever I hit a dead end.

Special thanks to Ing. Jaroslav Schmidt, Ph.D., for his advice and stimulating discussions on the fractional calculus and also for being my IT support whenever I broke my LaTeXcode.

I would like to extend my sincere thanks to Ing. Michal Beneš, Ph.D. for his guidance through the numerical part of this thesis.

I would also like to thank Ing. Jan Valentin, Ph.D. for his companionship throughout the experimental measurements and to doc. Ing. Jan Vorel, Ph.D. for his help with the mastercurve optimisation.

Last but not least, I would like to thank my family, especially my parents, my grandparents, my sister and my partner. Thank you for your unending support throughout my years of study. I would never be able to achieve so much without you by my side. Thank you for believing in me.

Contents

Symbols

General mathematics

e	Euler number
i	imaginary unit
Re	real part of complex number
Im	imaginary part of complex number
$\bullet^*$	complex variable
$\hat{\bullet}$	prescribed constant value
$\dot{\bullet}$	first time derivative
$\ddot{\bullet}$	second time derivative
D^α	α-th time derivative
I^α	α-th time integration
$H(t)$	Heaviside step function
$\Gamma(\alpha)$	Gamma function
$\delta(t)$	Dirac delta function
$\mathcal{L}\{f(t)\}(s),\ \bar{f}(s)$	Laplace transformation of function $f(t)$
$\mathrm{E}_{a,b}(z)$	Mittag-Leffler function

Viscoelasticity

t	time	s
$\bullet_\mathrm{e}$	value corresponding to elastic element	
$\bullet_\mathrm{v}$	value corresponding to viscous element	
$\bullet_0$	amplitude of the quantity	
$F(t)$	force	N
$u(t)$	displacement	m
k	stiffness	N/m
ν	constant of viscosity	N·s/m
τ_c	characteristic time	s
α	parameter of springpot	
ξ	parameter of springpot	

ω	angular frequency	rad/s
δ	phase shift	rad
$k'(\omega)$	storage stiffness	N/m
$k''(\omega)$	loss stiffness	N/m
$k^*(\omega)$	complex stiffness	N/m
$J(t)$	creep modulus	m/N
$R(t)$	relaxation modulus	N/m

Numerical analysis

Δt	size of time step	s
$\bullet^n$	nodal value	
$\bullet^0$	initial value	
$w_j(\alpha)$	weight function	
$q(t)$	internal parameter of Maxwell cell	N
$v(t)$	velocity	m/s
ω_0	natural frequency of undamped oscillation	rad/s
ω_D	natural frequency of damped oscillation	rad/s
ξ_D	damping ratio	
T_0	time period of undamped oscillation	s
T_D	time period of damped oscillation	s

Experimental analysis

h	sample thickness	mm
d	sample diameter	mm
$\tau(t)$	shear stress	Pa
$\gamma(t)$	shear strain	
η	constant of viscosity	Pa·s
G	shear modulus of elasticity	Pa
$G'(\omega)$	storage shear modulus	Pa
$G''(\omega)$	loss shear modulus	Pa
$G^*(\omega)$	complex shear modulus	Pa
T	temperature	°C
T_R	reference temperature	°C
$\alpha_\mathrm{R}(T)$	temperature shift factor	
$C_1,\ C_2$	parameters of WLF equation	

Chapter 1

Introduction

Polyvinyl butyral (PVB) is a polymeric material belonging to the group of thermoplastics. In civil engineering PVB is adopted in the manufacturing process of laminated glass panels. Laminated glass is a composite material consisting of at least two glass plates bound by polymeric interlayers. Both the plates and polymeric interlayer can vary in thicknesses and properties.

The glass itself is a brittle material with high compressive strength. Its tensile strength is significantly lower and when exceeded the brittle failure takes place. The glass breaks to shards leading to collapse of the structure. There is no residual strength of the material. The basic type of glass is a float glass. Its strength is the lowest and it breaks into large sharp pieces. Its properties can be improved with additional chemical or temperature toughening or tempering. These processes lead to improved tensile strength by increasing the compressive stress on the glass surface [20]. For the tempered glass the surface stress is very high. Because of that, it forms small cube-shaped pieces upon breakage. The tempered glass is used for example for windshields in automotive industry. However, the improved strength still does not change the brittle breakage of the glass and therefore the glass itself cannot be used for load-bearing structures.

Nevertheless, the appearance of glass is very attractive for architects. Glass structures (such as roofing, beams, columns or staircases) are still built, which calls for application of laminated glass. For laminated glass, even after the glass plate is broken, the shards stick to the interlayer. This behaviour reduces injuries caused by the shards. In addition, the unbroken glass plates remain load-bearing and there is no instant collapse of the structure. For this reason, laminated glass is also referred to as a safety glass. Glass plates in the composite can vary in thickness, mostly ranging between 3-25 mm [20].

As already mentioned, the interlayers have an important safety function. However, their importance also lies in binding the main load-bearing elements (i.e. the glass plates) together and ensuring their interaction. For a structure loaded by bending the interlayers are mostly loaded in shear. This is shown in Fig. 1.1 showing three cases of a bent laminated beam with a corresponding cross section for various levels of shear interaction. In case (a) the interlayer ensures a perfect interaction between the two layers. The cross section then behaves as full which leads to smaller deformations. On the other hand, case (c) represents the interlayer with zero shear stiffness suggesting no interaction between the plates. In this case, the cross section consists of two individual parts which (according to a moment of inertia) leads to greater deformation of the beam. In almost all practical

applications, however, the laminated glass behaves according to the intermediate case (b), where the interlayer ensures at least a partial interaction.
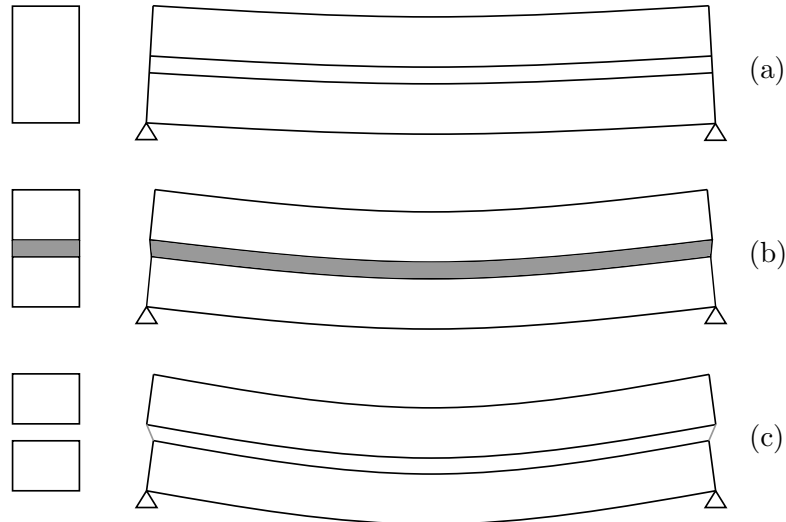

FIGURE 1.1: Layered beam in bending for varying interlayer properties (a) perfect, (b) partial, (c) zero shear interaction between layers

When designing laminated glass structures, the interaction between the glass plates is often neglected. However, to describe the behaviour of the composite properly, an accurate description of the response of a particular interlayer is needed. The interlayers are mostly made of polymers or cast resins. There is a whole range of materials used for laminated glass interlayers, e.g. ethylene-vinyl acetate (EVA), ionoplast SentryGlas (SG) or polyuretane (PUR). However, the most frequently used material is polyvinyl butyral (PVB) [20].

Polyvinyl butyral can be classified as a viscoelastic material. This means that its behaviour is neither purely elastic nor purely viscous. It behaves somewhere in between. Addressing its viscoleastic response, both experimentally and computationally, is the principal objective of this thesis organized as follows.

Chapter 2 introduces the theory of linear viscoelasticity in general for 1D problem. Several theoretical models are presented in this chapter considering either standard or fractional approach to describe viscoelastic behaviour. Owing to the computational part presented in Chapter 3, the formulation is presented in the force-displacement regime. This adds clarity to performed numerical simulations and consequently to the discussion of the achieved results considering both static and dynamic behavior.

Point out that no reference to a particular viscoelastic material has been made in the previous two chapters. In practical application, a proper tuning of a selected material model is needed. This in turn requires experimental measurements. To this end, an extensive experimental program carried out as part of this thesis is described in Chapter 4. Attention is limited to PVB material tested in a dynamic regime with the help of a dynamic shear rheometer. Because of the experimental setup, the expressions presented in Chapter 2 are considered in a plane of shear stress and strain. The results obtained from the experimental analysis are then used to calibrate the selected theoretical models.

The most important conclusion remarks are then summarized in Chapter 5.

Chapter 2

Theory of viscoelasticity

Rheology is the study of the time dependent material response under a set of loading and environmental conditions described in the stress-strain space [19]. The description of the material behaviour requires introduction of an appropriate material model. It is necessary to take into account that this model should approximate the behaviour of the material as close to its actual behaviour as possible while also considering the computational complexity.

The same material could be described by several material models and the most appropriate choice depends on the number of variables – the type of loading, time span, co-acting with other materials in the composite, characteristics of the surrounding environment, the size effect etc. For instance, if we want to model single glass plate in bending, the behaviour is efficiently described as elastic until brittle fracture [35]. On the other hand, let's consider the laminated glass composite consisting of glass plates and a polymer interlayer. When this composite is loaded in shear, the vast majority of the deformation happens inside the polymer interlayer and therefore the behaviour of the glass can be simplified, the glass plates can be modelled as a rigid material with no ability to deform.

The model commonly used to describe the behaviour of solid materials or structures is the linear elastic model, the main advantage of this model is its simplicity with the linear force-displacement proportionality. The elastic model is appropriate if the time-dependent phenomenon such as creep, relaxation or aging are negligible within the time period under consideration. However, it is not rare to use this simple model even in the problems where these phenomenon have a significant effect on the material response. To design structures the deviations from the elasticity are often introduced by various coefficients. We can mention, for example, the concrete structures, where the creep is significant in the long time horizon. Nevertheless, it is common to use models based on the theory of elasticity to design concrete structures and the influence of the creep is introduced by the reduction of Young's modulus (representing the stiffness of the material) for the long-term response.

These simplifications can be useful and can save us a lot of time. However, sometimes it is necessary to describe the material response more accurately. For example, when we use the simplified material model we are moving away from the real behaviour and therefore these models are usually more conservative and their use can lead to uneconomical design of the structure. This problem can be reduced if we use more complex material

models which are more complicated for computations, but which can provide more precise approximations of the material behaviour, closer to its actual response.

2.1 Viscoelasticity in general

The most simple generalization of linear elasticity for time-dependent behaviour of material is the linear viscoelasticity. This theory assumes the linear dependence of internal force on the history of displacement and the validity of the superposition principle, see Chapter 1 in [16]. All of the theory presented in this thesis is based on the principles of linear viscoelasticity.

As the name suggests, the behaviour of viscoelastic material is somewhere between the purely elastic and purely viscous, the material shows both the elastic and viscous properties. The viscoelastic behaviour is typical for some kinds of polymers, bitumen materials, concrete or for metals under very high temperatures. Viscoelastic materials can be also found as parts of a human body – e.g. the skin tissue that shows significant creep or aging [17].

To introduce a suitable model describing the viscoelastic behaviour we have two main options. The viscoelastic model can be made as a connection of several elastic and viscous cells together in series or in parallel. This approach is simpler according to the mathematical apparatus. However the model often requires adopting larger number of rheological cells to reach required accuracy. This leads to large number of unknown parameters that is need to be obtained based on material experiments. The second option is to introduce the fractional viscoelasticity. This approach allows us to use less extensive models with less parameters at the cost of more complex mathematical operations.

2.1.1 Limit cases of viscoelastic behaviour

As was already mentioned, the behaviour of the viscoelastic material lies somewhere between elastic and viscous. These two models – represented by an elastic spring and a viscous damper – stands for the limit cases of viscoelastic behaviour.
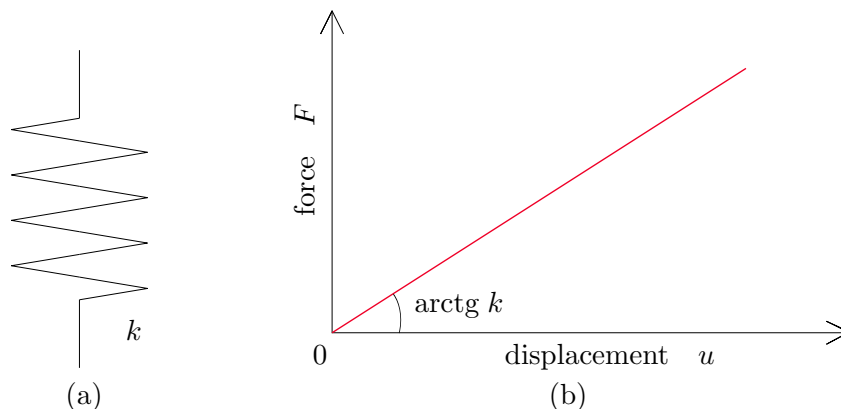

FIGURE 2.1: (a) Rheological scheme of linear spring, (b) force-displacement diagram

Model of linear spring

The elastic material model is commonly used for the description of solids. Elasticity is the ability of material to instantaneously respond to the applied force. Loading the elastic material with an instant force causes an instant displacement. The material returns to its original shape and size once the load is removed, the displacement is fully reversible [9].

For the purposes of this thesis we limit attention to the linear elasticity where the relationship between the force load F and the displacement u is linear. This proportionality is shown in Fig. 2.1 (b) and is mathematically described by the Hooke law. This well known constitutive law has the following form

$$F(t) = ku(t), \tag{2.1}$$

where k is the stiffness, the material constant which represents its resistance to loading in tension and in compression – the higher the stiffness of the material is, the lower is the displacement retrieved from the applied force of the same magnitude.

This material behaviour is represented by the model of linear spring – see the rheological scheme shown in Fig. 2.1 (a).
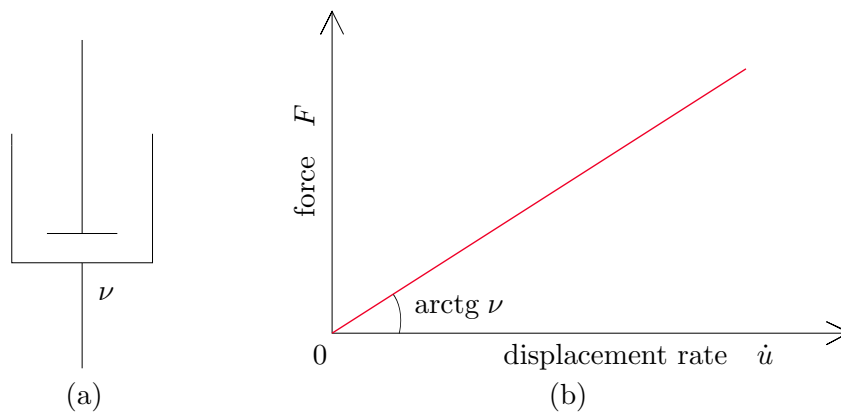
Model of viscous damper

FIGURE 2.2: (a) Rheological scheme of a dashpot (b) proportionality between force and displacement rate

The viscous behaviour, on the other hand, is typical for fluids – liquids or gases. The ideally viscous fluid, also known as a Newtonian fluid, shows the linear proportionality between force and displacement rate (i.e. velocity), see Fig. 2.2 (b). The application of an instant force causes an instant increase of the velocity which leads to a gradual increase of the displacement. Once the force is removed, the velocity becomes zero and the displacement remains constant since this moment. For a better idea of this behaviour see Fig. 2.3 showing the response of a viscous fluid loaded by a rectangular force. The viscous behaviour is described by the Newton law of viscosity in the following form

$$F(t) = \nu \dot{u}(t), \tag{2.2}$$

where $\dot{u}$ is the first time derivative of the displacement u, i.e. the displacement rate, and ν is the coefficient of viscosity which represents the ability of the fluid to flow. The higher this coefficient is, the stronger is the resistance of the fluid to flow under the applied force [12].
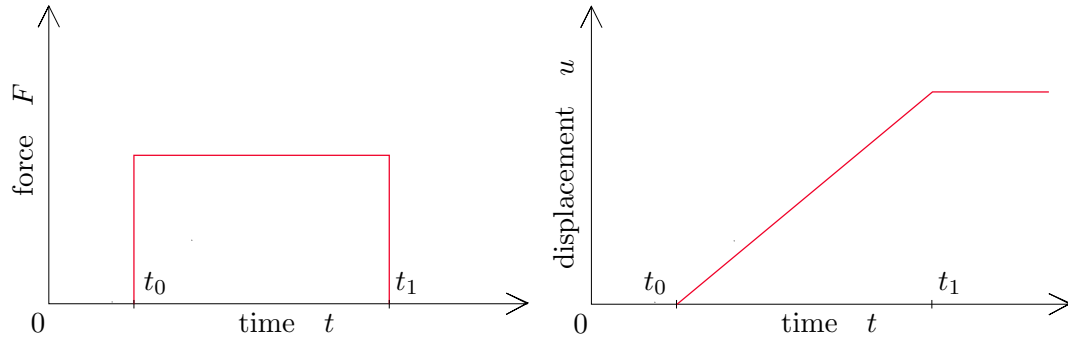

FIGURE 2.3: Behaviour of the viscous fluid under rectangular force load

The simple rheological model used to describe the viscous fluid is a dashpot – the purely viscous damper. The rheological scheme of the dashpot is shown in Fig. 2.2 (a).

2.1.2 Characteristic time

The viscoelastic response lies between the two limit cases. It depends on the material parameters but also on the considered time period. For a fast (short time) processes the material acts mostly as elastic while for a slow (long time) processes the viscous behaviour dominates [9]. The range between the fast and slow processes is given by the characteristic time depending on elastic and viscous properties of the material.

The characteristic time τ_{c} can be introduced in the following form

$$\tau_{\mathrm{c}} = \frac{\nu}{k}. \tag{2.3}$$

The physical meaning of it is shown in Fig. 2.4, considering a single spring and a single dashpot loaded by a constant force introduced suddenly at $t = 0$. As mentioned in the previous sections, the constant force causes the constant displacement of the spring and the constant displacement rate of the dashpot which leads to a linear increase of the displacement of the dashpot over time. The characteristic time indicates the moment when the viscous displacement reaches the same value as is the elastic one.
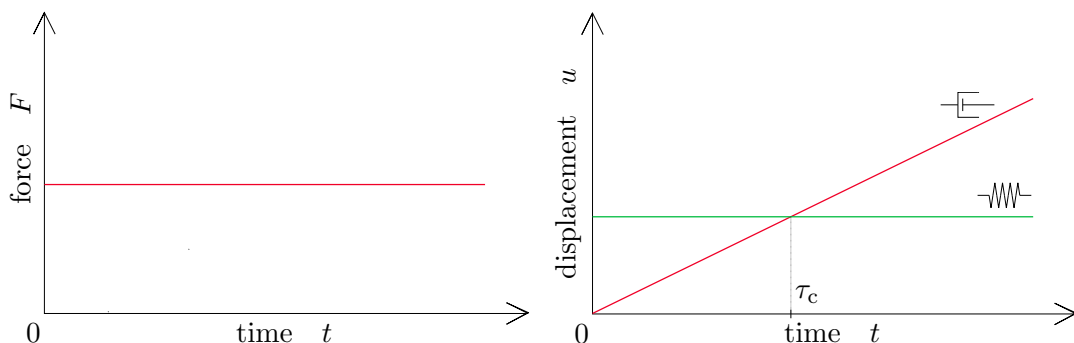

FIGURE 2.4: Physical meaning of characteristic time

Figure 2.4 also shows that for times $t \ll \tau_{\mathrm{c}}$ the elastic displacement is dominating while for $t \gg \tau_{\mathrm{c}}$ the behaviour is mainly affected by the material viscosity. If the viscosity of the material is higher, so is the characteristic time, the viscous behaviour is less significant. Therefore, it is obvious that the higher the characteristic time is, the closer the response is to elastic and vice versa.

2.1.3   Creep and relaxation

One of the characteristic phenomena for the viscoelastic materials is a creep. This term indicates the gradual increase of displacement while the force load remains constant over time. The relaxation, on the other hand, refers to a spontaneous decrease of the internal force under loading by a constant displacement.

Many materials also change their mechanical properties over time. The properties can improve, which can be described as the maturation, or worsen, which is associated with the degradation. These changes can be referred as aging of the material. We can mention concrete as an example of an aging material. Mechanical properties (e.g. the elastic modulus) of concrete improve over time due to the hydration processes. Therefore, the response of the concrete structure is stiffer the later the load is applied to the structure.

Our research focuses on the polyvinyl butyral (PVB), the polymeric material for which aging seems to be not significant. Therefore, this phenomena was neglected for the purposes of this thesis and the formulas presented in this text are valid for a non-aging material with the material parameters remaining constant over time.

Creep

As was already mentioned, creep is the phenomena causing a gradual increase of the displacement over time even if the internal force $\hat{F}$ remains constant. The evolution of the displacement $u(t)$ can be then written in the following form

$$u(t) = \hat{F} J(t), \tag{2.4}$$

where $J(t)$ denotes the creep modulus, the function of time describing the displacement response to a Heaviside load.
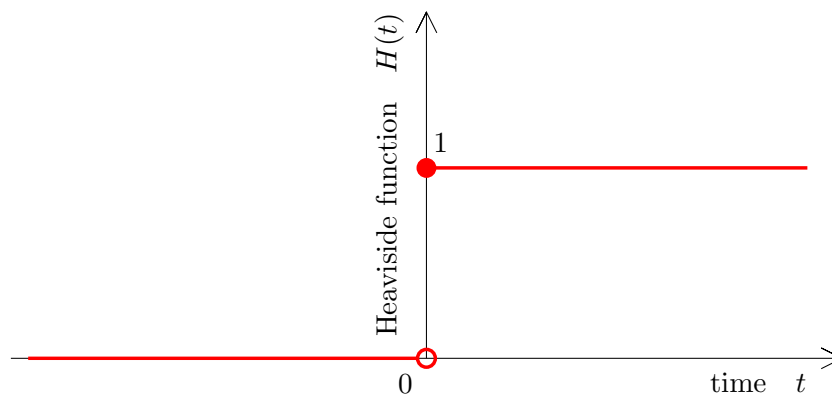

FIGURE 2.5: Heaviside step function

The Heaviside step function $H(t)$ is equal to zero for $t < 0$ and equal to one for $t \geq 0$. Mathematically the function is prescribed in the following form

$$H(t) = \begin{cases} 0 & \text{for} \quad t < 0 \\ 1 & \text{for} \quad t \geq 0 \end{cases} \tag{2.5}$$

and its graph is shown in Fig. 2.5. The Heaviside load then refers to a force $F = 1$ applied instantaneously in time $t = 0$ and remaining constant since then.

The creep modulus vary for each rheological model. For the model of a linear spring described by Hooke's law (recall Eq. (2.1)) the displacement can be expressed as

$$u(t) = \frac{1}{k} F(t). \tag{2.6}$$

For the Heaviside load $F(t) = H(t)$ we get the creep modulus of a linear spring in the following form

$$J(t) = \frac{1}{k} H(t). \tag{2.7}$$

It is obvious that the creep modulus is just a Heaviside function multiplied by a constant and therefore the elastic material shows no creep over time.

As for the dashpot, the displacement follows from Eq. (2.2) as

$$\dot{u}(t) = \frac{1}{\nu} F(t) \quad \rightarrow \quad u(t) = \frac{1}{\nu} \int_0^t F(t). \tag{2.8}$$

After the introduction of $F(t) = H(t)$ and of the initial condition $u(0) = 0$ (dashpot is not able to deform instantaneously) we get the creep modulus of the viscous dashpot model in the following form

$$J(t) = \frac{t}{\nu} H(t). \tag{2.9}$$

Compared to the spring, the whole displacement of the dashpot model is caused by the creep and the displacement grows to infinity.

Relaxation

The inverse phenomena to creep is the relaxation. It is referred as a gradual decrease of internal force even when the displacement $\hat{u}$ remains constant. The constitutive law can be expressed as

$$F(t) = \hat{u} R(t), \tag{2.10}$$

where $R(t)$ is the relaxation modulus, the force response to load by Heaviside displacement $u(t) = H(t)$.

Analogously to the previous paragraphs we can express the relaxation modulus of the spring and dashpot models. After the substitution of $u(t) = H(t)$ into Eq. (2.1) we get the relaxation modulus of the spring in the following form

$$R(t) = k H(t). \tag{2.11}$$

It is once again obvious that the elastic model is not affected by time-dependent phenomenon.

As we already know, the viscous model is not able to deform instantaneously. If we apply the Heaviside displacement to the dashpot model, the instant increase of displacement means there is an infinite displacement rate which leads to infinite internal force in this moment. After this moment the displacement remains constant, therefore the displacement rate is zero as well as the internal force. This progress of function $F(t)$ is called the Dirac delta function, which is shown in Fig. 2.6 and can be written mathematically as

$$\delta(t) = \begin{cases} 0 & \text{for} \quad t < 0 \\ \infty & \text{for} \quad t = 0 \\ 0 & \text{for} \quad t > 0. \end{cases} \tag{2.12}$$

This behaviour is not realistic and therefore dashpot does not allows the definition of the time dependent relaxation modulus.
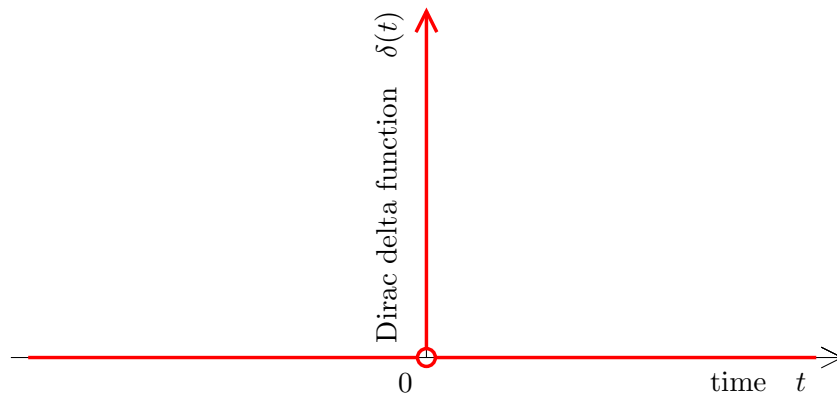

FIGURE 2.6: Dirac delta function

The knowledge of creep and relaxation moduli together with the superposition principle provide us a way to determine the response to time-varying load [16], [4]. Let's consider the instantaneous load by a force $\hat{F}$ applied at time $t = 0$ and followed by a continuous load development $F(t)$. The constitutive law can be then written as

$$u(t) = \hat{F} J(t) + \int_0^t \dot{F}(s) J(s) ds, \tag{2.13}$$

where $\dot{\bullet}$ denotes the first time derivative.

Analogously for the instantaneous displacement $\hat{u}$ applied at time $t = 0$ followed by a continuous development of displacement $u(t)$ we get

$$F(t) = \hat{u} R(t) + \int_0^t \dot{u}(s) R(s) ds. \tag{2.14}$$

2.1.4 Dynamic viscoelasticity

When the material is loaded with the constant static force the viscoelastic behaviour leads to increasing displacement over time due to the effect of creep. For the dynamic load, e.g. the oscillating force, the displacement is not necessarily increasing over time.

For the harmonic load the viscoelasticity of the material causes that the response is out of phase with the load.

Dynamic analysis of a material can provide information of its stiffness as well as viscosity and damping effect. This is the reason why properties of viscoelastic materials are often examined with the use of dynamic experiments. It is usual to load the sample with a harmonic force or displacement while both the elastic and viscous response are analyzed [9]. The study presented in this thesis used dynamical testing as well. Broader description of the experimental analysis is provided in Chapter 4.

Harmonic load can be prescribed as sinusoidal in the following form

$$u(t) = u_0 \sin(\omega t), \tag{2.15}$$

where u_0 is the amplitude of the displacement load and ω is the loading angular frequency. With the assumption of small displacements within the range of linear viscoelasticity, the response to the harmonic load is also harmonic with the same angular frequency but shifted by the phase shift δ [5]. The response has the following form

$$F(t) = F_0 \sin(\omega t + \delta). \tag{2.16}$$

The phase shift is the effect of viscous behaviour. In the case of purely elastic material there is no phase shift, $\delta = 0$ and the response is in phase with the load. On the other hand, for purely viscous material the response is 90° out of phase with the load, the phase shift $\delta = \pi/2$. This is shown in Fig. 2.7 (b), the blue line indicates sinusoidal displacement load and the other lines indicate response – grey dashed for elastic, grey dotted for viscous and red for general viscoelastic.
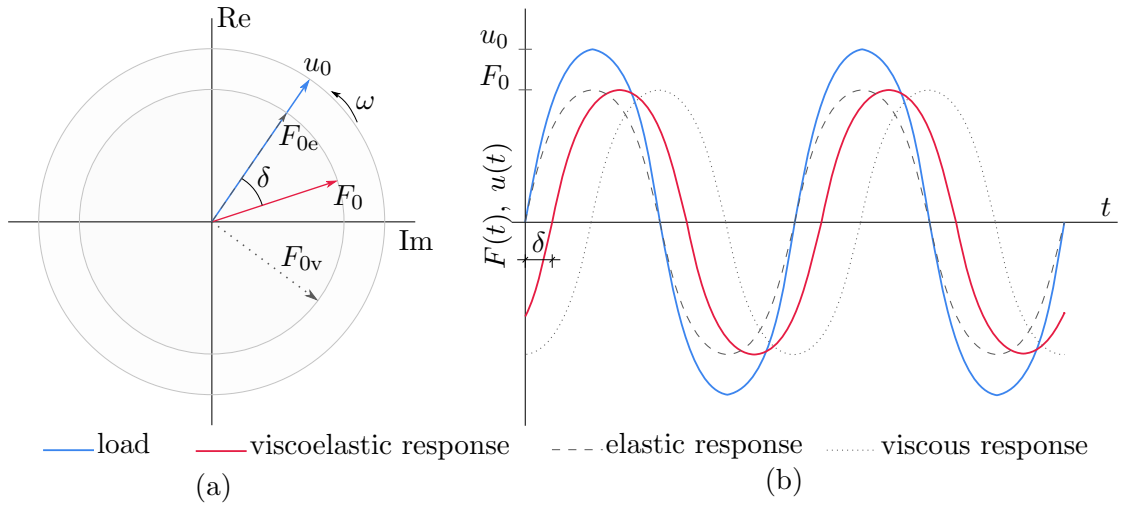

FIGURE 2.7: Elastic, viscous and viscoelastic response to dynamic load
(a) harmonic loading in complex plane (b) projection onto the real axis

The property of trigonometric functions $\sin(a + b) = \sin(a)\cos(b) + \cos(a)\sin(b)$ allows us to rewrite Eq. (2.16) as

$$F(t) = F_0 \cos\delta \sin(\omega t) + F_0 \sin\delta \cos(\omega t). \tag{2.17}$$

Because the phase shift δ is constant in time, $\sin(\delta)$ and $\cos(\delta)$ are constants as well. Let's examine the right hand side of this equation. The first term with the amplitude $F_e = F_0 \cos \delta$ is oscillating in phase with the load, it corresponds to the elastic response. As we know, for trigonometric functions it holds that $\cos(x) = \sin(x + \pi/2)$. Therefore the second term of the equation indicates the response shifted by $90°$ to the load and it corresponds to the viscous response with the amplitude $F_v = F_0 \sin \delta$.

Now it is appropriate to prescribe the storage and loss stiffness as

$$k' = \frac{F_0}{u_0} \cos \delta = \frac{F_e}{u_0},$$

$$k'' = \frac{F_0}{u_0} \sin \delta = \frac{F_v}{u_0}, \tag{2.18}$$

where k' denotes so called storage stiffness corresponding to the elastic part of the behaviour with the energy stored in the material. The loss stiffness k'' corresponds to the viscous part of the behaviour with the energy lost by the effect of damping.

Introducing Eq. (2.18) into Eq. (2.17) provides the constitutive law for the dynamic loading in the form

$$F(t) = u_0 k' \sin(\omega t) + u_0 k'' \cos(\omega t). \tag{2.19}$$

In the following sections the storage and loss stiffnesses are derived for all presented models. To derive these analytical expressions it is beneficial to employ complex numbers.

See Fig. 2.7 (a) showing the complex vectors of the lengths u_0 (blue) and F_0 (red) rotating with the angular frequency ω. The limit cases for viscoelastic response are shown as well – F_{0e} (gray dashed) corresponding to elastic behaviour and F_{0v} (gray dotted) representing the viscous behaviour. The projection of these vectors into the real axis (in the figure marked as Re) corresponds to the harmonic functions shown in Fig. 2.7 (b). This harmonic functions can be defined as a phasor formulation in the following form

$$u(t) = u_0^* e^{i\omega t},$$
$$F(t) = F_0^* e^{i\omega t}, \tag{2.20}$$

where $\bullet^*$ denotes the complex variable, e is the Euler's constant and i is the imaginary unit. F_0^* and u_0^* are amplitudes of the harmonic oscillation in the complex plane.

The complex stiffness k^* can be then defined as

$$k^* = \frac{F_0^*}{u_0^*}. \tag{2.21}$$

The relationship between the storage, loss and complex stiffness has the following form
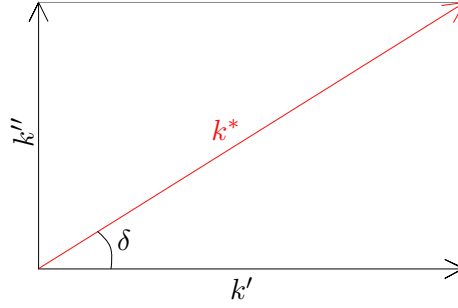
$$k^* = k' + i k''. \tag{2.22}$$

FIGURE 2.8: Illustrative meaning of complex stiffness

Figure 2.8 shows the magnitude of the complex stiffness which is given by

$$|k^*| = \sqrt{(k')^2 + (k'')^2}. \tag{2.23}$$

Introduction of Eq. (2.18) into Eq. (2.22) then leads to the following expression

$$k^* = \frac{F_0}{u_0} \cos \delta + \mathrm{i} \frac{F_0}{u_0} \sin \delta, \tag{2.24}$$

which can be rewritten using the Euler formula $\mathrm{e}^{ix} = \cos x + \mathrm{i} \sin x$ [37] as

$$k^* = \frac{F_0}{u_0} \mathrm{e}^{\mathrm{i}\delta}. \tag{2.25}$$

The storage and loss stiffnesses can be derived from the complex stiffness by separating the real (Re) and imaginary (Im) parts as

$$\begin{aligned} k' &= \mathrm{Re}(k^*), \\ k'' &= \mathrm{Im}(k^*). \end{aligned} \tag{2.26}$$

Remark that the storage, loss and complex stiffnesses (i.e. the dynamic stiffnesses) are not constants in general. The following sections will show that the dynamic stiffnesses are dependent on angular frequency. The experimental analysis presented in Chapter 4 determines their dependence on temperature as well.

2.1.4.1 Complex stiffness of spring and dashpot

For the elastic material the response is in phase with the load, the phase shift $\delta = 0$. Therefore, from Eq. (2.18) we see that the loss stiffness k'' of the elastic spring is equal to zero. The complex stiffness k^* is then equal straightly to the storage stiffness k' in the following form

$$k^* \equiv k' = \frac{F_e}{u_0} = \frac{k u_0}{u_0} = k. \tag{2.27}$$

The dynamic response of purely viscous material is out of phase with the load, the phase shift $\delta = \pi/2$. Equation (2.18) then shows that for the viscous damper the storage stiffness k' is zero so the complex stiffness k^* consists of the imaginary part only.

By introducing Eq. (2.2) into Eq. (2.20) we get

$$F(\omega) = \nu \dot{u}^*(\omega) = \mathrm{i}\omega\nu u_0^* \mathrm{e}^{\mathrm{i}\omega t} = F_0^* \mathrm{e}^{\mathrm{i}\omega t}. \tag{2.28}$$

Using Eq. (2.21) the complex stiffness of viscous dashpot can be expressed in the following form

$$k^*(\omega) \equiv \mathrm{i}k''(\omega) = \frac{F_0^*}{u_0^*} = \frac{\mathrm{i}\omega\nu u(\omega)}{u(\omega)} = \mathrm{i}\omega\nu = \mathrm{i}\frac{F_0}{u_0}. \tag{2.29}$$

2.2 Fractional viscoelasticity

If we want to describe viscoelastic material with its time-dependent behaviour, we do not suffice with purely elastic or purely viscous model. One of the possible approaches is to introduce more complicated models consisting of more springs and dashpots connected in series or in parallel. It is usually true that increasing the number of elements improves accuracy of the model prediction but at the expense of increasing number of model parameters (i.e. the stiffness or viscosity coefficient for each element). This approach is described in more detail in the Section 2.3.

Another approach for the description of the viscoelastic material is the use of fractional viscoelasticity which is based on the principles of fractional calculus, the theory of integrals and derivatives of non-integer order [28]. The basic relationships needed for better understanding of the following text are presented in Appendix A.

2.2.1 Springpot element

Fractional viscoelasticity introduces the springpot, rheological element that behaves as viscoelastic on its own. The rheological scheme of this fractional element is shown in Fig. 2.9.
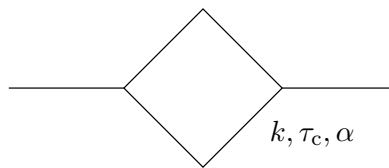

FIGURE 2.9: Rheological scheme of springpot element

To get an idea of the behaviour of the springpot, let us first recall the behaviour of spring and dashpot. The elastic spring is characteristic by its proportionality between the applied force and the displacement. The dashpot then shows the proportionality between the applied force and first time derivative of displacement, i.e. the displacement rate. The behaviour of the springpot element, as its name suggests, lies somewhere between the spring and the dashpot. The constitutive law for the springpot element has the following form

$$F(t) = \xi D^\alpha u(t), \tag{2.30}$$

where ξ and α are the parameters of the springpot. D^α denotes the α-th time derivative, generalization of derivative $d^n/(dt)^n$ for non-integer n [21]. The springpot shows

proportionality between applied force and the α-th derivative of the displacement while $\alpha \in \mathbb{R}$. The parameter ξ can be rewritten with the use of the characteristic time as

$$\xi = k\tau_{\mathrm{c}}^{\alpha} \tag{2.31}$$

and by the substitution into Eq. (2.30) we get

$$F(t) = k\tau_{\mathrm{c}}^{\alpha} D^{\alpha} u(t), \tag{2.32}$$

which is convenient for a better interpretation of parameters of the springpot element.

For the application in the theory of viscoelasticity the limit cases of the behaviour have to be respected. These limit cases are given by the purely elastic and purely viscous behaviour and they are obvious from Eq. (2.32). For $\alpha = 0$ we get the following equation

$$F(t) = k\tau_{\mathrm{c}}^{0} D^{0} u(t) = ku(t), \tag{2.33}$$

because $\tau_{\mathrm{c}}^{0} = 1$. Equation (2.33) is identical to Eq. (2.1) describing the behaviour of a purely elastic material. For $\alpha = 1$ we recieve

$$F(t) = k\tau_{\mathrm{c}}^{1} D^{1} u(t) = \nu \dot{u}(t), \tag{2.34}$$

the purely viscous behaviour as was introduced in Eq. (2.2).

These limit cases show that we are in the range between the zero time derivative and the first time derivative of the displacement. Therefore for our purposes in the application in viscoelasticity we further restrict the values of the springpot parameter α to $\alpha \in \langle 0, 1 \rangle$.

2.2.1.1   Creep and relaxation moduli of the springpot

To obtain the creep modulus we load the element with a Heaviside force.

The displacement can be expressed from Eq. (2.32) as

$$u(t) = I^{\alpha} \frac{F(t)}{k\tau_{\mathrm{c}}^{\alpha}} = \frac{1}{k\tau_{\mathrm{c}}^{\alpha}} I^{\alpha} F(t), \tag{2.35}$$

where I^{α} denotes the integral operator of the α-th order. The Riemann-Liouville fractional integral, see Eq. (A.14), can be substituted for I^{α}. Considerig the Heaviside load as $F(t) = H(t)$ we get the creep modulus of the springpot in the form

$$J(t) = \frac{1}{k\tau_{\mathrm{c}}^{\alpha}} \frac{1}{\Gamma(\alpha)} \int_{0}^{t} (t - s)^{\alpha - 1} H(s) \mathrm{d}s, \tag{2.36}$$

where $\Gamma(\alpha)$ is the Gamma function (for further description see Appendix A). After integration we get

$$J(t) = \frac{1}{k\alpha\Gamma(\alpha)} \left(\frac{t}{\tau_{\mathrm{c}}} \right)^{\alpha} H(t). \tag{2.37}$$

Exploiting the Gamma function property $\Gamma(x + 1) = x\Gamma(x)$ (Eq. (A.7)) simplifies the above expression as

$$J(t) = \frac{1}{k\Gamma(\alpha + 1)} \left(\frac{t}{\tau_{\mathrm{c}}} \right)^{\alpha} H(t). \tag{2.38}$$

The creep modulus of the springpot is dependent on the springpot parameter α. This dependence is shown in Fig. 2.10 also with the limit cases of the elastic and viscous behaviour. As the value of α increases to one, the response becomes closer to the response of the dashpot (pink line in the figure). In contrast, if we consider the value decreasing to zero, the response is getting closer to the elastic behaviour (brown line).
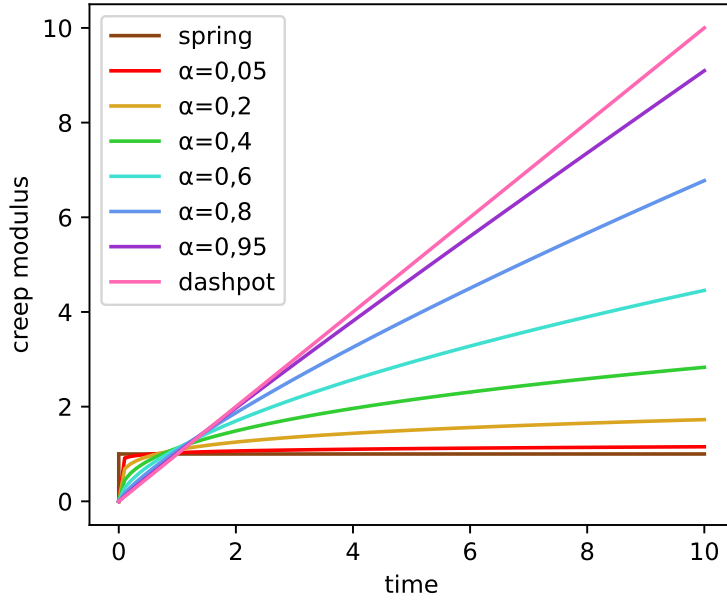

FIGURE 2.10: Creep modulus of springpot in dependence on parameter α

The limit cases of the parameter α can be inspected analytically as well. For $\alpha = 0$ we get

$$J(t) = \frac{1}{k\Gamma(1)}\left(\frac{t}{\tau_{\mathrm{c}}}\right)^0 H(t) = \frac{1}{k}H(t), \tag{2.39}$$

which corresponds to the creep modulus of the elastic spring derived in Eq. (2.7). For the limit case $\alpha = 1$ it stands

$$J(t) = \frac{1}{k\Gamma(2)}\left(\frac{t}{\tau_{\mathrm{c}}}\right) H(t) = \frac{t}{\nu}H(t), \tag{2.40}$$

which is the same as for the dashpot, Eq. (2.9).

Substitution of the Caputo fractional derivative (Eq. (A.16)) into Eq. (2.32) provides the constitutive law in the form

$$F(t) = \frac{k\tau_{\mathrm{c}}^\alpha}{\Gamma(\lceil\alpha\rceil - \alpha)}\int_0^t (t-s)^{\lceil\alpha\rceil - \alpha - 1} D^{\lceil\alpha\rceil} u(s)\mathrm{d}s, \tag{2.41}$$

where $\lceil\alpha\rceil$ is the ceiling function. For $\alpha \in \langle 0, 1\rangle$, i.e. $\lceil\alpha\rceil = 1$, and the Heaviside displacement load $u(t) = H(t)$ we get the following expression, recall Eq. (A.17),

$$R(t) = \frac{k\tau_{\mathrm{c}}^\alpha}{\Gamma(1 - \alpha)}\int_0^t (t-s)^{-\alpha}\frac{\mathrm{d}}{\mathrm{d}s}H(s)\mathrm{d}s. \tag{2.42}$$

For further integration we use the following properties of the Heaviside function and the Dirac delta function [28]

$$\frac{\mathrm{d}}{\mathrm{d}t}H(t) = \delta(t),$$ (2.43a)

$$\int_b^a f(t)\delta(t - t_0)dt = f(t_0).$$ (2.43b)

Their substitution into Eq. (2.42) leads to

$$R(t) = \frac{k\tau_c^\alpha}{\Gamma(1 - \alpha)}\int_0^t (t - s)^{-\alpha}\delta(s)\mathrm{d}s = \frac{k\tau_c^\alpha}{\Gamma(1 - \alpha)}(t - 0)^{-\alpha}.$$ (2.44)

Finally we obtain the relaxation modulus of the springpot as

$$R(t) = \frac{k}{\Gamma(1 - \alpha)}\left(\frac{t}{\tau_c}\right)^{-\alpha}H(t).$$ (2.45)

We can show that the same result can be obtained if we use the Riemann-Liouville definition of fractional derivative introduced in Appendix A by Eq. A.18. Substituting this formulation for D^α in Eq. (2.32) provides the constitutive law written in the form

$$F(t) = \frac{k\tau_c^\alpha}{\Gamma(\lceil\alpha\rceil - \alpha)}D^{\lceil\alpha\rceil}\int_0^t (t - s)^{\lceil\alpha\rceil - \alpha - 1}u(s)\mathrm{d}s.$$ (2.46)

Now we recall Eq. (A.20), because for the Heaviside displacement load $u(t) = H(t)$ and $\alpha \in \langle 0, 1 \rangle$, i.e. $\lceil\alpha\rceil = 1$, Eq. (2.46) becomes

$$R(t) = \frac{k\tau_c^\alpha}{\Gamma(1 - \alpha)}\frac{\mathrm{d}}{\mathrm{d}t}\int_0^t (t - s)^{-\alpha}H(s)\mathrm{d}s.$$ (2.47)

Since we integrate from zero, the Heaviside function is constant, $H(t > 0) = 1$. Therefore, after further integration we get

$$R(t) = \frac{k\tau_c^\alpha}{\Gamma(1 - \alpha)}\frac{\mathrm{d}}{\mathrm{d}t}\frac{1}{1 - \alpha}t^{1-\alpha}.$$ (2.48)

The relaxation modulus of the springpot is now simply obtained as

$$R(t) = \frac{k}{\Gamma(1 - \alpha)}\left(\frac{t}{\tau_c}\right)^{-\alpha}H(t).$$ (2.49)

We see that the expression is the same as Eq. (2.45) obtained via the Caputo fractional derivative. The derivation procedure is different, but the result remains the same whether we use the Caputo or the Riemann-Liouville formulation. In the rest of the thesis we restrict to use of the Caputo fractional derivative.

As is shown in Fig. 2.11, the relaxation modulus of the springpot element is dependent on the parameter α as well. For $\alpha \to 0$ the relaxation modulus becomes

$$R(t) = \frac{k}{\Gamma(1)}H(t),$$ (2.50)

thus the relaxation modulus of the elastic spring, Eq. (2.11). On the other hand, $\alpha \to 0$ gives

$$R(t) = \frac{k}{\Gamma(0)} \left(\frac{\tau_c}{t}\right) H(t). \tag{2.51}$$

The Gamma function is divergent at zero, $\Gamma(0^+) = \infty$ (see Appendix A) and we need to take into account a singularity at $t = 0$. For this limit case the relaxation modulus becomes the Dirac delta function, as was derived for the viscous dashpot.
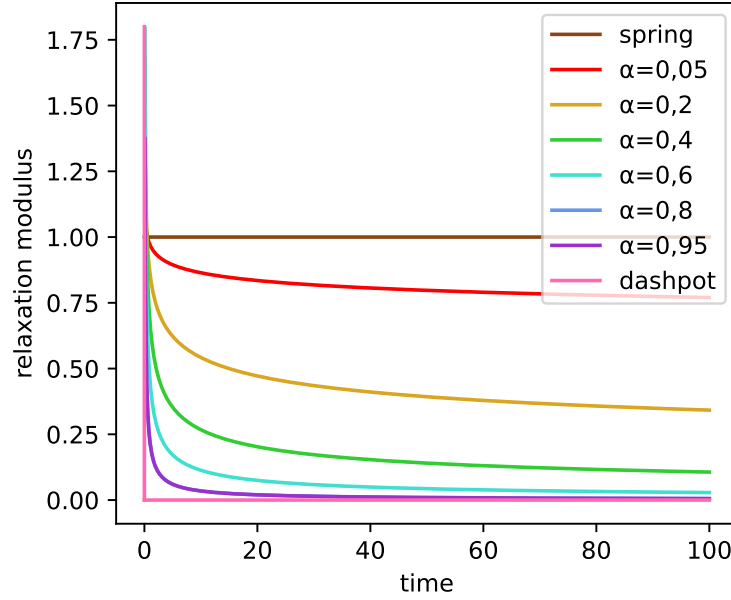

FIGURE 2.11: Relaxation modulus of springpot in dependence on parameter α

2.2.1.2 Complex stiffness of the springpot

The harmonic displacement load $u(t) = u_0^* e^{i\omega t}$ acting on the springpot leads to the following evolution of the internal force over time

$$F(\omega) = k\tau_c^\alpha D^\alpha u(\omega) = k\tau_c^\alpha D^\alpha u_0^* e^{i\omega t} = F_0^* e^{i\omega t}. \tag{2.52}$$

Adopting the Caputo fractional derivative introduced in Equation (A.17) gives

$$F(\omega) = \frac{k\tau_c^\alpha}{\Gamma(1-\alpha)} \int_{-\infty}^{t} (t-s)^{-\alpha} u_0^* \frac{\mathrm{d}}{\mathrm{d}t} e^{i\omega s} ds. \tag{2.53}$$

Note, that the lower limit of integral is set as $-\infty$ to prevent transient effects during oscillation. In this case the integration is not trivial and the following result was therefore taken from the literature, see [5], and verified in the WolframAlpha environment. The resulting expression has the following form

$$F(\omega) = k\tau_c^\alpha (i\omega)^\alpha u_0^* e^{i\omega t} = F_0^* e^{i\omega t}. \tag{2.54}$$

The complex stiffness of the springpot element can now be expressed as

$$k^*(\omega) = \frac{F_0^*}{u_0^*} = k(\mathrm{i}\omega\tau_\mathrm{c})^\alpha. \tag{2.55}$$

The imaginary unit can be rewritten in the trigonometric form as $\mathrm{i} = \cos\pi/2 + \mathrm{i}\sin\pi/2$. The use of the De-Moivre's formula $\mathrm{i}^n = \cos(n\pi/2) + \mathrm{i}\sin(n\pi/2)$, $n \in \mathbb{R}$ [27] provides

$$k^*(\omega) = \frac{F_0^*}{u_0^*} = k(\omega\tau_\mathrm{c})^\alpha\left(\cos\frac{\alpha\pi}{2} + \mathrm{i}\sin\frac{\alpha\pi}{2}\right). \tag{2.56}$$

Separation of the real and imaginary part then allows us to obtain the storage and loss stiffnesses of the springpot element in the following form

$$\begin{aligned} k'(\omega) &= k(\omega\tau_\mathrm{c})^\alpha\cos\frac{\alpha\pi}{2}, \\ k''(\omega) &= k(\omega\tau_\mathrm{c})^\alpha\sin\frac{\alpha\pi}{2}. \end{aligned} \tag{2.57}$$

The correctness of the solution can be once more verified by the substitution of the limit cases of α. For $\alpha = 0$ the loss stiffness becomes zero and the storage stiffness is $k'(\omega) = k$, corresponding to the behaviour of spring. For $\alpha = 1$ the storage stiffness becomes zero while the loss stiffness is $k''(\omega) = \nu\omega$, the behaviour of dashpot.

2.3 Arrangement of rheological elements

The individual elements, as were described in the previous sections, can be connected together to form more complex rheological models. The basic types of connections are connection in series and in parallel. Both types of connections have their characteristic behaviour which is introduced in the following text.
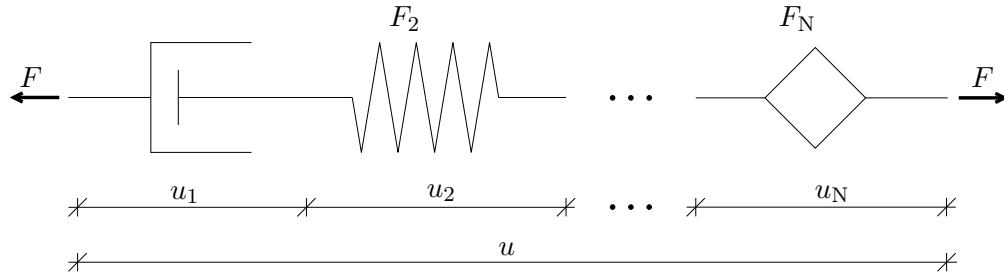
FIGURE 2.12: Serial connection of various rheological elements

The serial connection of various rheological elements is shown in Fig. 2.12. The condition of balance of forces must be met, therefore, for this type of connection the internal forces F_i for all individual elements are equal and also equal to the applied external force F. The same applies for the derivatives of the forces, including the fractional derivatives. Therefore,

$$F(t) = F_1(t) = F_2(t) = \cdots = F_N(t), \tag{2.58a}$$

$$\dot{F}(t) = \dot{F}_1(t) = \dot{F}_2(t) = \cdots = \dot{F}_N(t), \tag{2.58b}$$

$$D^\alpha F(t) = D^\alpha F_1(t) = D^\alpha F_2(t) = \cdots = D^\alpha F_N(t). \tag{2.58c}$$

Because each of the connected elements deforms individually, we obtain the total displacement u as the sum of the partial displacements u_i of individual elements

$$u(t) = u_1(t) + u_2(t) + \cdots + u_N(t), \tag{2.59a}$$

$$\dot{u}(t) = \dot{u}_1(t) + \dot{u}_2(t) + \cdots + \dot{u}_N(t), \tag{2.59b}$$

$$D^\alpha u(t) = D^\alpha u_1(t) + D^\alpha u_2(t) + \cdots + D^\alpha u_N(t). \tag{2.59c}$$

Combining Eqs. (2.58a), (2.59a) and (2.13) gives the creep modulus $J(t)$ as the sum of the creep moduli $J_i(t)$ of the individual elements connected in series

$$J(t) = J_1(t) + J_2(t) + \cdots + J_N(t) = \sum_{i=1}^{N} J_i(t). \tag{2.60}$$
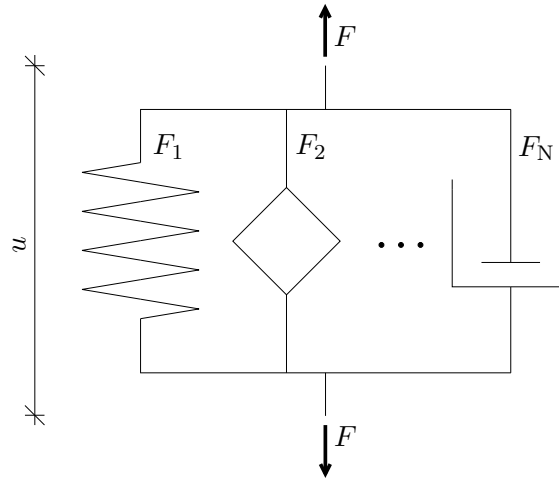

FIGURE 2.13: Parallel connection of various rheological elements

Compared to the serial connection, the elements connected in parallel, see Fig. 2.13, deform all as one and the displacement is the same for all of them. The continuity condition has the following form

$$u(t) = u_1(t) = u_2(t) = \cdots = u_N(t), \tag{2.61a}$$

$$\dot{u}(t) = \dot{u}_1(t) = \dot{u}_2(t) = \cdots = \dot{u}_N(t), \tag{2.61b}$$

$$D^\alpha u(t) = D^\alpha u_1(t) = D^\alpha u_2(t) = \cdots = D^\alpha u_N(t). \tag{2.61c}$$

Condition of the balance of forces tells us that the total force is equal to the sum of forces in individual parallel branches of the model. The equilibrium condition then read

$$F(t) = F_1(t) + F_2(t) + \cdots + F_N(t), \tag{2.62a}$$

$$\dot{F}(t) = \dot{F}_1(t) + \dot{F}_2(t) + \cdots + \dot{F}_N(t), \tag{2.62b}$$

$$D^\alpha F(t) = D^\alpha F_1(t) + D^\alpha F_2(t) + \cdots + D^\alpha F_N(t). \tag{2.62c}$$

The same holds for the relaxation modulus $R(t)$ as a consequence of Eqs. (2.61a), (2.62a) and (2.14). It can be obtained as the sum of the relaxation moduli $R_i(t)$ of the individual

elements connected in parallel

$$R(t) = R_1(t) + R_2(t) + \cdots + R_N(t) = \sum_{i=1}^{N} R_i(t). \tag{2.63}$$

Analogically we can obtain the complex stiffness

$$k^*(\omega) = k_1^*(\omega) + k_2^*(\omega) + \cdots + k_N^*(\omega) = \sum_{i=1}^{N} k_i^*(\omega), \tag{2.64}$$

the storage stiffness

$$k'(\omega) = k_1'(\omega) + k_2'(\omega) + \cdots + k_N'(\omega) = \sum_{i=1}^{N} k_i'(\omega) \tag{2.65}$$

and the loss stiffness

$$k''(\omega) = k_1''(\omega) + k_2''(\omega) + \cdots + k_N''(\omega) = \sum_{i=1}^{N} k_i''(\omega). \tag{2.66}$$

The most simple theoretical models used for the description of viscoelastic material consist of one elastic spring and one viscous dashpot. Their connection in series is called the Maxwell model while for their parallel connection we talk about the Kelvin-Voigt model [16]. These simple models are introduced in the following sections together with several more advanced viscoelastic models that are used for the material description later in this thesis.

2.3.1 Kelvin-Voigt model

The Kelvin-Voigt model is a parallel connection of a single spring with a single dashpot, the rheological scheme is shown in Fig. 2.14 (a).
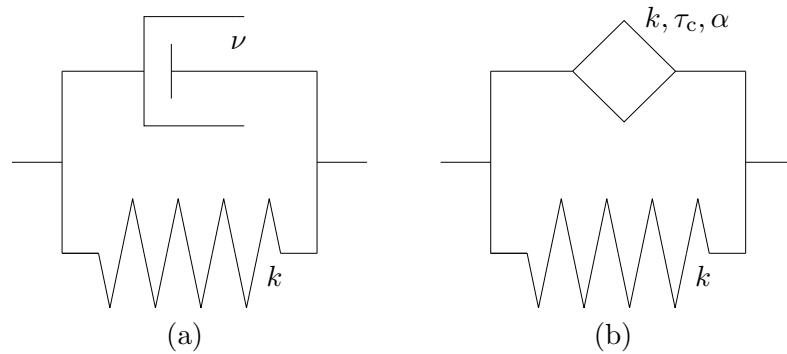

FIGURE 2.14: Rheological scheme of (a) standard, (b) fractional Kelvin-Voigt model

Instant force applied to the model does not cause instant displacement. This is the effect of a dashpot that is not able to deform instantaneously. Since there is no displacement there is no internal force in the spring and therefore at the beginning the whole force is

carried by the dashpot. This leads to increase of the displacement rate and the model starts to deform gradually. Increasing displacement leads to increase of force in the spring and decrease of force in the dashpot, also the decrease of displacement rate. As the time approaches infinity the displacement rate is zero. There is no internal force in the dashpot and the whole force is carried by the spring.

This behaviour is shown in Fig. 2.15 by the blue line. To write it mathematically we use Eq. (2.62a), the equilibrium condition for parallel connection, and the constitutive laws prescribed for spring and dashpot, Eq. (2.1) and Eq. (2.2), to get the following differential equation

$$F(t) = ku(t) + \nu\dot{u}(t). \tag{2.67}$$

For $F(t) = H(t)$ and the initial condition $u(0) = 0$ we obtain the creep modulus of the Kelvin-Voigt model as

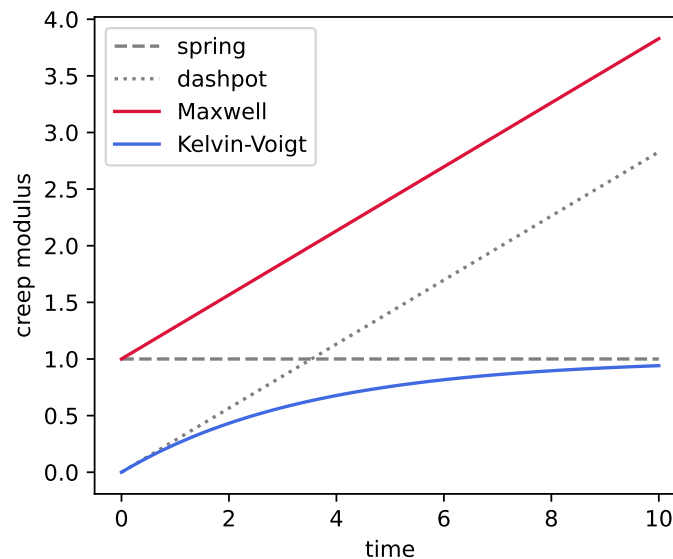$$J(t) = \frac{1}{k}\left(1 - \mathrm{e}^{-\frac{t}{\tau_c}}\right)H(t). \tag{2.68}$$

FIGURE 2.15: Creep modulus of the Maxwell and Kelvin-Voigt model

Loading of the Kelvin-Voigt model with an instant displacement causes infinite internal force of the dashpot at $t = 0$. The displacement remaining constant for $t > 0$ causes zero displacement rate and therefore $F_\mathrm{v} = 0$, the whole force is carried by the elastic element. We can prescribe the relaxation modulus mathematically as

$$R(t) = \begin{cases} \infty & \text{for} \quad t = 0 \\ k & \text{for} \quad t > 0. \end{cases} \tag{2.69}$$

Graphical representation is shown in Fig. 2.16 by the blue line. As well as for the single dashpot, this response is not realistic and therefore the Kelvin-Voigt model is not appropriate to describe relaxation.

In this research we further focus on the generalized Maxwell model in its standard as well as its fractional form. This is the reason why the Kelvin-Void model is only briefly introduced here while the Maxwell and fractional Maxwell models get closer attention in the following sections.
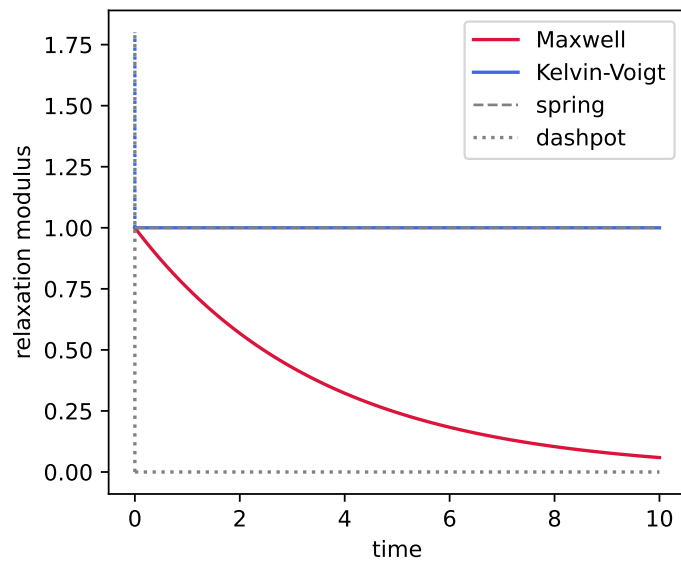
FIGURE 2.16: Relaxation modulus of the Maxwell and Kelvin-Voigt model

2.3.2 Maxwell model

The Maxwell model consists of a linear spring and a dashpot connected in series, its rheological scheme is shown in Fig. 2.17 (a).
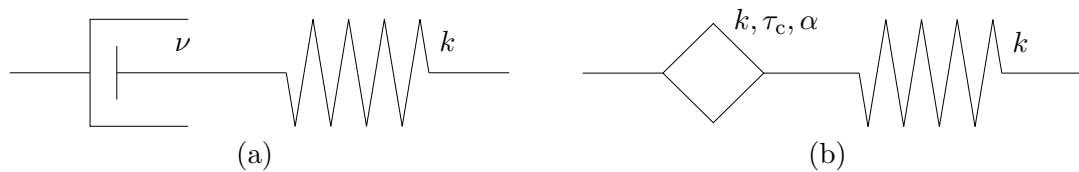

FIGURE 2.17: Rheological scheme of (a) standard, (b) fractional Maxwell model

An instant force applied to the Maxwell model causes an instant displacement of the spring. Since the force is the same in both, the spring and dashpot, the displacement increases gradually in time due to the constant displacement rate of the dashpot. This behaviour is shown in Fig. 2.15 by the red line. Now we substitute the Hooke and the Newton laws (Eq. (2.6) and Eq. (2.8)) into Eq. (2.59a), the continuity equation of serial connection. This substitution allows us to express the creep modulus of the Maxwell model in the following form

$$J(t) = \left(\frac{1}{k} + \frac{t}{\nu} \right) H(t) = \frac{1}{k} \left(1 + \frac{t}{\tau_{\mathrm{c}}} \right) H(t). \tag{2.70}$$

It is obvious that the creep modulus, plotted in Fig. 2.15 by a red line, is the sum of the creep moduli of the spring and the dashpot – Eq. (2.7) and Eq. (2.9).

When instant displacement is applied to the model, at $t = 0$ it is all carried by the spring. The displacement of spring causes non-zero internal force. The internal force then causes the displacement rate of the dashpot and the dashpot starts to deform. However, if the total displacement is held constant, the increasing displacement of the dashpot causes the decrease of displacement of the spring. This leads to decrease of the internal force. For $t \to \infty$ the whole displacement is carried by the dashpot while the

force becomes zero, so there is no long term stiffness. The red line in Fig. 2.16 represents this behaviour.

To express the relaxation modulus of the Maxwell model mathematically we substitute Eq. (2.1) and Eq. (2.2) into Eq. (2.59a). We get the following differential equation

$$\dot{u}(t) = \frac{\dot{F}(t)}{k} + \frac{F(t)}{\nu}, \tag{2.71}$$

which for $u(t) = H(t)$ and an initial condition $F(0) = F_e = kH(t)$ becomes

$$R(t) = k e^{-\frac{t}{\tau_c}} H(t). \tag{2.72}$$

Next, suppose that the model is loaded by the harmonic load $u(t) = u_0^* e^{i\omega t}$, the response is $F(t) = F_0^* e^{i\omega t}$. Upon substituting for $u(t)$ and $F(t)$ in Eq. (2.71) we get

$$u_0^* e^{i\omega t} = \frac{i\omega F_0^* e^{i\omega t}}{k} + \frac{F_0^* e^{i\omega t}}{\nu}. \tag{2.73}$$

The complex stiffness of the Maxwell model is now obtained as

$$k^*(\omega) = \frac{F_0^*}{u_0^*} = \frac{k i\omega\tau_c}{i\omega\tau_c + 1}. \tag{2.74}$$

Real and imaginary parts can be separated to get the storage and loss stiffnesses

$$\begin{aligned}
k'(\omega) &= \frac{k\omega^2\tau_c^2}{\omega^2\tau_c^2 + 1}, \\
k''(\omega) &= \frac{k\omega\tau_c}{\omega^2\tau_c^2 + 1}.
\end{aligned} \tag{2.75}$$

2.3.3 Fractional Maxwell model

Replacing the dashpot in the Maxwell model by the springpot element gives us the fractional Maxwell model, see the rheological scheme in Fig. 2.17 (b).

To describe the behaviour of the model we substitute the Hooke law, Eq. (2.1), and the constitutive law of the springpot, Eq. (2.9), into Eq. 2.59a, the continuity condition for serial connection. We get the following fractional differential equation

$$D^\alpha u(t) = \frac{D^\alpha F(t)}{k} + \frac{F(t)}{k\tau_c^\alpha}. \tag{2.76}$$

Introduction of the Heaviside force $F(t) = H(t)$ and subsequent integration lead to the creep modulus of the fractional Maxwell model

$$u(t) = \frac{H(t)}{k} + I^\alpha \frac{H(t)}{k\tau_c^\alpha} = J(t). \tag{2.77}$$

Expanding the Riemann-Liouville integral, Eq. (A.14), gives

$$J(t) = \frac{1}{k} \left[1 + \frac{1}{\Gamma(\alpha+1)} \left(\frac{t}{\tau_c} \right)^\alpha \right] H(t). \tag{2.78}$$

The creep modulus is the sum of the creep modulus of the spring, Eq. (2.7), and the springpot, Eq. (2.38).

To derive the relaxation modulus we start from Eq. (2.76). Performing the α-th integration of Eq. (2.76) and assuming the Heaviside displacement load $u(t) = H(t)$ yields

$$kH(t) = F(t) + I^{\alpha}\frac{F(t)}{\tau_{\mathrm{c}}^{\alpha}}. \tag{2.79}$$

The solution of this fractional differential equation can be obtained with use of the Laplace transform. Brief summary of this method is provided in Appendix B as well as the formulas for the Laplace transforms of functions used in the following transformation, Eq. (B.4) and Eq. (B.6). The Laplace transform allows us to convert a differential equation into an algebraic equation, which is simple to solve and the solution is then transformed back with the inverse Laplace transform.

To solve Eq. (2.79) for $F(t)$ we use the Laplace transform $\mathcal{L}\{F(t)\} \to \bar{F}(s)$ to get the transformed equation in the following form

$$\frac{k}{s} = \bar{F}(s) + \frac{\bar{F}(s)}{s^{\alpha}\tau_{\mathrm{c}}^{\alpha}}, \tag{2.80}$$

where $\bar{F}(s)$ is the Laplace transform of the unknown function. Modification of the equation allows us to find the solution in the Laplace domain as

$$\bar{F}(s) = k\frac{s^{\alpha-1}}{s^{\alpha} + \tau_{\mathrm{c}}^{-\alpha}}. \tag{2.81}$$

Now the inverse Laplace transform is performed using Eq. (B.5) to obtain the solution of the differential equation in the following form

$$F(t) = k\mathrm{E}_{\alpha,1}\left(-\left(\frac{t}{\tau_{\mathrm{c}}}\right)^{\alpha}\right), \tag{2.82}$$

where $\mathrm{E}_{\alpha,1}$ is the Mittag-Leffler function, see Appendix A. Finally, the relaxation modulus of the fractional Maxwell model is

$$R(t) = k\mathrm{E}_{\alpha,1}\left(-\left(\frac{t}{\tau_{\mathrm{c}}}\right)^{\alpha}\right)H(t). \tag{2.83}$$

Once again we consider the harmonic load $u(t) = u_0^*\mathrm{e}^{\mathrm{i}\omega t}$ with the response $F(t) = F_0^*\mathrm{e}^{\mathrm{i}\omega t}$. The substitution into Eq. (2.76) provides

$$D^{\alpha}u_0^*\mathrm{e}^{\mathrm{i}\omega t} = \frac{D^{\alpha}F_0^*\mathrm{e}^{\mathrm{i}\omega t}}{k} + \frac{F_0^*\mathrm{e}^{\mathrm{i}\omega t}}{k\tau_{\mathrm{c}}^{\alpha}}. \tag{2.84}$$

After integration we get the complex amplitude of the force

$$F_0^* = \frac{ku_0^*(\mathrm{i}\omega\tau_{\mathrm{c}})^{\alpha}}{(\mathrm{i}\omega\tau_{\mathrm{c}})^{\alpha} + 1}. \tag{2.85}$$

The complex stiffness can now be obtained as

$$k^*(\omega) = \frac{k(\mathrm{i}\omega\tau_\mathrm{c})^\alpha}{(\mathrm{i}\omega\tau_\mathrm{c})^\alpha + 1}. \tag{2.86}$$

The real and imaginary parts can be again separated using the De-Moivre's formula $\mathrm{i}^n = \cos(n\pi/2) + \mathrm{i}\sin(n\pi/2)$, $n \in \mathbb{R}$, which allows us to express the storage and loss stiffnesses as

$$
\begin{aligned}
k'(\omega) &= k\frac{(\tau_\mathrm{c}\omega)^{2\alpha} + (\tau_\mathrm{c}\omega)^\alpha \cos\left(\alpha\frac{\pi}{2}\right)}{(\tau_\mathrm{c}\omega)^{2\alpha} + 2(\tau_\mathrm{c}\omega)^\alpha \cos\left(\alpha\frac{\pi}{2}\right) + 1}, \\
k''(\omega) &= k\frac{(\tau_\mathrm{c}\omega)^\alpha \sin\left(\alpha\frac{\pi}{2}\right)}{(\tau_\mathrm{c}\omega)^{2\alpha} + 2(\tau_\mathrm{c}\omega)^\alpha \cos\left(\alpha\frac{\pi}{2}\right) + 1}.
\end{aligned}
\tag{2.87}
$$

2.3.4 Generalized Maxwell model

The possibilities in the connection of rheological elements lead to an endless amount of viscoelastic models. However, each of the models is appropriate to describe different types of materials. Simple viscoelastic models such as Maxwell, Kelvin-Voigt or single springpot model are not sufficient to describe polymers. Theoretical model mostly used for the description of these materials is the generalized Maxwell model in its standard as well as the fractional form, see Fig. 2.18. This was also examined in the previous research [15], where the response of various viscoelastic models was considered in comparison to the experimental results on PVB interlayer of laminated glass.
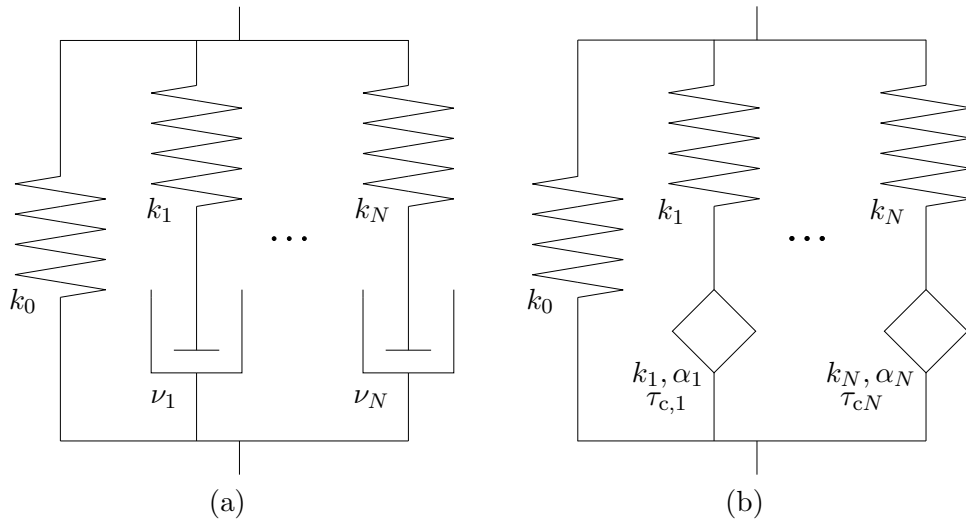

FIGURE 2.18: Rheological scheme of standard (a) and fractional (b) Maxwell chain

2.3.4.1 Standard Maxwell chain

The generalized Maxwell model, also known as the Maxwell chain, is a viscoelastic model consisting of a single spring and N Maxwell cells (the Maxwell cell is referred as a Maxwell model in the previous sections) arranged in parallel. Every cell is represented by its own parameters – single spring by its stiffness k_0 and i-th Maxwell cell by its stiffness k_i and coefficient of viscosity ν_i or characteristic time τ_{ci}. The standard Maxwell chain is shown in Fig. 2.18 (a).

Behaviour of single spring is given by the Hooke law (Eq. (2.1)) while the behaviour of each Maxwell cell is prescribed by the differential equation Eq. (2.71). The cells connected in parallel deform all as one, therefore $u = u_0 = u_1 = \cdots = u_N$. The force, on the other hand, is divided into individual branches of the model and the total force is then given as $F = F_0 + F_1 + \cdots + F_N$.

The relaxation modulus can be simply obtained as a sum of relaxation moduli of individual cells. Considering the relaxation modulus of single spring (Eq. (2.11)) and of the Maxwell model (Eq. (2.72)), the relaxation modulus of the Maxwell chain has the following form

$$R(t) = \left(k_0 + \sum_{i=1}^{N} k_i e^{-\frac{t}{\tau_{ci}}} \right) H(t). \tag{2.88}$$

The same way the complex, storage and loss stiffnesses can be obtained using Eq. (2.27) and Eqs. (2.74)-(2.75) as

$$k^*(\omega) = k_0 + \sum_{i=1}^{N} \frac{k_i i\omega\tau_{ci}}{i\omega\tau_{ci} + 1}, \tag{2.89}$$

$$k'(\omega) = k_0 + \sum_{i=1}^{N} \frac{k_i \omega^2 \tau_{ci}^2}{\omega^2 \tau_{ci}^2 + 1}, \tag{2.90}$$

$$k''(\omega) = \sum_{i=1}^{N} \frac{k_i \omega\tau_{ci}}{\omega^2 \tau_{ci}^2 + 1}. \tag{2.91}$$

It is obvious that the behaviour of the generalized model depends on the number of cells connected in the chain.
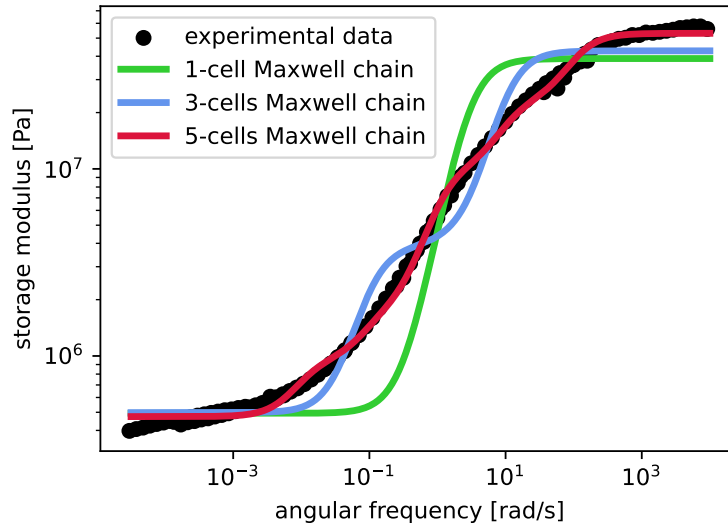

FIGURE 2.19: Approximation of experimentally obtained data by Maxwell chain with varying number of cells

In general, for higher number of cells we get better approximation of material behaviour. Figure 2.19 compares the approximation of experimentally obtained data of shear storage modulus (analogous quantity to storage stiffness) by the generalized Maxwell model of 1, 3 and 5 cells. It is clearly shown that for higher number of cells the model approximates

the data better. Theoretically, for $N \to \infty$ the model would describe the behaviour perfectly. However, increasing of the number of cells also leads to more free model parameters – k_i, τ_{ci}. These parameters need to be calibrated based on the material experiments.

Note that at this moment this figure is only illustrative to demonstrate the behaviour of the model. The experimentally obtained data as well as the experiment itself are introduced in detail in Chapter 4 together with the model calibration.

2.3.4.2 Fractional Maxwell chain

The fractional Maxwell chain is a parallel connection of a single spring and N fractional Maxwell cells. In this case each cell is represented by its stiffness k_i, characteristic time τ_{ci} and the springpot parameter α_i. This model is shown in Fig. 2.18 (b).

The relaxation modulus is the sum of the relaxation moduli of the spring Eq. (2.11) and of the fractional Maxwell model Eq. (2.83)

$$R(t) = \left(k_0 + \sum_{i=1}^{N} k_i \mathrm{E}_{\alpha,1} \left(- \left(\frac{t}{\tau_{ci}} \right)^{\alpha} \right) \right) H(t). \tag{2.92}$$

Considering Eq. (2.27) and Eqs. (2.86)-(2.87), the complex, storage and loss stiffness of the fractional Maxwell chain are then

$$k^*(\omega) = k_0 + \sum_{i=1}^{N} \frac{k_i (\mathrm{i}\omega\tau_{ci})^{\alpha_i}}{(\mathrm{i}\omega\tau_{ci})^{\alpha_i} + 1}, \tag{2.93}$$

$$k'(\omega) = k_0 + \sum_{i=1}^{N} k_i \frac{(\tau_{ci}\omega)^{2\alpha_i} + (\tau_{ci}\omega)^{\alpha_i} \cos\left(\alpha_i \frac{\pi}{2}\right)}{(\tau_{ci}\omega)^{2\alpha_i} + 2(\tau_{ci}\omega)^{\alpha_i} \cos\left(\alpha_i \frac{\pi}{2}\right) + 1}, \tag{2.94}$$

$$k''(\omega) = \sum_{i=1}^{N} k_i \frac{(\tau_{ci}\omega)^{\alpha_i} \sin\left(\alpha_i \frac{\pi}{2}\right)}{(\tau_{ci}\omega)^{2\alpha_i} + 2(\tau_{ci}\omega)^{\alpha_i} \cos\left(\alpha_i \frac{\pi}{2}\right) + 1}. \tag{2.95}$$

The same as for the standard Maxwell chain, the behaviour of the fractional model depends on the number of connected fractional Maxwell cells N. Higher number of cells requires to find more free parameters k_i, τ_{ci}, α_i based on the data obtained from material experiments (see more in Chapter 4). However, here we meet the main advantage of the fractional model – to fit the data well we need the lower number of cells in comparison to the standard Maxwell chain.

In Fig. 2.20 we can see the experimentally obtained data of shear storage modulus approximated by the fractional Maxwell chain for $N = 1$ and $N = 2$. It is clearly shown that even the 2-cells fractional model approximates the data well while the approximation quality is comparable to the 5-cells standard Maxwell chain (as was shown in Fig. 2.19 in the previous section). Therefore, even though we need to use more advanced mathematical apparatus, the use of the models based on fractional viscoelasticity could be advantageous for material description.
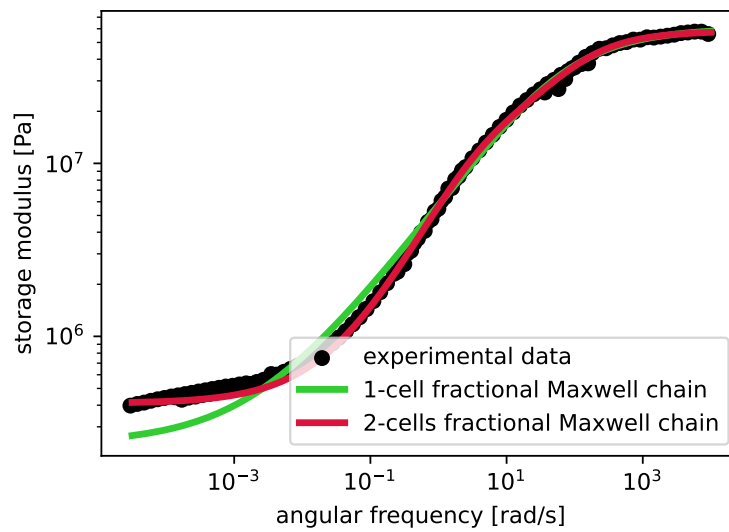
FIGURE 2.20: Approximation of experimentally obtained data by fractional Maxwell chain of various number of cells

This chapter provided an introduction to the theory of viscoelasticity with an analytically prescribed behaviour of several theoretical models. From now on, we are going to focus only on the generalized Maxwell model in its standard as well as its fractional form.

Chapter 3

Numerical description of the generalized Maxwell model

In our practical lives we come across a large number of problems that can be described mathematically by differential equations. In order to obtain an exact solution, these equations are often too difficult or even impossible to solve analytically, i.e. express the solution using elementary functions. Numerical methods allows us to solve these problems at the cost that the solution is only approximate.

Numerical methods in general are based on discretization of variables to the nodal points t^n, as is shown in the scheme in Fig. 3.3. The upper index denotes the coordinate of the nodal point, which for the constant step size Δt is given by $t^n = t^0 + n\Delta t$, t^0 is an initial node. The solution is then not found as a continuous function $f(t)$ but as a finite set of nodal values f^n in consecutive steps. In general, the more we reduce the step Δt the closer we get to the exact solution.
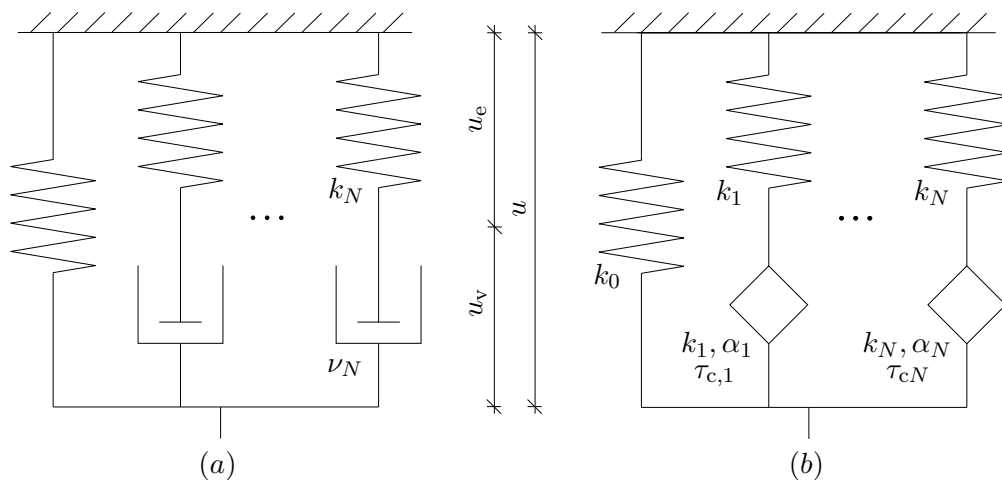

FIGURE 3.1: (a) Standard, (b) fractional form of the generalized Maxwell model

We have already met the differential equations earlier in this thesis. Several viscoelastic models were discussed in Chapter 2 and their behaviour in general was prescribed by the differential equations. For some special cases of loading (i.e. constant force or displacement, harmonic displacement) analytical solution of these equations was provided. However, for general load it is profitable to solve these equations numerically.

From now on we further narrow our focus to the generalized Maxwell model in its standard as well as fractional form. This chapter presents numerical algorithms to solve static and dynamic response of these two theoretical models in various loading situations. While the algorithms are derived for general models with N Maxwell cells, see Fig. 3.1, the presented examples consider the models for $N = 1$ – single spring connected with one Maxwell cell (standard or fractional), see Fig. 3.2. The reason is the transparency of results which allows us to clearly explain the influence of individual model parameters to the behaviour. Note that the three parametric model in Fig. 3.2 (a) is also termed the standard solid which help to resolve some of the drawbacks introduced in Section 3.2 for a single Maxwell cell.
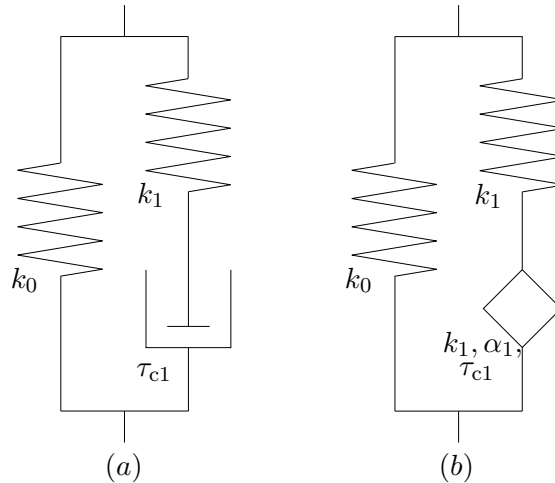

FIGURE 3.2: (a) Standard, (b) fractional generalized Maxwell model for $N = 1$

Numerical analysis presented in this chapter is based on the finite difference method (FDM), which is briefly introduced in the following section.
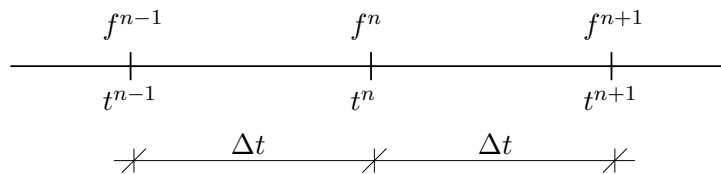

FIGURE 3.3: Nodal values for numerical solution

3.1 Finite difference method

This class of numerical methods obtains the approximate solution in steps. For the following node, the approximate value f^{n+1} is based on the previous nodal values $f(t^n)$, $f(t^{n-1})$, ... [6]. The numerical solution considers the differences instead of the derivatives – the derivatives in the differential equation are replaced with their numerical approximations [8].

3.1.1 Numerical approximations of derivatives

For the following numerical analysis we discretize the problem to finite set of nodal points. The value of derivative of a function in node t^n can be estimated based on the

values of this function in nearby nodal points. The coordinate of the node is given by $t^n = t^0 + n\Delta t$, where t^0 denotes the initial node and Δt is the step, [8]. For clarity the function in node t^n is denoted as $f^n \equiv f(t^n)$.

The most simple approximation of the first order derivative is given by the forward differencing scheme [8], [22]. This scheme is based on the definition of derivative and considers the derivative of the function as the tangent directive to the graph of the function. The approximation can be written in the following form

$$\dot{f}^n \approx \frac{f^{n+1} - f^n}{\Delta t}. \tag{3.1}$$

The finite difference method based on this differencing scheme is called the forward Euler method which is the most simple numerical method used to solve differential equations.

For the second-order derivative we use the approximation which is based on the central difference and can be written as [22]

$$\ddot{f}^n \approx \frac{f^{n+1} - 2f^n + f^{n-1}}{(\Delta t)^2}. \tag{3.2}$$

3.1.1.1 Numerical approximations of fractional derivative

To approximate the fractional derivative we use the forward differencing scheme introduced in [24] which approximates the fractional derivative $D^\alpha f$ as

$$D^\alpha f^n \approx \frac{1}{(\Delta t)^\alpha} \sum_{j=0}^{n} w_j(\alpha) f^{n+1-j}, \tag{3.3}$$

where j denotes the index of the step. For $j = 0$ it corresponds to the actual step and with increasing j we go retrospectively, $j = n$ then corresponds to the initial step at t^0. Therefore, the approximation of the fractional derivative depends on all of the nodal values obtained in previous steps. The influence of these values is given by the weights w_j that can be expressed in the following form [24]

$$\begin{aligned} w_0(\alpha) &= 1, \\ w_1(\alpha) &= -\alpha, \\ &\dots \\ w_j(\alpha) &= w_{j\text{-}1}(\alpha)\frac{j - 1 - \alpha}{j}. \end{aligned} \tag{3.4}$$

For the special case $\alpha = 1$ we get $w_0(\alpha) = 1$, $w_1(\alpha) = -1$. For $j \geq 2$ we get $w_j(\alpha) = 0$ and Eq. (3.3) becomes the forward differentiation scheme for the first derivative Eq. (3.1). For $\alpha = 0$ the only non-zero weight is for $j = 0$ and therefore the result at t^{n+1} is independent of the previous time steps.

3.1.2 Stability of the forward Euler method

The forward Euler method, as was introduced earlier, is classified as an explicit method. The advantage of explicit methods is that the value in node t^{n+1} can be expressed directly from the values in previous nodes. The implicit methods, on the other hand, give us the relationship between the values in the individual nodes and it requires additional computations to obtain these values [6] [7]. However, the disadvantage of explicit methods is their stability depending on the step size Δt.

The size of the step between the two nodes is a key parameter of the numerical solution. It strongly influences the behaviour including the accuracy of the approximation. The order of accuracy of the forward Euler method is one, in other words, the error of the numerical solution obtained with this method is proportional to the step Δt [6] [7]. Therefore, the solution for ten times smaller time step Δt requires the computation in ten times more steps to cover the time interval but the solution is obtained with ten times smaller error. The influence of the step size Δt on the approximation accuracy is provided on the specific example later in Section 3.3.1.1 while at this moment we are going to discuss its limits in the case of stability.
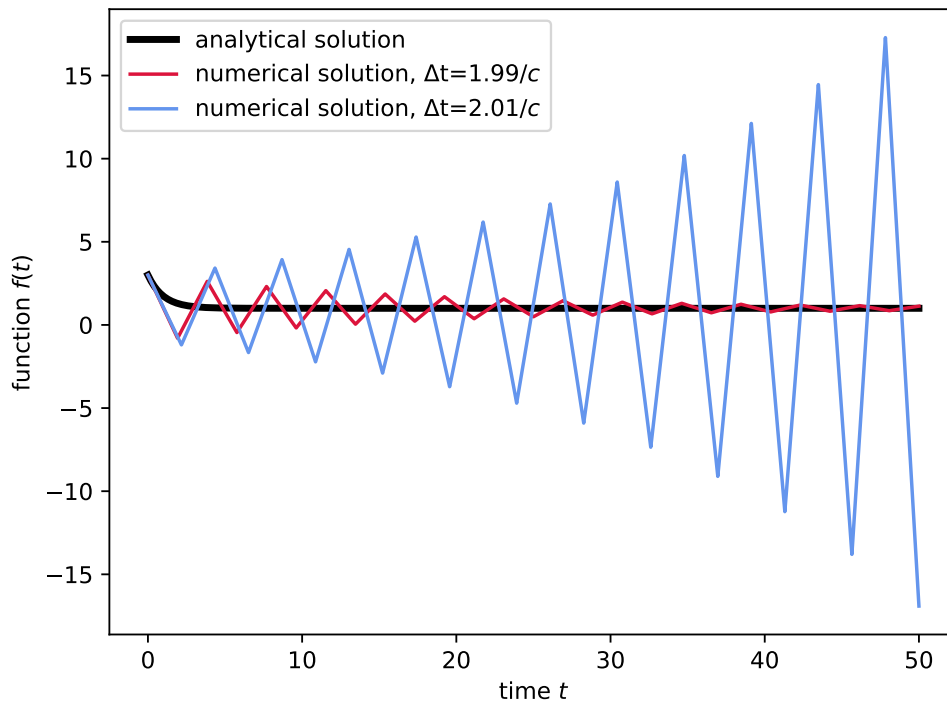

FIGURE 3.4: Instability of the forward Euler method

Let's consider the following differential equation

$$\dot{f}(t) + cf(t) = 0, \tag{3.5}$$

where c is a positive constant. Its discrete form in node t^n can be obtained by substituting the approximation of the first derivative Eq. (3.1) for $\dot{f}(t)$. We get

$$\frac{f^{n+1} - f^n}{\Delta t} + cf^n = 0 \tag{3.6}$$

from which we can explicitly express the value in the next node t^{n+1} as

$$f^{n+1} = f^n \left(1 - c\Delta t\right). \tag{3.7}$$

This expression can be further rewritten to

$$f^{n+1} = f^0 \left(1 - c\Delta t\right)^{n+1}. \tag{3.8}$$

Since n is non-negative integer, the behaviour of the approximate solution depends on the expression inside the bracket on the right hand side of Eq. (3.8). If the expression $1 - c\Delta t$ is positive the approximation of $f(t)$ is a decreasing function for $1/c > \Delta t$ which converges to the exact solution. For $c\Delta t < 0$ we would get a rising function and the approximate solution would be divergent, however, for $c > 0$, $\Delta t > 0$ this situation is impossible to occur.

If the expression $1 - c\Delta t$ is negative the approximate solution changes the sign each step, the solution is oscillating between the positive and negative values. For $1/c < \Delta t < 2/c$ the approximate solution converges to the exact solution, this is plotted in Fig. 3.4 by the red line. The blue line stands for $\Delta t > 2/c$. In this case the approximate solution oscillates between negative and positive values while the amplitudes grow beyond all limits. In this case we are not able to obtain the solution and we say for this step size the method is unstable.

3.2 Summary of necessary formulae

The generalized Maxwell model (or the Maxwell chain) consists of a spring with stiffness k_0 connected in parallel with N Maxwell cells, recall Fig. 3.1. The i-th cell is represented by its stiffness k_i, coefficient of viscosity ν_i (or characteristic time τ_{ci}) and the coefficient α_i – the standard Maxwell cell stands for the special case for $\alpha_i = 1$. For the sake of clarity, the following paragraphs summarise the formulae from Chapter 2 on which we base the following numerical analysis.

The characteristic time of i-th Maxwell cell was defined by Eq. (2.3) as

$$\tau_c = \frac{\nu}{k}. \tag{3.9}$$

The constitutive law describing the behaviour of the purely elastic element is given by the Hooke law (Eq. (2.1))

$$F_e(t) = k u_e(t) \tag{3.10}$$

and the behaviour of i-th standard Maxwell cell is described by the following differential equation (Eq. (2.71)) as

$$k_i \dot{u}(t) = \dot{F}_i(t) + \frac{F_i(t)}{\tau_{ci}}, \quad i = 1, 2, \ldots, N. \tag{3.11}$$

For i-th fractional Maxwell cell the behaviour is described by the fractional differential equation (Eq. (2.76))

$$k_i D^{\alpha_i} u(t) = D^{\alpha_i} F_i(t) + \frac{F_i(t)}{\tau_{ci}^{\alpha_i}}, \quad i = 1, 2, \ldots, N. \tag{3.12}$$

From Eq. (2.58a) we know that the force is the same in elements connected in series. Therefore, for i-th cell in the model it reads

$$F_i(t) = F_{ei}(t) = F_{vi}(t). \tag{3.13}$$

Total displacement of i-th cell is given as a sum of the partial displacements (Eq. (2.59a))

$$u_i(t) = u_{ei}(t) + u_{vi}(t). \tag{3.14}$$

This total displacement of i-th cell connected in parallel is the same as the displacement of the generalized model as a whole and also as the displacement of the single spring connected in the model (Eq. (2.61a))

$$u(t) = u_0(t) = u_i(t). \tag{3.15}$$

The total force is a sum of forces of each cell, including the spring, (Eq. (2.62a))

$$F(t) = F_0(t) + \sum_{i=1}^{N} F_i(t). \tag{3.16}$$

For the following analysis it is profitable for us to introduce the internal parameter $q_i(t)$ for i-th cell as

$$q_i(t) = k_i u(t) - F_i(t). \tag{3.17}$$

To explain its physical meaning we recall properties of serial connection – total displacement is a sum of elastic and viscous displacements (Eq. (3.14)) and internal force in the cell is equal to internal force of each serially connected element (Eq. (3.13)). Therefore, we can substitute the Hooke law (Eq. (3.10)) for $F_i(t)$ in Eq. (3.17) and rewrite it in the following form

$$q_i(t) = k_i u(t) - k_i u_{ei}(t) = k_i u_{vi}(t). \tag{3.18}$$

Now it is obvious that the internal parameter q_i describes the displacement of i-th viscous element multiplied by the stiffness k_i (which is constant). With the known physical meaning it is now simple to prescribe initial conditions $q_i(0) = q_i^0$.

The following sections introduce numerical algorithms to describe the behaviour of the standard and fractional Maxwell chain under various loading conditions. The numerical algorithms are derived for the general N-cells Maxwell model with parameters k_0, k_i, τ_{ci}, α_i. For the examples presented in this chapter we consider the specific parameters and initial conditions given by Tab. 3.1 unless otherwise stated. The numerical analysis is introduced on a static problem first, the extension to a dynamic problem is provided later in this chapter.

3.3 Static analysis

In the following text we describe the behaviour of the models in time domain. The model is loaded either by the prescribed force $F(t)$ to search for the displacement response $u(t)$ by the prescribed displacement $u(t)$ to determine the response $F(t)$. The time variable is discretized into nodal times t^n with the constant time step Δt, see Fig. 3.5.

Parameter	Notation	Value
Number of Maxwell cells	N	1
Stiffness of single spring	k_0	5 N/m
Stiffness of spring in the Maxwell cell	k_1	10 N/m
Characteristic time of the Maxwell cell	τ_{c1}	0.1 s
Springpot parameter (fractional model)	α_1	varying
Initial force	F^0	0
Initial displacement	u^0	0
Initial velocity	v^0	0
Initial condition for internal parameter	q_1^0	0

TABLE 3.1: Parameters of standard Maxwell chain considered for presented examples

The static load is usually applied over a long period of time. In real world, the typical example of the static load is the self weight of a structure. The changes of the static load over time are very small and it does not induce inertia forces [4]. Therefore, the equilibrium condition for the generalized Maxwell model is valid as was prescribed by Eq. (3.16). In the following sections we present the response of the standard and fractional Maxwell chains loaded either by a constant force or a constant displacement.
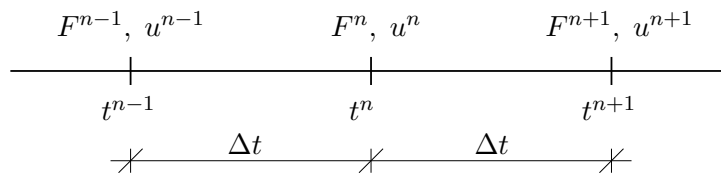

FIGURE 3.5: Nodal values for numerical solution

3.3.1 Standard Maxwell chain under static load

To describe the response of the standard Maxwell chain to static loading we need to solve the following system of equations. The behaviour of the single spring is described by the Hooke law (Eq. (3.10)), for i-th Maxwell cell by the differential equation (Eq. (3.11)) and these are bound by the equilibrum condition (Eq. (3.16)).

$$F_0(t) = k_0 u(t), \tag{3.19a}$$

$$k_i \dot{u}(t) = \dot{F}_i(t) + \frac{F_i(t)}{\tau_{ci}}, \tag{3.19b}$$

$$F(t) = F_0(t) + \sum_{i=1}^{N} F_i(t). \tag{3.19c}$$

The system consists of $N+2$ equations for $N+2$ unknowns – partial force in spring $F_0(t)$, partial force $F_i(t)$ in each of N Maxwell cells and either displacement $u(t)$ (for loading by the prescribed force) or total force $F(t)$ (for loading by the prescribed displacement).

Introduction of the internal parameter $q_i(t)$ prescribed by Eq. (3.17) allows us to rewrite the system of equations as

$$q_0(t) = 0, \tag{3.20a}$$

$$\dot{q}_i(t) + \frac{q_i(t)}{\tau_{ci}} = \frac{k_i u(t)}{\tau_{ci}}, \tag{3.20b}$$

$$F(t) + \sum_{i=1}^{N} q_i(t) = u(t)k_0 + u(t)\sum_{i=1}^{N} k_i. \tag{3.20c}$$

The system is now solved for unknown internal parameter of each cell $q_i(t)$ and still, either the displacement $u(t)$ or the total force $F(t)$. The partial forces $F_0(t)$ and $F_i(t)$ can be then evaluated as

$$F_0(t) = k_0 u(t),$$
$$F_i(t) = k_i u(t) - q_i(t). \tag{3.21}$$

The discretization of the problem is obtained by replacing the first derivative $\dot{q}_i(t)$ by the forward differentiation scheme introduced in Eq. (3.1). The discrete form of the system of equations in time node $t = t^n$ is

$$q_0^n = 0, \tag{3.22a}$$

$$\frac{q_i^{n+1} - q_i^n}{\Delta t} + \frac{q_i^n}{\tau_{ci}} = \frac{k_i u^n}{\tau_{ci}}, \tag{3.22b}$$

$$F^n + \sum_{i=1}^{N} q_i^n = u^n k_0 + u^n \sum_{i=1}^{N} k_i. \tag{3.22c}$$

From this discrete system the values in the consecutive time nodes are based on the initial condition prescribed at $t = t^0$. The initial condition specifies the clarity of the solution and it depends on the type of load. The following sections further discuss the numerical solution of the response to the applied force or the displacement load.

3.3.1.1   Constant displacement load

To illustrate the principle of FDM, let's consider the standard generalized Maxwell model loaded by the displacement $\hat{u}$ remaining constant from time $t = 0$. This load can be prescribed as the multiple of the Heaviside function $u(t) = \hat{u}H(t)$, however, for simplicity we constrict to times $t \geq 0$ and therefore we can write the expression as $u(t) = \hat{u}$. The instant displacement applied at t^0 is equal to the elastic displacement of each cell, because there is no instant deformation in the viscous element. Based on the zero initial conditions the force in i-th cell after the load is applied is then given by the Hooke law as $F_i^0 = k_i\hat{u}$ and as $F_0^0 = k_0\hat{u}$ for the force in single spring.

In this particular case the solution can be obtained from the original system of equations (3.19a) - (3.19c). For the constant displacement load $u(t) = \hat{u}$ the time derivative

$\dot{u}(t) = 0$ and therefore the system can be rewritten to the form

$$F_0(t) = k_0 u(t), \tag{3.23a}$$

$$\dot{F}_i(t) + \frac{F_i(t)}{\tau_{ci}} = 0, \tag{3.23b}$$

$$F(t) = F_0(t) + \sum_{i=1}^{N} F_i(t). \tag{3.23c}$$

The analytical solution of this problem was provided in the previous chapter, because the response to a constant load can be written as a multiple of the relaxation modulus by this constant, $F(t) = \hat{u}R(t)$, recall Eq. (2.14). The relaxation modulus of the standard Maxwell chain was derived in Section 2.3.4.1 in the form of Eq. (2.88)

$$R(t) = k_0 + \sum_{i=1}^{N} k_i e^{-\frac{t}{\tau_{ci}}}. \tag{3.24}$$

Therefore, the analytical solution to this problem can then be expressed in the following form

$$F(t) = \hat{u} \left(k_0 + \sum_{i=1}^{N} k_i e^{-\frac{t}{\tau_{ci}}} \right) \tag{3.25}$$

and it is plotted in Fig. 3.6 by the red line.

For loading by the constant displacement the solution of the system of equations, Eqs. (3.19a)-(3.19c), was simply obtained analytically. This fact gives us the opportunity to compare analytical solution and the solution obtained numerically with the use of FDM, specifically the forward Euler method.

To solve the response numerically we begin with the discretization of time variable to nodes, as was shown in Fig. 3.5. Introduction of the forward differencing scheme (Eq. (3.1)) leads to discretization of Eqs. (3.23a)-(3.23c) at $t = t^n$ as

$$F_0^n = k_0 u^n, \tag{3.26a}$$

$$\frac{F_i^{n+1} - F_i^n}{\Delta t} + \frac{F_i^n}{\tau_{ci}} = 0, \tag{3.26b}$$

$$F^n = F_0^n + \sum_{i=1}^{N} F_i^n. \tag{3.26c}$$

Since the displacement load $u(t) = \hat{u}$ is constant, its value is the same for each time step $u^0 = u^1 = \cdots = u^n = u^{n+1}$. From Eq. (3.26a) we see that the same applies to the partial force in the spring, therefore in time node $t = t^{n+1}$ it reads that

$$F_0^{n+1} = F_0^n. \tag{3.27}$$

The partial force in i-th Maxwell cell is simply expressed from Eq. (3.26b) as

$$F_i^{n+1} = F_i^n \left(1 - \frac{\Delta t}{\tau_{ci}} \right). \tag{3.28}$$

Finally, the total force at $t = t^{n+1}$ is provided by the equilibrium Eq. (3.26c)

$$F^{n+1} = F_0^{n+1} + \sum_{i=1}^{N} F_i^{n+1}. \tag{3.29}$$

The numerical solution is obtained in steps based on the initial condition prescribed at $t = 0$. In the first step $(n = 0)$ the known value $F_i^0 = F_i^n$ allows us to compute the value in the following step $F_i^1 = F_i^{n+1}$. The next step $(n = 1)$ is then based on the known value $F_i^1 = F_i^n$. This process is consecutively repeated in each step to find the approximate solution on the required interval.
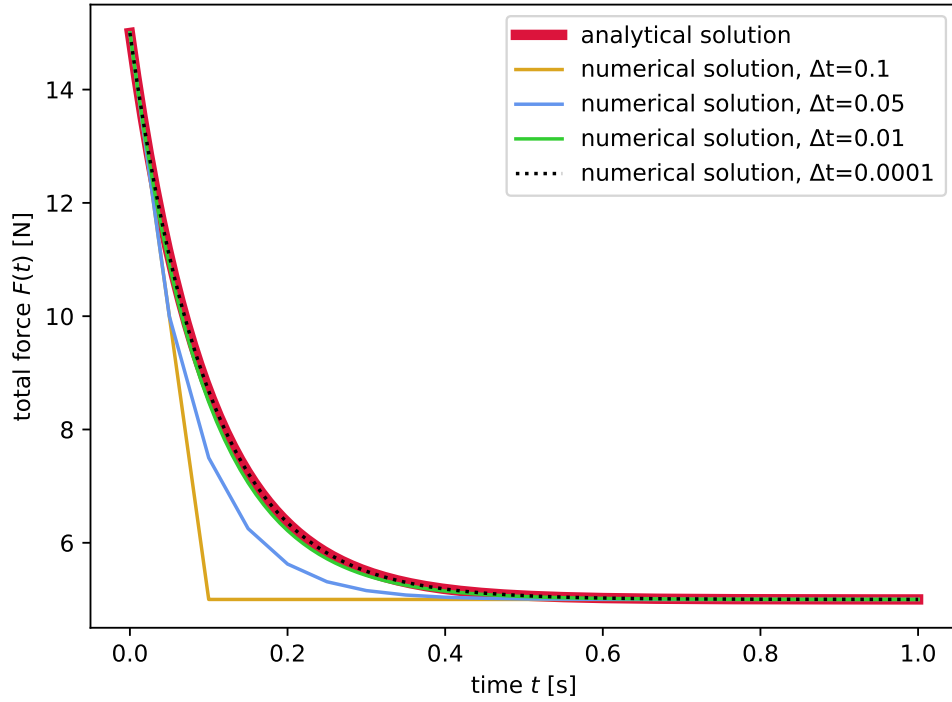
FIGURE 3.6: Maxwell chain $(N = 1)$ under constant strain load $\hat{u} = 1$ m analytical and numerical solution

For the standard Maxwell chain loaded by the constant displacement the numerical algorithm can be summarized as

$$F_0^{n+1} = F_0^n,$$

$$F_i^{n+1} = F_i^n \left(1 - \frac{\Delta t}{\tau_{ci}} \right),$$

$$F^{n+1} = F_0^{n+1} + \sum_{i=1}^{N} F_i^{n+1}. \tag{3.30}$$

Figure 3.6 compares the analytical solution of Eqs. (3.23a)-(3.23c) (the red line) with the numerical solutions obtained by the forward Euler method for variable time step Δt. The model parameters presented in Tab. 3.1 are considered, the model is loaded by the constant displacement $\hat{u} = 1$ m.

It is obvious that for smaller steps we are closer to the exact solution, as was already mentioned in Section 3.1.2. The graphs presented in the rest of this chapter use the numerical solution for the time step $\Delta t = 0.001$ s. This value leads to the behaviour described accurately and smoothly enough to discuss the results and see the main trends in the response while it still maintains a reasonable computational effort.

In Fig. 3.7 we see the numerically described response of one-cell standard Maxwell chain ($N = 1$, recall Fig. 3.2) with varying parameter τ_{c1} to the constant displacement load prescribed as $\hat{u} = 1$ m, parameters of the model and the initial condition are considered according to Tab. 3.1. The limit cases of the model for τ_{c1} are schematically shown in Fig. 3.8. For $\tau_{c1} \to \infty$ the viscosity of the dashpot is infinite and there is no viscous displacement, $u_{v1}(t) = 0$. Therefore, from Eq. (3.14) we know that $u(t) = u_{e1}(t)$. In this limit case the model behaves as two springs connected in parallel, the response is purely elastic with stiffness $k_0 + k_1$. The response is shown as the black line in the plot in Fig. 3.7.
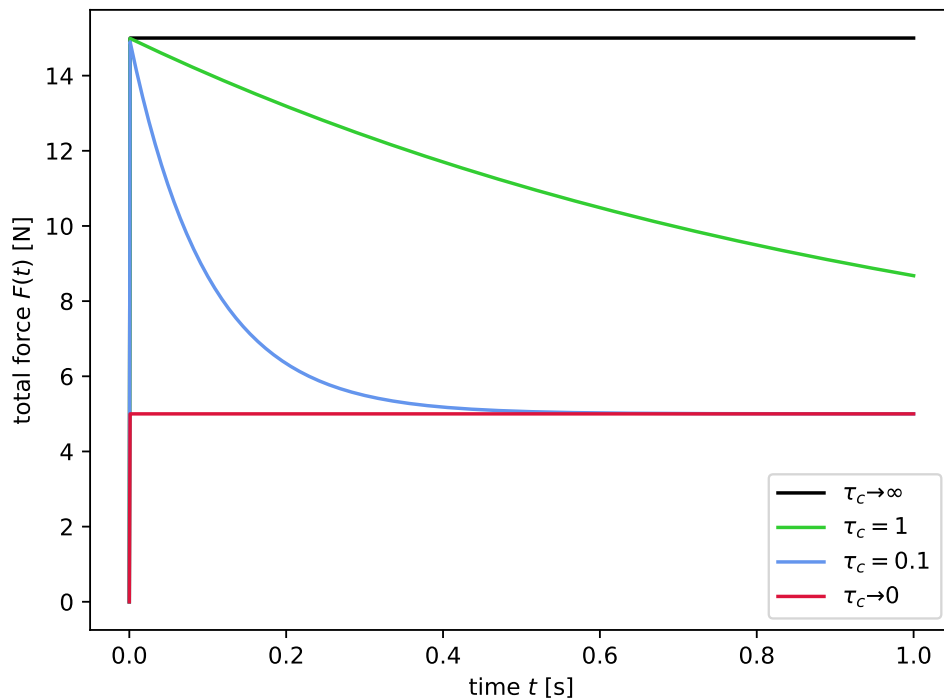

FIGURE 3.7: Static force response of standard Maxwell chain ($N = 1$) to loading by constant displacement $\hat{u} = 1$ m

The second limit case stands for $\tau_{c1} \to 0$. In this case there is no viscosity of the dashpot which leads to its unlimited mobility. The whole load is then carried by the single spring. For this limit case the response is purely elastic as well. The difference is that this time the resistant stiffness is only k_0 and therefore the response is more compliant, the same displacement load results in lower internal force. In this case the response is shown as the red line in the graph.

3.3.1.2 Constant force load

In the previous example we compared the analytical and numerical solution of the response of the standard Maxwell chain loaded by a constant displacement. The response

to displacement load is simple to solve – each cell (including the single spring) is loaded by the same displacement and therefore we can solve the response $F_i(t)$ of each cell separately from the differential equation describing i-th Maxwell cell (Eq. (3.11)) and the constitutive law for the single spring (Eq. (3.10)). The total response $F(t)$ is then given by a simple sum of partial responses (Eq. (3.16)).
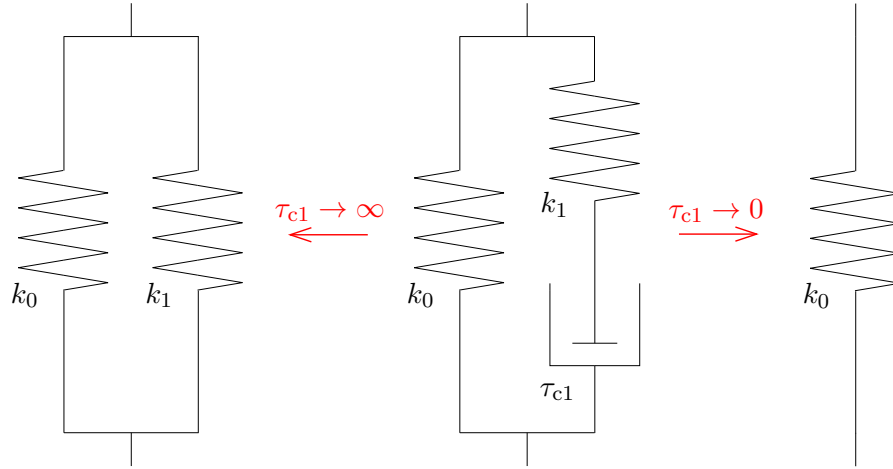

FIGURE 3.8: Limit cases of characteristic time τ_{c1} for 1-cell standard Maxwell chain

For the force load we have to consider interdependence between the displacement response $u(t)$, force in the single spring $F_0(t)$ and N forces in the connected Maxwell cells $F_i(t)$. This problem leads to a system of $N + 2$ equations including the constitutive law for the single spring Eq. (3.10), the differential equation for each of N Maxwell cells Eq. (3.11) and the equilibrium condition Eq. (3.16). This system of equations was presented with the use of internal parameter $q_i(t)$, Eqs. (3.20a)-(3.20c), and in the discrete form, Eqs. (3.22a)-(3.22c).

This system of equations can be now solved in consecutive steps based on the values of q_i^0 and u^0 prescribed by the initial conditions at t^0. From Eq. (3.22b) written at t^n the internal parameters q_i^{n+1} can be expressed as

$$q_i^{n+1} = \frac{\Delta t}{\tau_{ci}} k_i u^n + q_i^n - \frac{\Delta t}{\tau_{ci}} q_i^n, \tag{3.31}$$

and from Eq. (3.22c) written at t^{n+1} the displacement u^{n+1} can be evaluated in the following form

$$u^{n+1} = \frac{1}{k_0 + \sum\limits_{i=1}^{N} k_i} \left(F^{n+1} + \sum\limits_{i=1}^{N} q_i^{n+1} \right). \tag{3.32}$$

The internal force F_i^{n+1} in i-th cell can be simply expressed from the definition of the internal parameter given by Eq. (3.17).

For now we consider the load by instantaneous force applied at $t = 0$ and remaining constant since this moment. For times $t \geq 0$ the load is prescribed as $F(t) = \hat{F}$. Assuming an undeformed state before the load is applied the initial condition can be formulated as $u^0 = 0$. The instantaneous force leads to the instantaneous elastic deformation which is the same for each cell including the single spring. This elastic displacement can be

simply obtained from the Hooke law as $u^0 = \hat{F}/(k_0 + k_1 + \cdots + k_N)$. The force $\hat{F}$ is divided into individual cells in proportion to their stiffnesses, therefore $F_0^0 = k_0 u^0$, $F_i^0 = k_i u^0$. There is no instantaneous deformation in any of the viscous elements and therefore the initial condition for the internal parameter can be prescribed as $q_i^0 = 0$.
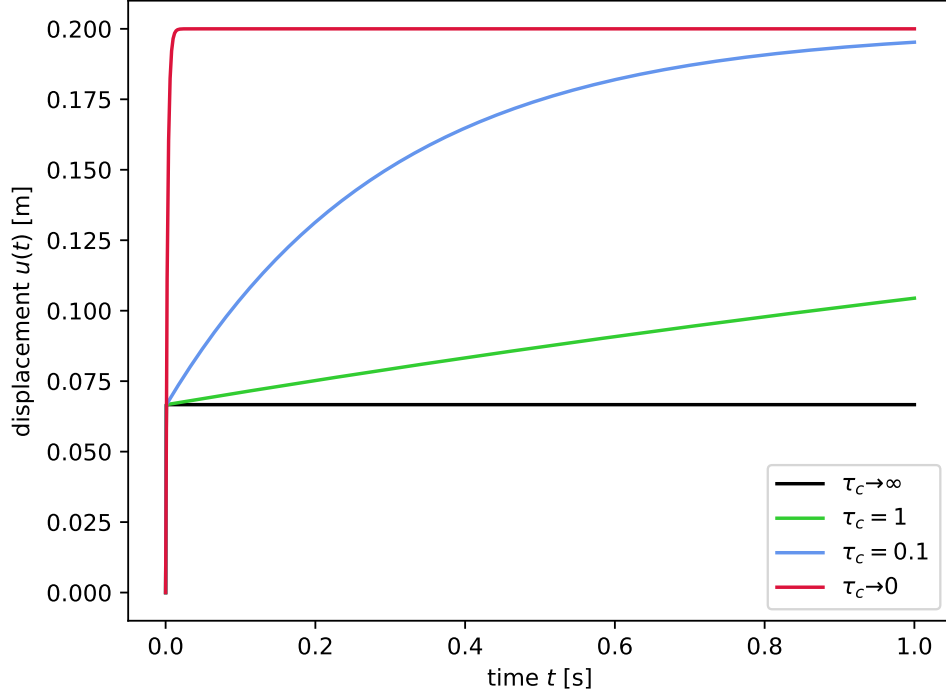

FIGURE 3.9: Static displacement response of standard Maxwell chain ($N = 1$) subjected to constant force load $\hat{F} = 1$ N

Figure 3.9 shows the behaviour of 1-cell standard Maxwell chain loaded by constant force $\hat{F} = 1$ N and the model parameters given by Tab. 3.1. The graph compares the behaviour of this model for varying value of the characteristic time τ_{c1} of the connected Maxwell cell. The two limit cases for τ_{c1} were already discussed in detail above in Section 3.3.1.1, the scheme of the model in these limit cases was shown in Fig. 3.8. The black line in Fig. 3.9 stands for the limit case $\tau_{c1} \to \infty$ which corresponds to the response of the elastic model having the stiffness $k_0 + k_1$. The red line then describes the limit case for $\tau_{c1} \to 0$, the response corresponding to the elastic model with the stiffness k_0. The blue and green lines stand for the intermediate values of τ_{c1}.

For $t = 0$ the instant force load causes instant displacement of the elastic elements, the initial stiffness is given as $k_0 + k_1$. For $t > 0$ we observe a significant increase of displacement, i.e. the creep effect. For $t \to \infty$ the displacement reaches its limit value given by the long-term stiffness k_0.

This effect is displayed in Fig. 3.10 which shows evolution of the displacement in individual elements of the model for $\tau_{c1} = 10$ s under constant loading force $\hat{F} = 1$ N. The displacement of the whole model $u(t)$ (plotted by the green line) is the same as the displacement of the single spring $u_0(t)$. The displacement of the Maxwell cell is divided to elastic and viscous part. For $t = 0$ the whole displacement of the Maxwell cell is elastic with the resisting stiffness k_1. For $t > 0$ the viscous displacement increases causing the elastic displacement as well as the internal force in the Maxwell cell F_1 to decrease. The evolution of the internal forces in single spring F_0 and Maxwell cell F_1 under the same loading conditions is shown in Fig. 3.11. Since $F = F_0 + F_1$ the force in

the single spring F_0 is increasing together with decreasing force in the Maxwell cell F_1. At time $t \to \infty$ the whole deformation of the Maxwell cell is carried by the dashpot and therefore this cell does not carry any force, $F_1 \to 0$. The whole force is finally carried by the single spring with the long-term stiffness k_0.

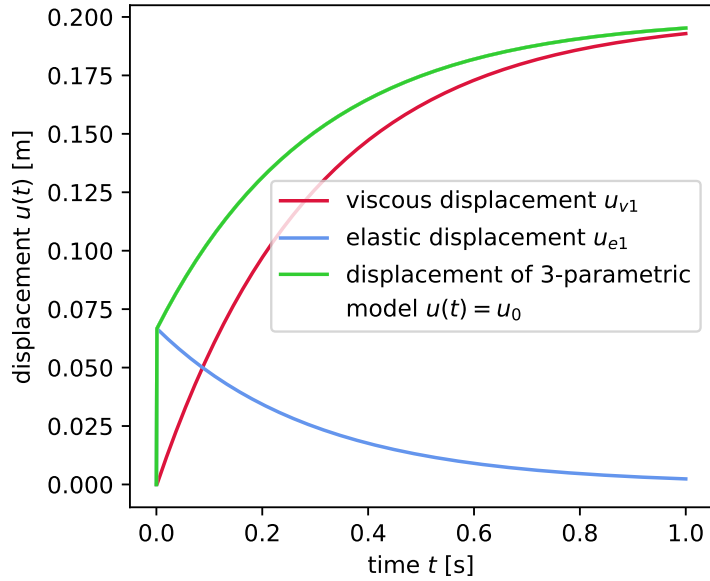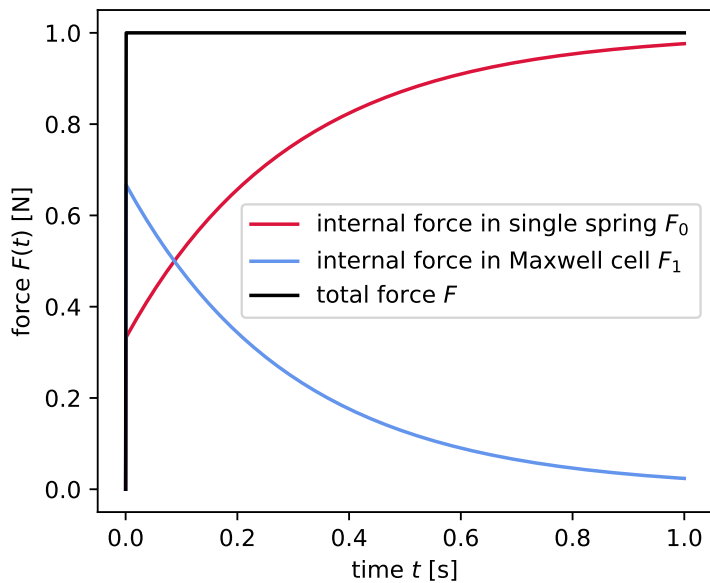FIGURE 3.10: Evolution of displacement $u(t) = u_0$, u_{e1}, u_{v1} of standard Maxwell chain ($N = 1$) under constant force load $\hat{F} = 1$ N

FIGURE 3.11: Evolution of partial forces F_0, F_1 of standard Maxwell chain ($N = 1$) under constant force load $\hat{F} = 1$ N

3.3.2 Fractional Maxwell chain under static load

Behaviour of the fractional Maxwell chain consisting of a single spring and N Maxwell cells can be described by the system of equations including the Hooke law (Eq. (3.10)), the fractional differential equation for i-th fractional Maxwell cell (Eq. (3.12)) and the equilibrium condition (Eq. (3.16)). The system of equations has the following form

$$F_0(t) = k_0 u(t), \tag{3.33a}$$

$$k_i D^{\alpha_i} u(t) = D^{\alpha_i} F_i(t) + \frac{F_i(t)}{\tau_{\mathrm{c}i}^{\alpha_i}}, \tag{3.33b}$$

$$F(t) = F_0(t) + \sum_{i=1}^{N} F_i(t). \tag{3.33c}$$

The system can be rewritten by introduction of the internal parameter $q_i(t)$ (Eq. (3.17)) as

$$q_0(t) = 0, \tag{3.34a}$$

$$D^{\alpha_i} q_i(t) + \frac{q_i(t)}{\tau_{\mathrm{c}i}^{\alpha_i}} = \frac{k_i u(t)}{\tau_{\mathrm{c}i}^{\alpha_i}}, \tag{3.34b}$$

$$F(t) + \sum_{i=1}^{N} q_i(t) = u(t)k_0 + u(t)\sum_{i=1}^{N} k_i. \tag{3.34c}$$

The fractional derivative $D^{\alpha_i} q_i(t)$ can be now approximated by the forward differentiation scheme Eq. (3.3). The approximation at time $t = t^n$ then reads

$$q_0^n = 0, \tag{3.35a}$$

$$\frac{1}{(\Delta t)^{\alpha_i}} \sum_{j=0}^{n} w_j(\alpha_i) q^{n+1-j} + \frac{q_i^n}{\tau_{\mathrm{c}i}^{\alpha_i}} = \frac{k_i u^n}{\tau_{\mathrm{c}i}^{\alpha_i}}, \tag{3.35b}$$

$$F^n + \sum_{i=1}^{N} q_i^n = u^n k_0 + u^n \sum_{i=1}^{N} k_i. \tag{3.35c}$$

which can be further adjusted to

$$q_0^n = 0, \tag{3.36a}$$

$$q^{n+1} + \sum_{j=1}^{n} w_j(\alpha_i) q^{n+1-j} + q_i^n \frac{(\Delta t)^{\alpha_i}}{\tau_{\mathrm{c}i}^{\alpha_i}} = k_i u^n \frac{(\Delta t)^{\alpha_i}}{\tau_{\mathrm{c}i}^{\alpha_i}}, \tag{3.36b}$$

$$F^n + \sum_{i=1}^{N} q_i^n = u^n k_0 + u^n \sum_{i=1}^{N} k_i. \tag{3.36c}$$

Recall that the approximation of the fractional derivative depends on the values of all previous time nodes. The influence of j-th value is given by the value of the weight function $w_j(\alpha_i)$ specified by Eq. (3.4). The weights in absolute value are shown in Fig. 3.12 depending on j, the retrospective coordinate of time node – $j = 0$ is the actual time and increasing j corresponds to the previous time steps.
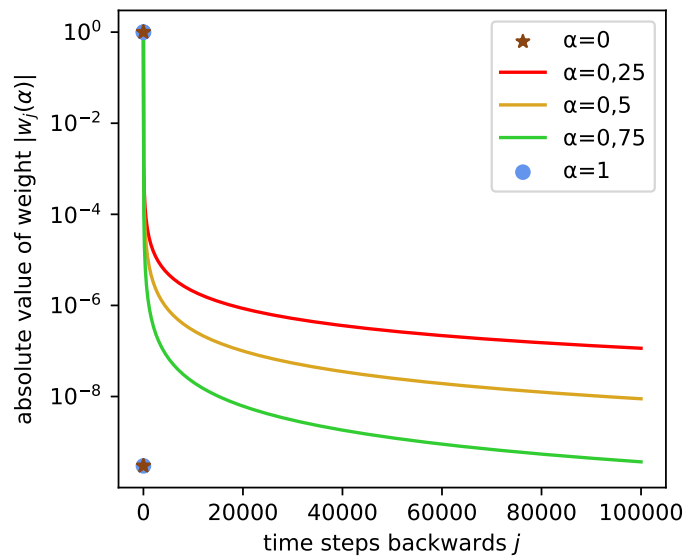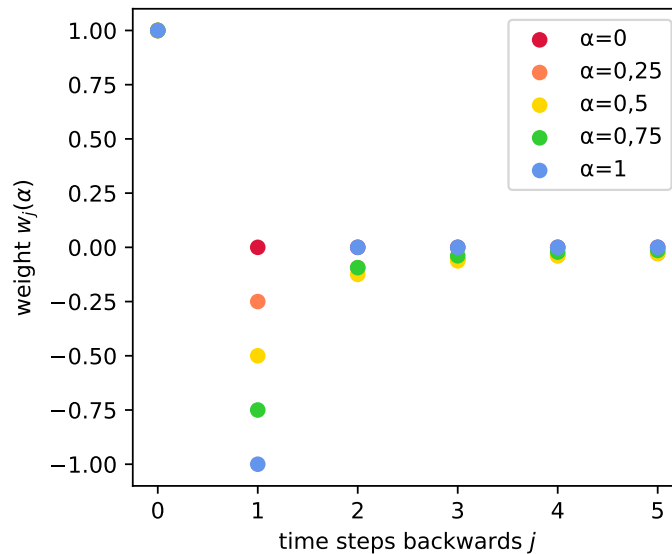
FIGURE 3.12: Weight function for different values of α

FIGURE 3.13: Weight function for different values of α

Figure 3.13 then shows the detail of weights for the most recent time steps. Recall, that the actual step coordinate is $j = 0$ where the weight $w_0 = 1$ for any α_i. The graph clearly shows that for $\alpha = 0$ (springpot becomes purely elastic) the only non-zero value is for $j = 0$ and therefore there is no influence of previous time steps, the elastic response is load-history independent. For $\alpha = 1$ (springpot becomes purely viscous) the non-zero values are for $j = 0$ and $j = 1$. The evaluation of the response for the next time step considers the last two nodal values. For the intermediate values of α the values in all of the previous steps are considered. However, from the graph it is obvious that the weights are decreasing the further back in time we go. Simply put, the influence of the most recent values ($j = 0$, $j = 1$, ...) is greater than for the older ones. Also we can see that the closer the parameter α is to 1, the faster the weight function decreases.

3.3.2.1 Constant displacement load

Loading of the model by the prescribed displacement $u(t)$ retrieves the unknown total internal force $F(t)$ depending on the internal force in each cell $F_i(t)$ and in the single spring $F_0(t)$. For the solution it is profitable to describe the model using the internal parameter $q_i(t)$. Therefore, at the moment we need to solve the system of Eqs. (3.34a)-(3.34c) for unknowns $q_i(t)$ and $F(t)$. The internal parameter $q_i(t)$ of i-th cell allows us to simply evaluate the internal force $F_i(t)$ of this cell as

$$F_i(t) = k_i u(t) - q_i(t). \tag{3.37}$$

The unknown internal parameter q_i^{n+1} can be expressed from Eq. (3.36b) written at $t = t^n$ as

$$q_i^{n+1} = \left(\frac{\Delta t}{\tau_{ci}}\right)^{\alpha_i} k_i u^n - \left(\frac{\Delta t}{\tau_{ci}}\right)^{\alpha_i} q_i^n - \sum_{j=1}^{n} w_j(\alpha_i) q^{n+1-j}. \tag{3.38}$$

Equation (3.36c) written at $t = t^{n+1}$ then provides the force F^{n+1} in the form

$$F^{n+1} = u^{n+1} \left(k_0 + \sum_{i=1}^{N} k_i \right) - \sum_{i=1}^{N} q_i^{n+1}. \tag{3.39}$$

With the use of this algorithm we can solve the response of the fractional Maxwell chain to the prescribed static displacement load $u(t)$.

Considering the constant displacement load prescribed as $u(t) = \hat{u}$ for $t \geq 0$ gives $u^0 = u^1 = \cdots = u^n$. Introducing this load in Eqs. (3.37) – (3.39) yields the response shown in Fig. 3.14.

In the previous section we focused on the standard Maxwell chain and discussed its response in dependence on the characteristic time τ_{c1} of the connected Maxwell cell. The influence of the characteristic time for the fractional Maxwell chain leads to similar results as for the standard Maxwell chain. For $\tau_{c1} \to 0$ the springpot in the Maxwell cell carries no force and the model acts as purely elastic with stiffness k_0, $\tau_{c1} \to \infty$ stands for the limit case where there is no movement in the viscous element and therefore the model acts as purely elastic with stiffness $k_0 + k_1$, the intermediate values of τ_{c1} then suggests the response of the model with significant relaxation.

The graph showing the results for varying parameter τ_{c1} would be almost the same as the one for the standard Maxwell chain shown in Fig. 3.7 and therefore, for the sake of brevity it is not presented here, only the two limit cases are plotted in Fig. 3.14. For the fractional chain it is interesting to discuss the response in dependence on the springpot parameter α_1. Figure 3.14 shows the results for the model parameters according to Tab. 3.1 and for the varying parameter α_1. The constant displacement load is prescribed as $\hat{u} = 1$ m.

From Chapter 2 we already know the limit cases for the parameter α_1. The scheme of the model in limit cases is shown in Fig. 3.15. For the limit case $\alpha_1 = 1$ the springpot becomes purely viscous and the model behaves the same way as the standard Maxwell chain, this is plotted by the blue line in the graph in Fig. 3.14 and this response is the same as for the standard Maxwell chain (the blue line in Fig. 3.7).
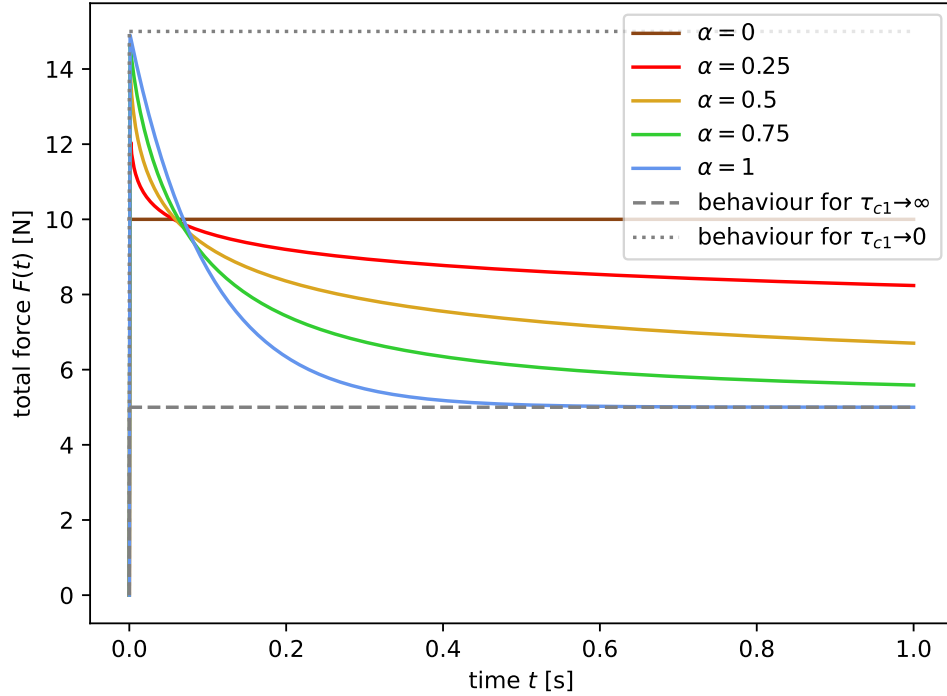
FIGURE 3.14: Static force response of fractional Maxwell chain ($N = 1$) to constant displacement load $\hat{u} = 1$ m
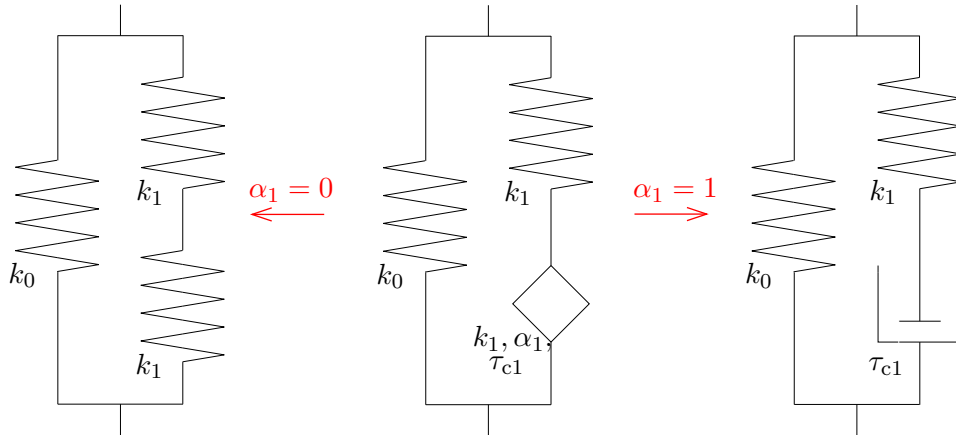

FIGURE 3.15: Limit cases of springpot parameter α_1 for fractional Maxwell chain

For $\alpha_1 = 0$ the springpot behaviour becomes purely elastic, see the brown line in Fig. 3.14. In this limit case the model behaves as purely elastic with stiffness $k_0 + k_1/2$. The springpot element becomes spring in this limit case and therefore decreases the stiffness of the cell as we get two serially connected springs, this leads to greater compliance of the model. For comparison, the grey dashed line in the graph stands for the case of different characteristic time, $\tau_{c1} \to \infty$, where there is no movement in the springpot element.

It is appropriate to point out that for each different value of parameter α_1 the response in limit tends to the same constant value given by the limit case $\tau_{c1} \to \infty$. However, the rate of convergence is different for different values of α_1. The closer the parameter α_1 is to zero the closer is the behaviour of the springpot to elastic and therefore the slower

(less significant) is the relaxation process. On the other hand, for $\alpha_1 \to 1$ the springpot behaves more as viscous element and the relaxation is more significant.

3.3.2.2 Constant force load

Loading by the constant static force requires solving the system of Eqs. (3.34a)-(3.34c) for $q_i(t)$ and $u(t)$. For the discrete problem the internal parameter q_i^{n+1} can follows from Eq. (3.36b) written at time $t = t^n$ as

$$q_i^{n+1} = \left(\frac{\Delta t}{\tau_{ci}}\right)^{\alpha_i} k_i u^n - \left(\frac{\Delta t}{\tau_{ci}}\right)^{\alpha_i} q_i^n - \sum_{j=1}^{n} w_j(\alpha_i) q^{n+1-j}. \tag{3.40}$$

The unknown displacement in the next node u^{n+1} is then found from Eq. (3.36c) for $t = t^{n+1}$ as

$$u^{n+1} = \frac{1}{k_0 + \sum\limits_{i=1}^{N} k_i} \left(F^{n+1} + \sum_{i=1}^{N} q_i^{n+1}\right). \tag{3.41}$$

From this algorithm we simply obtain the response in successive time steps based on the prescribed force and initial conditions q_i^0 and u^0. Since there is no deformation of the viscous element, the initial condition for the internal parameter is given by $q_i^0 = 0$. For the displacement the initial condition is derived from the purely elastic model as $u^0 = F^0/(k_0 + k_1 + \cdots + k_N)$.
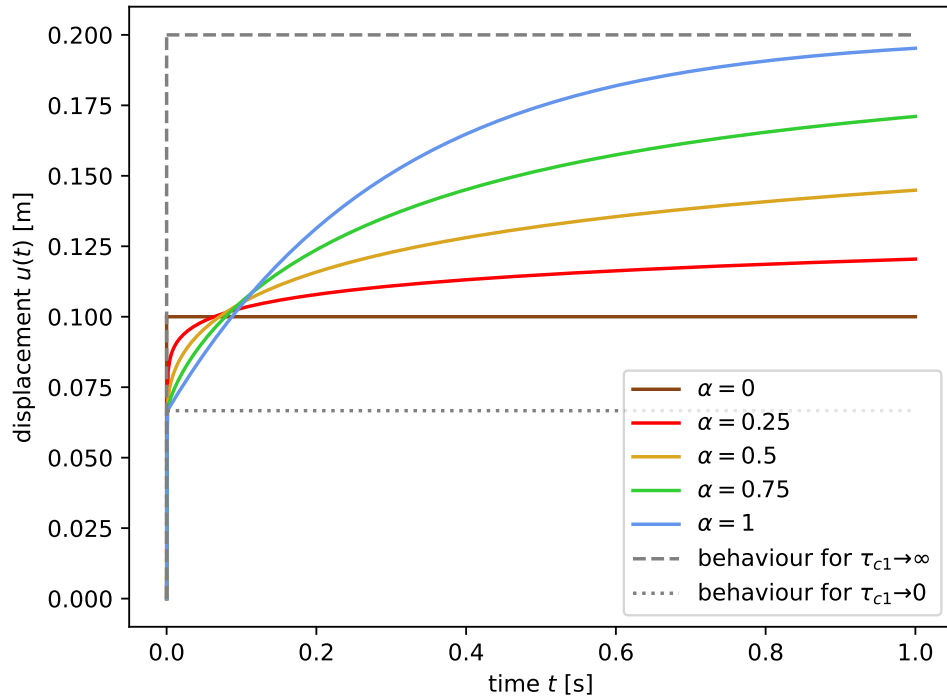

FIGURE 3.16: Static displacement response of fractional Maxwell chain ($N = 1$) to constant force load $\hat{F} = 1$ N

In this case we substitute the constant force load prescribed as $F(t) = \hat{F}$ acting from time $t = 0$. We know that the constant load remains the same in all of the time steps, therefore

$\hat{F} = F^0 = F^1 = \cdots = F^{n+1}$. Figure 3.16 shows the response of 1-cell fractional Maxwell chain loaded by the sudden acting constant force $\hat{F} = 1$ N. The response corresponds to model with parameters given by Tab. 3.1 for varying parameter α_1.

The same as for the previous example, the limit case for $\alpha_1 = 0$ where the springpot becomes purely elastic is plotted by the brown line in the graph and the response corresponds to the response of purely elastic model with stiffness $k_0 + k_1/2$. The limit case for $\alpha_1 = 1$ where the springpot behaviour becomes purely viscous is plotted by the blue line. This reponse is the same as for the standard Maxwell chain loaded by the constant force, as was presented in Section 3.3.1.2, compare with Fig. 3.9. The grey dashed line stands again for the limit case of the characteristic time $\tau_{c1} \to \infty$, where the model behaves as purely elastic with stiffness $k_0 + k_1$. For $\alpha_1 > 0$ the response tends to the same constant value, this is caused by the effect of viscoelastic creep. However, the closer the parameter α_1 is to zero (and therefore to elasticity) the less significant is the creep.

3.4 Dynamic analysis

Dynamic loading, in comparison to the static loading, causes non-negligible acceleration of the structure. Typical examples of the dynamic load are wind, earthquake, traffic load or load caused by the production machines, but even the single force can cause dynamic response if applied rapidly to the structure (or for our simpler problem, to the material model).
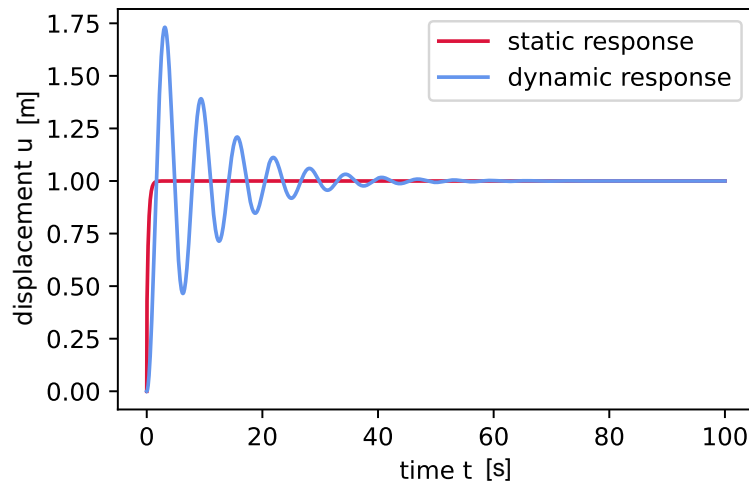

FIGURE 3.17: Static and dynamic response to instantaneous force load

Figure 3.17 compares the static and dynamic response to an instantaneous force load. As is shown, the dynamic response (blue line) oscillates around the static deflection (red line) and finally stabilizes on the static value. The stabilization is caused by the damping effect. Amplitude of the dynamic oscillation can be reduced by a gradual application of the acting force.

For the dynamic analysis we consider the model with the attached mass m shown in Fig. 3.18. The acceleration of the mass results in additional force – the inertia force

induced by the movement of the mass m given by

$$F_{\mathrm{I}}(t) = m\ddot{u}(t), \tag{3.42}$$

where $\ddot{u}$ denotes the second time derivative of displacement, i.e. the acceleration. To describe the dynamic response, the equilibrium condition Eq. (3.16) has to be extended by the inertia force to the following form

$$F(t) = F_0(t) + \sum_{\mathrm{i}=1}^{\mathrm{N}} F_{\mathrm{i}}(t) + F_{\mathrm{I}}(t). \tag{3.43}$$

This equilibrium condition including the inertia force is known as D'Alembert's principle [26], [29]. Since the equilibrium condition includes the displacement in the second time derivative we need to prescribe two initial conditions at t^0, we specify the initial displacement u^0 and the initial velocity $v^0 = \dot{u}^0$. These two initial conditions ensure the uniqueness of the solution.
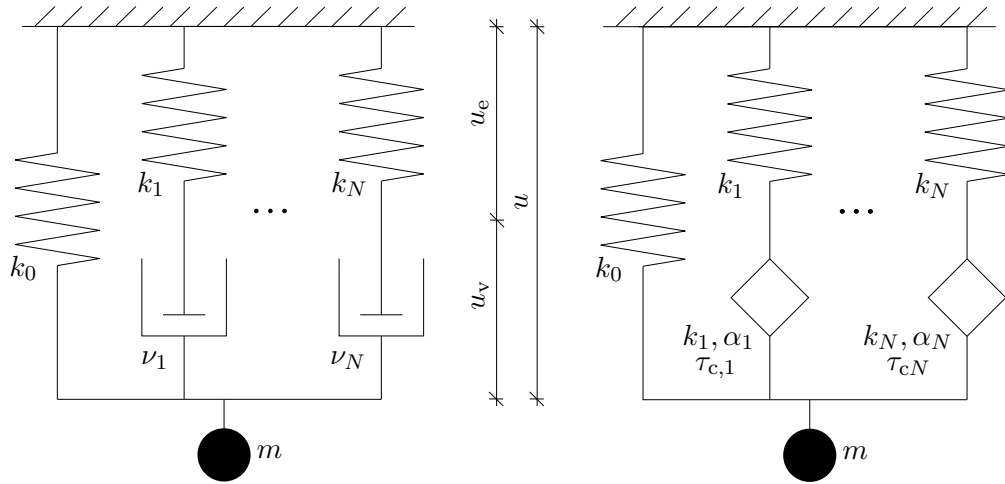

FIGURE 3.18: Standard and fractional Maxwell chain for dynamic analysis

In dynamic analysis we are mainly interested in the displacement response and we distinguish two variants of oscillations. Forced oscillation is consequence of the loading force varying in time. In case of the free oscillation, there is no external force and the oscillation is retrieved from the non-zero initial conditions, i.e. from the prescribed non-zero displacement or velocity [26], [29]. In general, the oscillation response can be analytically prescribed as

$$u(t) = \mathrm{e}^{-\xi_{\mathrm{D}}\omega_0 t} \left(u_{0\mathrm{c}} \cos\omega_{\mathrm{D}} t + u_{0\mathrm{s}} \sin\omega_{\mathrm{D}} t \right) + u_{\mathrm{st}}(t), \tag{3.44}$$

where the damping is represented by the damping ratio $\xi_{\mathrm{D}} \in \langle 0; 1 \rangle$, ω_0 is the natural frequency of undamped oscillation and ω_{D} is a natural frequency of damped oscillation, $u_{\mathrm{st}}(t)$ is the static displacement [26], [29]. As was already mentioned, the dynamic response oscillates around the static response.

Natural frequency of the model can be determined as

$$\omega_0 = \sqrt{\frac{k}{m}}, \tag{3.45}$$

where k is the stiffness of the model and m is the oscillating mass. For the damped oscillation we get its natural frequency as [26]

$$\omega_{\mathrm{D}} = \omega_0 \sqrt{1 - \xi_{\mathrm{D}}^2}. \tag{3.46}$$

In general we can say that $\omega_{\mathrm{D}} < \omega_0$. It is obvious that for an undamped problem where $\xi_{\mathrm{D}} = 0$ we get $\omega_{\mathrm{D}} = \omega_0$ and therefore Eq. (3.44) becomes

$$u(t) = u_{0\mathrm{c}} \cos \omega_0 t + u_{0\mathrm{s}} \sin \omega_0 t + u_{\mathrm{st}}(t), \tag{3.47}$$

The time period of free oscillation attributed to one wave can be then evaluated as

$$T_0 = \frac{2\pi}{\omega_0}, \quad T_{\mathrm{D}} = \frac{2\pi}{\omega_{\mathrm{D}}}. \tag{3.48}$$

The following sections introduces the numerical algorithms to describe either the free or forced oscillation. The behaviour of the standard and fractional Maxwell chains is then discussed on simple examples of a model loaded by an initial displacement, a suddenly acting force or a harmonic force.

3.4.1   Standard Maxwell chain under dynamic load

Moving from the static to the dynamic problem is straightforward. The constitutive laws for the single spring Eq. (3.10) and for i-th Maxwell cell Eq. (3.11) remain unchanged. The difference arises for the equilibrium condition, where we need to include the inertia force and use D'Alembert's condition Eq. (3.43). Therefore, the dynamic response of the standard Maxwell chain is described by the following system of equations

$$F_0(t) = k_0 u(t), \tag{3.49a}$$

$$k_i \dot{u}(t) = \dot{F}_i(t) + \frac{F_i(t)}{\tau_{ci}}, \tag{3.49b}$$

$$F(t) = F_0(t) + \sum_{i=1}^{N} F_i(t) + m\ddot{u}(t), \tag{3.49c}$$

which after introduction of the internal parameter $q_i(t)$ becomes

$$q_0(t) = 0, \tag{3.50a}$$

$$\dot{q}_i(t) + \frac{q_i(t)}{\tau_{ci}} = \frac{k_i u(t)}{\tau_{ci}}, \tag{3.50b}$$

$$F(t) + \sum_{i=1}^{N} q_i(t) = u(t) k_0 + u(t) \sum_{i=1}^{N} k_i + m\ddot{u}(t). \tag{3.50c}$$

This system of equations is solved for an unknown displacement $u(t)$ and internal parameters $q_i(t)$ based on the prescribed evolution of the external force $F(t)$ and initial conditions $u(0)$, $q_i(0)$.

For the discretization we use the differentiation schemes for the first (Eq. (3.1)) and for the second derivative (Eq. (3.2)), respectively. The discretized form of the system

written at $t = t^n$ reads that

$$q_0^n = 0, \tag{3.51a}$$

$$\frac{q_i^{n+1} - q_i^n}{\Delta t} + \frac{q_i^n}{\tau_{ci}} = \frac{k_i u^n}{\tau_{ci}}, \tag{3.51b}$$

$$F^n + \sum_{i=1}^N q_i^n = u^n k_0 + u^n \sum_{i=1}^N k_i + m \frac{u^{n+1} - 2u^n + u^{n-1}}{(\Delta t)^2}. \tag{3.51c}$$

From the discretized state we can express the algorithm to calculate the response at $t = t^{n+1}$ in the following form

$$q_i^{n+1} = \frac{\Delta t}{\tau_{ci}} (k_i u^n - q_i^n) + q_i^n, \tag{3.52a}$$

$$u^{n+1} = \frac{(\Delta t)^2}{m} \left(F^n + \sum_{i=1}^N q_i^n - u^n k_0 - u^n \sum_{i=1}^N k_i) \right) + 2u^n - u^{n-1}. \tag{3.52b}$$

Now we see that to evaluate the displacement u^{n+1} we need to know the values from two previous time nodes u^n and u^{n-1}. This differs from the static problem where the evaluation of u^{n+1} depended on the value from one previous time node only (for the standard Maxwell chain).

For the static problem we prescribed the initial value of the displacement u^0. The dynamic problem requires additional initial condition prescribing the initial velocity $v^0 = \dot{u}^0$. Since the velocity is the first time derivative of the displacement, we can use the approximation of the first derivative by Eq. (3.1) to express the displacement at time t^1 as

$$u^1 = u^0 + v^0 \Delta t. \tag{3.53}$$

Now we base the numerical solution on the known initial values q_i^0, u^0, u^1 and we can evaluate the response in the subsequent time steps.

3.4.1.1 Free oscillation

As was already introduced, the free oscillation is retrieved from the non-zero initial conditions while there is no external force applied to the model. Therefore, in the case of free oscillation the force $F(t) = 0$ and the initial conditions are prescribed as $u(0) = \hat{u}$, $v(0) = \hat{v}$ and $q_i(0) = 0$. The specific example of free oscillation of the standard Maxwell chain is shown in Fig. 3.19. This solution was obtained employing the numerical algorithm given by Eqs. (3.52a)-(3.52b).

The figure shows the dynamic response of 1-cell standard Maxwell chain (parameters given by Tab. 3.1) for varying characteristic time τ_{c1} with the connected mass $m = 1$ kg. This response is retrieved from the prescribed initial displacement $u(0) = 1$ m while the initial velocity remains zero $v(0) = 0$.

The limit cases for the characteristic time τ_{c1} remain the same as was discussed in the previous sections dealing with the static response. In both cases the response is purely elastic, for $\tau_{c1} \to \infty$ with stiffness $k_0 + k_1$ and for $\tau_{c1} \to 0$ with stiffness k_0. The purely elastic behaviour in these limit cases leads to undamped oscillation, as is

plotted by black and red lines in Fig. 3.19. The amplitudes of the displacement during free undamped oscillation remains constant. For intermediate values of the characteristic time the amplitude of the displacement decreases with each wave and finally the response stabilizes on the static value, which for free oscillation is zero, see the green and blue line in the graph. This phenomenon is caused by damping and we talk about the free damped oscillation.
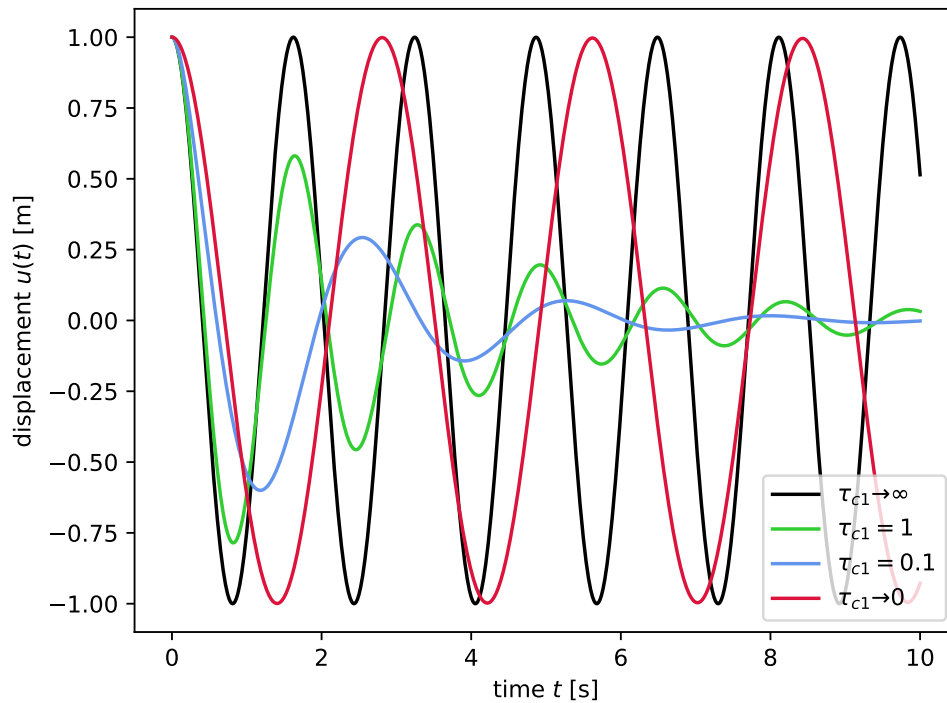

FIGURE 3.19: Free oscillation of standard Maxwell chain ($N = 1$) retrieved from non-zero initial displacement $u(0) = 1$ m
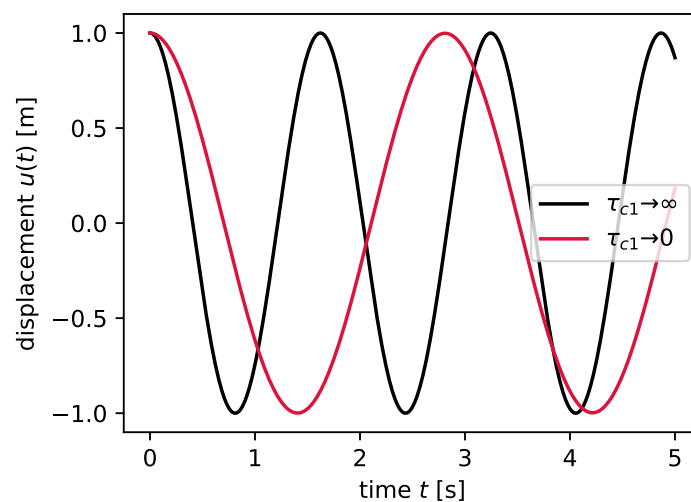
FIGURE 3.20: Frequency of free oscillation of standard Maxwell chain ($N = 1$)

The behaviour corresponding to the limit cases of parameter τ_{c1} is shown in more detail in Fig. 3.20. Both cases ($\tau_{c1} \to \infty$ and $\tau_{c1} \to 0$) represent undamped oscillation, the

maximal amplitudes do not change with each wave and they remain equal to the initial displacement. The difference between these two oscillating movements is their frequency. The natural frequency ω_0 of the model was introduced by Eq. (3.45), it depends on the moving mass and the stiffness of the model. The mass remains unchanged and therefore the difference in frequencies of both cases is caused by their different stiffnesses. For $\tau_{c1} \to \infty$ (the black line) the stiffness is higher as well as the natural frequency and therefore the period of the oscillation is lower. For $\tau_{c1} \to 0$ (the red line), on the other hand, we have lower stiffness which leads to lower natural frequency and longer natural period.

The free oscillation can be retrieved from either non-zero initial displacement or velocity. The example for non-zero initial displacement was shown above. Let's consider the model with the same parameters as for the previous example (Tab. 3.1, $m = 1$ kg) but the initial conditions this time are prescribed as $u(0) = 0$, $v(0) = 1$ m/s. The numerically obtained results are shown in Fig. 3.21. The results are similar as for the previous example – we still get free undamped oscillation for the limit cases of $\tau_{c1} \to \infty$ and $\tau_{c1} \to 0$ and damped oscillation for intermediate values of the characteristic time. For both of the limit cases the response oscillates with the same natural frequency as in the non-zero initial displacement problem. Here we see that the natural frequency does not depend on load or initial conditions but only on the model parameters and mass.
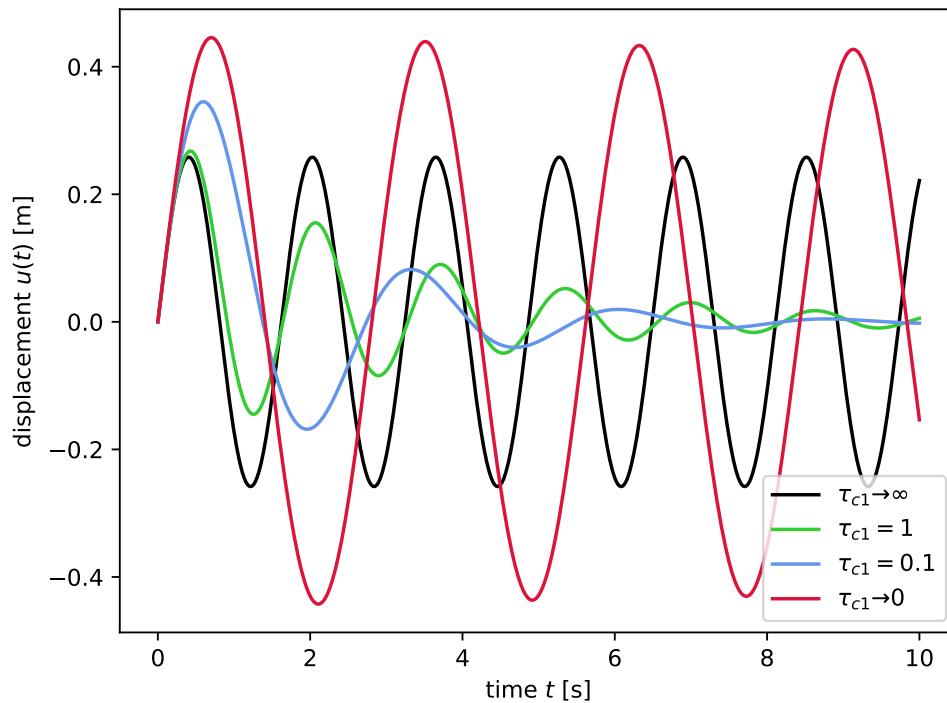

FIGURE 3.21: Free oscillation of standard Maxwell chain ($N = 1$) retrieved from non-zero initial velocity $v(0) = 1$ m/s

The difference in comparison to the previous example arises with the amplitudes. In the previous case the amplitudes were clearly given by the condition of initial displacement. To evaluate the amplitude in the non-zero initial velocity problem we use the general equation for the undamped harmonic oscillation Eq. (3.47). Note that for the free oscillation the static displacement u_{st} is zero. By substitution of the initial conditions

$u(0) = 0$, $v(0) = \hat{v}$ the equation becomes

$$u(t) = \frac{\hat{v}}{\omega_0} \sin \omega_0 t, \qquad (3.54)$$

from which we get the displacement amplitude $\hat{v}/\omega_0$. Now it is clear that the amplitudes depend on the natural frequency of the model – higher natural frequency (which goes hand in hand with higher model stiffness) leads to lower amplitudes and vice versa. This is clearly shown in Fig. 3.21 where for the more compliant limit case $\tau_{c1} \to 0$ (with only acting stiffness k_0) the displacement amplitudes are higher than for the other cases with co-acting stiffness k_1.

3.4.1.2   Sudden acting force

In the previous section we discussed the free oscillation. This state occurs for zero loading force $F(t) = 0$ and non-zero initial conditions, in general prescribed as $u(0) = \hat{u}$, $\dot{u}(0) = v(0) = \hat{v}$. On the contrary, the response to forced oscillation depends on the prescribed evolution of the loading force $F(t)$ while we base the solution on zero initial conditions $u(0) = 0$, $v(0) = 0$. Here we introduce the simple example of loading by the sudden acting force, which is instantaneously applied to the model at $t = 0$ and remains constant since. However, the loading force can be prescribed arbitrarily and the response can be still solved using the numerical algorithm given by Eqs. (3.52a)-(3.52b).
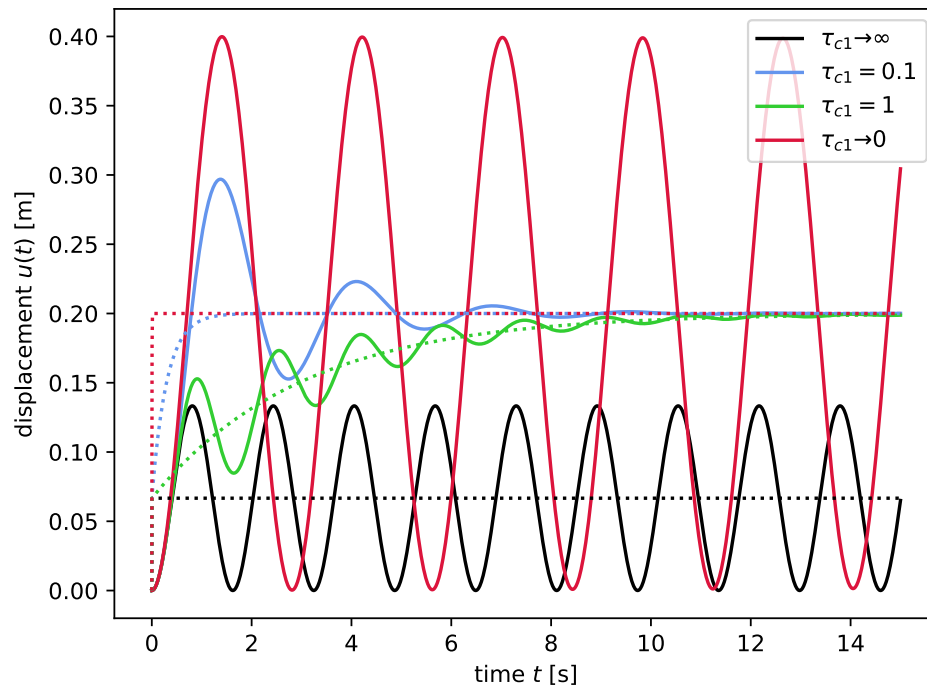

FIGURE 3.22: Oscillation of standard Maxwell chain ($N = 1$) retrieved from sudden acting force $F(t) = 1$ N

Figure 3.22 shows the numerically computed response of 1-cell standard Maxwell chain loaded by the sudden acting force $F(t) = 1$ N at $t = 0$. Parameters of the model were set the same as for the previous examples (Tab. 3.1, $m = 1$ kg).

As we already know, the limit cases for the characteristic times $\tau_{c1} \to 0$ and $\tau_{c1} \to \infty$ lead to the elastic problem and therefore to undamped oscillation. After the substitution of zero initial conditions to general solution for undamped oscillation given by Eq. (3.47) we can express the analytical solution of this problem as

$$u(t) = u_{st} - u_{st} \cos \omega_0 t. \tag{3.55}$$

Now it is clearly shown that the response oscillates around the static displacement u_{st} with the oscillation amplitude u_{st}. Therefore, the maximal value of the displacement is double the static value.

The static response corresponding to this loading process was already discussed in Section 3.3.1.2 and the results are plotted in Fig. 3.22 by the dotted lines. It is clearly shown that the dynamic response oscillates around the static one. The limit behaviour for $\tau_{c1} \to \infty$ and $\tau_{c1} \to 0$ leads to purely elastic response with constant (undamped) oscillation amplitude. The response for intermediate values of τ_{c1} shows a significant creep and damping effect to oscillation amplitudes.

3.4.1.3 Harmonic force load

As the last example for the standard Maxwell chain we show the response to loading by a harmonic force. The force is given by the sin function with the prescribed amplitude and frequency. The response to this type of load is, in general, a combination of two harmonic functions, see Fig. 3.23.
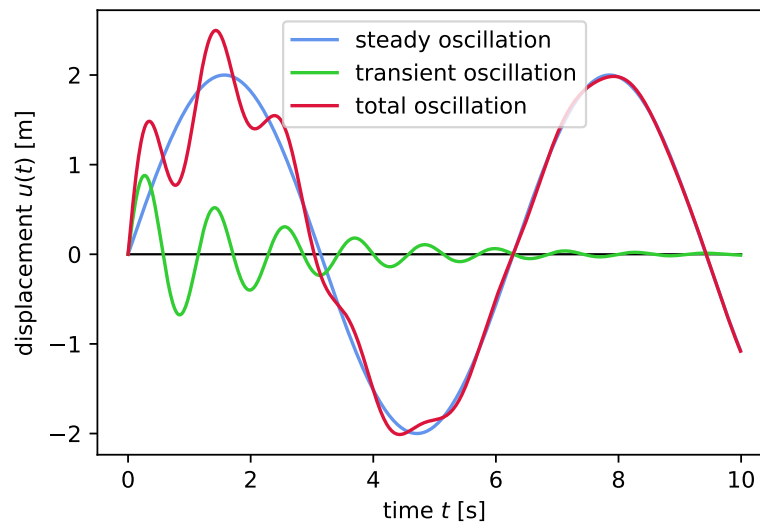

FIGURE 3.23: General example of dynamic response to loading by harmonic force –
transient and steady oscillation

The green line in the graph depicts the transient oscillation. This partial response is caused by the sudden introduction of the harmonic load. It oscillates with the natural frequency of the model and the effect of this transient oscillation disappears over time due to damping. The steady response (plotted by the blue line in the graph) oscillates with the excitation frequency of the loading force. Amplitudes of the steady response are not damped, however, the damping causes the phase shift from the load. The total

response is given as the sum of these two partial responses. This is depicted by the red line. It is clear that after damping the transient oscillation the response stabilizes and matches the steady one.

This behaviour can be described analytically as well. Recalling Eq. (3.44), the response to sinusoidal force load can be written in the form

$$u(t) = e^{-\xi_D \omega_0 t} \sin(\omega_D t + \delta_D) + u_0 \sin(\omega t + \delta). \tag{3.56}$$

The first term on the right side of the equation represents the transient oscillation with the damped natural frequency ω_D, the damping is a consequence of the damping ratio ξ_D. The second term then represents the steady response oscillating with excitation frequency ω, amplitude u_0 and phase shift δ. It is obvious that the effect of the transient response decreases in time. For this reason, when solving the long-term response only, the steady oscillations are taken into account [26].

Figure 3.24 shows the response of 1-cell standard Maxwell chain with parameters stored in Tab. 3.1, $m = 1$ kg and varying τ_{c1} to harmonic force $F(t) = \sin 0.5t$ N acting from $t = 0$. Until $t = 0$ we assume no load and the initial conditions can be prescribed as $u(0) = 0$, $v(0) = 0$, $q_i(0) = 0$. The response was obtained from the numerical algorithm given by Eqs. (3.52a)-(3.52b).

The black line in Fig. 3.24 depicts the response in the limit case $\tau_{c1} \to \infty$ when we get the purely elastic response with stiffness $k_0 + k_1$. In this case we clearly see the steady response in phase with the load. The transient response oscillating with the natural frequency does not disappear over time, because for this limit case there is no damping. The green line represents the response for $\tau_{c1} = 1$. For this case we see just a hint of a transient response which is quickly damped. Also we see the phase shift between the response and the loading force which is caused by the damping effect.
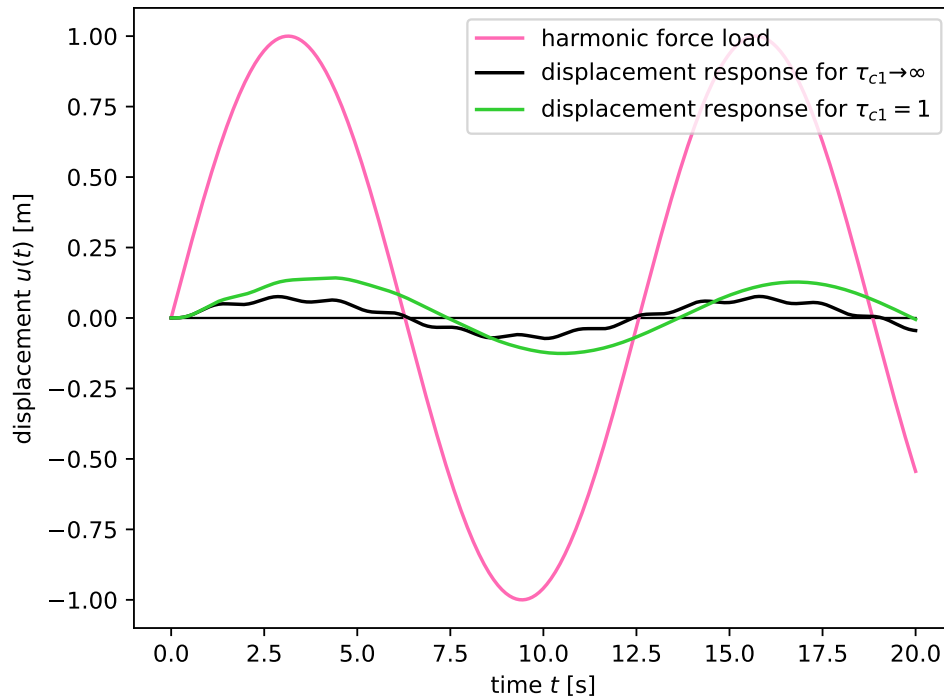

FIGURE 3.24: Displacement response of standard Maxwell chain ($N = 1$) loaded by harmonic force $F(t) = \sin 0.5t$ N

3.4.2   Fractional Maxwell chain under dynamic load

The behaviour of fractional Maxwell chain under dynamic load can be described by the system of equations including the Hooke law (Eq. (3.10)) describing the single spring, constitutive law describing i-th fractional Maxwell cell (Eq. (3.12)) and the equilibrium condition including the inertia forces (Eq. (3.43)). The final system of equations reads

$$F_0(t) = k_0 u(t), \tag{3.57a}$$

$$k_i D^{\alpha_i} u(t) = D^{\alpha_i} F_i(t) + \frac{F_i(t)}{\tau_{ci}^{\alpha_i}}, \tag{3.57b}$$

$$F(t) = F_0(t) + \sum_{i=1}^{N} F_i(t) + m\ddot{u}(t). \tag{3.57c}$$

Introduction of the internal parameter $q_i(t)$ (Eq. (3.17)) rewrites the system of equations to the form

$$q_0(t) = 0, \tag{3.58a}$$

$$D^{\alpha_i} q_i(t) + \frac{q_i(t)}{\tau_{ci}^{\alpha_i}} = \frac{k_i u(t)}{\tau_{ci}^{\alpha_i}}, \tag{3.58b}$$

$$F(t) + \sum_{i=1}^{N} q_i(t) = u(t)k_0 + u(t)\sum_{i=1}^{N} k_i + m\ddot{u}(t). \tag{3.58c}$$

For discretization of the problem at time t^n we use the approximation of the fractional derivative given by Eq. (3.3) and the approximation for the second derivative given by Eq. (3.2).

$$q_0{}^n = 0, \tag{3.59a}$$

$$\frac{1}{(\Delta t)^{\alpha_i}} \sum_{j=0}^{n} w_j(\alpha_i) q^{n+1-j} + \frac{q_i^n}{\tau_{ci}^{\alpha_i}} = \frac{k_i u^n}{\tau_{ci}^{\alpha_i}}, \tag{3.59b}$$

$$F^n + \sum_{i=1}^{N} q_i^n = u_0^k + u^n \sum_{i=1}^{N} k_i + m\frac{u^{n+1} - 2u^n + u^{n-1}}{(\Delta t)^2}. \tag{3.59c}$$

The algorithm to calculate the response at $t = t^{n+1}$ can now be expressed as

$$q_i^{n+1} = \frac{(\Delta t)^{\alpha_i}}{\tau_{ci}^{\alpha_i}} \left(k_i u^n - q_i^n \right) - \sum_{j=1}^{n} w_j(\alpha_i) q^{n+1-j}, \tag{3.60a}$$

$$u^{n+1} = \frac{(\Delta t)^2}{m} \left(F^n + \sum_{i=1}^{N} q_i^n - u^n k_0 - u^n \sum_{i=1}^{N} k_i \right) + 2u^n - u^{n-1}. \tag{3.60b}$$

The system of equations is supplemented by the prescribed initial conditions q_i^0, u^0 and $v^0 = \dot{u}^0$. With the use of the formula for approximation of the first derivative given by Eq. (3.1) we can express the displacement u^1 as

$$u^1 = u^0 + v^0 \Delta t. \tag{3.61}$$

The numerical solution is then based on the initial values q_i^0, u^0, u^1.

3.4.2.1 Free oscillation

For the example of free oscillation we assume no external force, $F(t) = 0$, and non-zero initial condition for displacement or velocity. Figure 3.25 shows the response of 1-cell fractional Maxwell model retrieved from the initial displacement $u^0 = 1$ m, $v^0 = 0$. The parameters of the model are given by Tab. 3.1, $m = 1$ kg and the results are shown for varying parameter α_1.
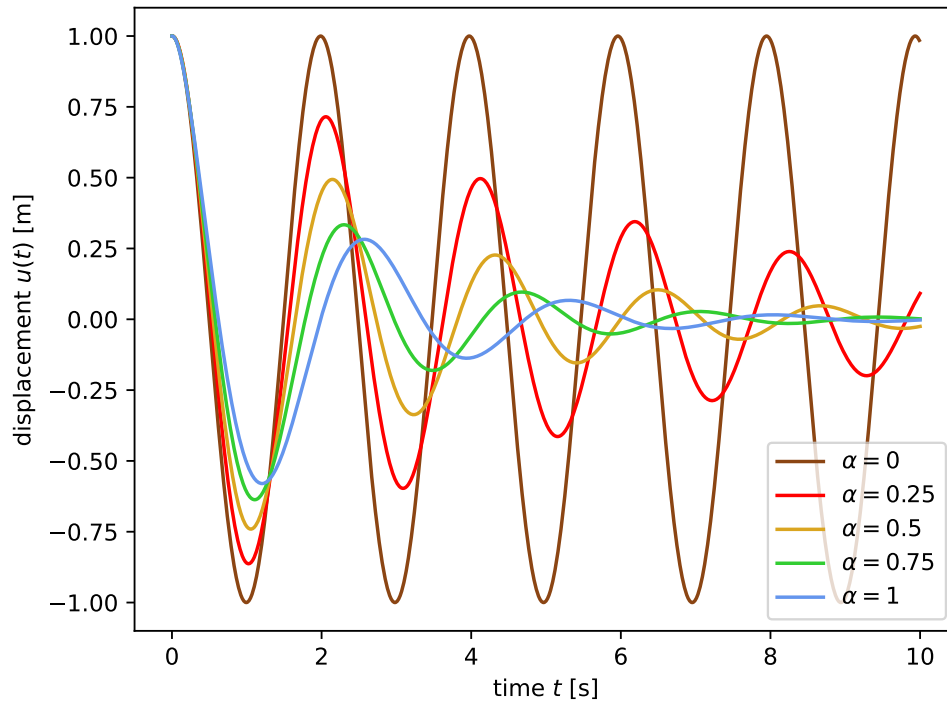

FIGURE 3.25: Free oscillation of fractional Maxwell chain ($N = 1$) retrieved from non-zero initial displacement $u^0 = 1$ m

This example clearly shows the influence of the parameter α_1. For $\alpha_1 = 0$ the springpot behaves as spring and we get purely elastic behaviour with stiffness $k_0 + k_1/2$, see the brown line in the graph. For increasing parameter α_1 the springpot becomes more and more viscous and finally for the limit case $\alpha_1 = 1$ (blue line in the graph) the fractional element becomes purely viscous and the behaviour of the fractional model in this limit case corresponds to the behaviour of the standard Maxwell chain.

Viscosity of the springpot has a direct influence on damping of the model. With increasing parameter α_1 we see a gradual increase of damping. In general, damping results in decrease of amplitudes in time and also decrease of the natural frequency of the oscillation. As was introduced earlier by Eq. (3.46), the natural frequency of damped oscillation is lower than for undamped oscillation. Lower natural frequency leads to longer natural period of the oscillation. Both of these phenomena are clearly visible in Fig. 3.25 – the closer is the behaviour of springpot to a standard viscous model (i.e. the closer is parameter α_1 to one), the more pronounced the damping is and the slower is the oscillation.

3.4.2.2 Sudden acting force

At this moment we are going to discuss the response to a sudden acting force applied to the fractional Maxwell model. The parameters of the model are kept the same as for the previous examples (Tab. 3.1, $m = 1$ kg), the springpot parameter α_1 is assumed to vary. The initial conditions are set as $u^0 = 0$, $v^0 = 0$, $q_i^0 = 0$. The force $F(t) = 1$ N is applied instantaneously at $t = 0$. The response shown in Fig. 3.26 was obtained via numerical solution of Eqs. (3.60a)-(3.60b).
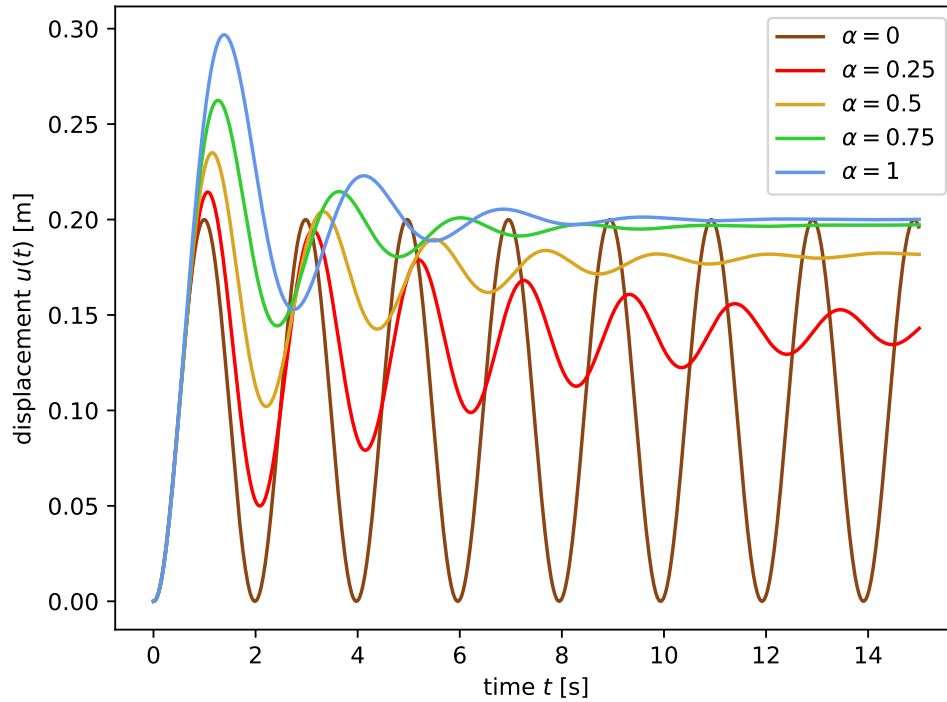
FIGURE 3.26: Oscillation of fractional Maxwell chain ($N = 1$) retrieved from sudden acting force $F(t) = 1$ N

In the graph we see several of the previously mentioned phenomena. With increasing parameter α_1 the response is more damped which leads to a more significant decrease of amplitudes over the time and also to prolonging the oscillation period. For $\alpha_1 = 1$ we get the same response as for the standard Maxwell chain discussed in Section 3.4.1.2. Limit case for $\alpha_1 = 0$ gives us purely elastic response with stiffness $k_0 + k_1/2$.

For damped oscillation the displacement stabilizes on the value corresponding to the static displacement. For $\alpha_1 > 0$ there is a significant effect of creep which causes an increase of the static displacement with time. The stabilized displacement is the same for $\alpha_1 > 0$, however, for $\alpha_1 \to 0$ the behaviour of the springpot is closer to the elastic one which reduces the effect of creep and the convergence to the limit value is slower.

3.4.2.3 Harmonic force load

As the last example in this chapter we introduce the fractional Maxwell chain loaded by the harmonic force prescribed as $F(t) = \sin 0.5t$ N. The response of 1-cell chain was

examined for model parameters prescribed in Tab. 3.1, $m = 1$ kg and variable value of parameter α_1. The numerical algorithm of Eqs. (3.60a)-(3.60b) supplemented by the aforementioned inputs and initial conditions $u(0) = 0$, $v(0) = 0$, $q_i(0) = 0$ gives the result shown in Fig. 3.27.
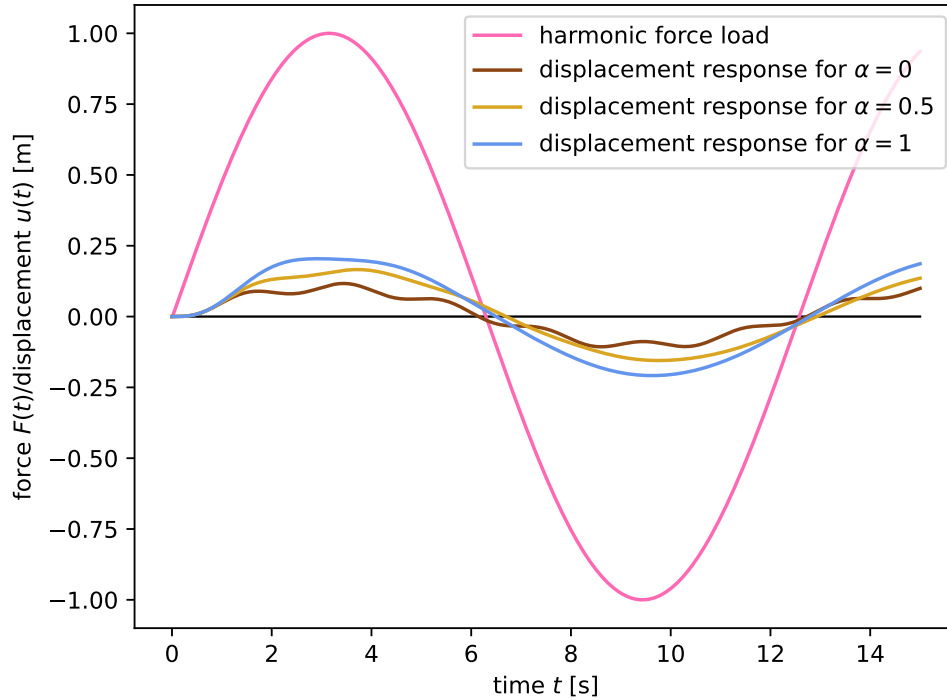

FIGURE 3.27: Displacement response of fractional Maxwell chain ($N = 1$) loaded by harmonic force $F(t) = \sin 0.5t$ N

The figure clearly shows that for the limit case $\alpha_1 = 0$ we get the undamped purely elastic response whose steady component oscillates in phase with the load. For the elastic behaviour the transient oscillation remains undamped over time. With increasing the springpot parameter α_1 we increase the damping effect. The damping results in a faster disappearance of transient oscillations and in an increase of the phase shift. For the limit case $\alpha_1 = 1$ the springpot behaves as a dashpot and the response of the fractional Maxwell chain becomes the same as for the standard Maxwell chain.

3.5   Discussion of the results

The numerical algorithms presented in this chapter were derived for the general Maxwell chain with N connected Maxwell cells and also for both the force and displacement driven loading. Therefore, if we know the loading function or at least its values in individual nodal points the response of the standard or fractional Maxwell chain model can be obtained. In this chapter, the functionality of the algorithms was shown for specific loading scenarios for which we can simply predict the model response or for some limit cases to even obtain analytical solutions. It was shown that for a sufficiently small time step the numerical response match the analytical solution well and it can be used to approximate the solution in the cases where obtaining the analytical solution would be too difficult or impossible.

However, the numerical study also brought up the problem associated with the fractional model. We talk about the time consumption of the calculation which is many times higher for the fractional model than for the standard one. For instance, we consider the static response to a constant force load. The corresponding response was presented in Section 3.3.1.2 for the standard Maxwell chain and in Section 3.3.2.2 for the fractional Maxwell chain. The approximate response was calculated with the use of Python script. To obtain the response in 10000 time steps for 1-cell Maxwell chain with fixed parameters the computational time was around 0.3 s for the standard model. For the fractional model, however, we arrive at times around 10 s.

This massive difference in computation times arises from the numerical approximations of derivatives. The first derivative approximation using Eq. (3.1) depends on the two latest nodal values of the function. For the fractional derivative the approximation given by Eq. (3.3) depends on the whole evolution of the function in previous time nodes. This means that for the standard Maxwell chain the static response in the following node depends on the value from the actual node only. For the fractional Maxwell chain we need to consider all of the nodal values since the beginning of loading and the weight of each individual value differs in each time step (the older the value is the lower is its influence to the following evolution of response).

In Chapter 2 the models based on the fractional viscoelasticity were introduced as a promising tool to describe the material behaviour. The fractional Maxwell chain can sufficiently describe the behaviour of material with lower number of cells (and therefore less parameters) than the standard Maxwell chain. However, if we want to solve the response numerically, the advantages of the fractional model are overshadowed by many times longer computation times than we need for the standard Maxwell chain.

Chapter 4

Experimental analysis of PVB foil

In Chapter 2 we introduced the theoretical models used to describe viscoelastic materials. Each model has its free parameters such as stiffness or coefficient of viscosity. The behaviour of the theoretical model depends on the values of these parameters. We want the model to behave as close as possible to the real behaviour of the material being described. To achieve this goal we need to calibrate the model – find the parameters based on the experiments performed on the material.

While the theoretical models have been, for simplicity, described in a plane of forces and displacements, the experimental analysis works in the stress-strain regime. Specifically for our experimental setup, the shear stress and shear strain. All of the mathematical relationships from Chapter 2 with force F, displacement u, stiffness k and viscosity coefficient ν can be rewritten analogously for shear stress τ, shear strain γ, shear modulus G and coefficient of viscosity η.

FIGURE 4.1: Dynamic shear rheometer Malvern KINEXUS

Our goal was to experimentally analyze polyvinyl butyral, the most frequently used material for the interlayer of laminated glass. The purpose of the interlayer is to ensure binding between individual glass plates. For the laminated glass element in bending the interlayer is loaded mostly in shear. Therefore, we are interested mostly in shear properties of the polymer. Experiments focused on obtaining shear properties of the material can be provided by loading the material in simple torsion with the use of dynamic shear rheometer.

4.1 Rheometer experiment

Rheometer is a device used to determine rheological properties of materials. For the viscoelastic material it is able to measure both the elastic and viscous properties. In [32] different types of rheometer geometry are introduced. For the purposes of this research we used the dynamic shear rheometer (DSR) with parallel-plate configuration, specifically the Malvern KINEXUS DSR+, see the photograph in Fig. 4.1.

The scheme of the parallel-plate geometry is shown in Fig. 4.2 (a) while Fig. 4.2 (b) shows the photograph of the same configuration. The sample is attached between the two parallel plates. The upper plate, i.e. the adapter, can move along and rotate around the vertical axis perpendicular to the plate. The bottom plate, i.e. the stator, is fixed. The torsional load is introduced to sample via rotation of the adapter. The loading process can be controlled by shear stress or strain and the rheometer can perform static loading (e.g. the creep test) or the dynamic loading. The dynamic rheometer test on laminated glass samples is introduced in [1] and this experimental configuration was also used in our research.
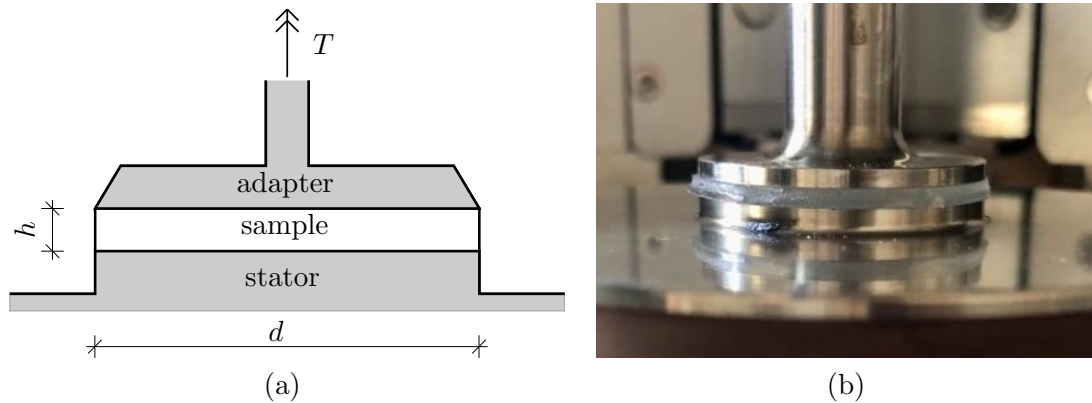

FIGURE 4.2: Parallel-plate rheometer with attached sample – (a) scheme, (b) photograph

The sample is loaded by a harmonic (sinusoidal) strain while the stress response is monitored by the rheometer. An example of the recorded evolution of stress and strain is shown in Fig. 4.3. The software then extracts the values of amplitudes of strain γ_0 and stress τ_0 and the phase shift δ between the load and the response. These values are converted into the required outputs – the storage modulus G', the loss modulus G'' and the complex modulus G^*. All of these quantities were introduced in Chapter 2, which is drawn in parallel to the storage, loss and complex stiffnesses k', k'', k^*, respectively.

The moduli are given by

$$G'(\omega) = \frac{\tau_0}{\gamma_0} \cos \delta,$$

$$G''(\omega) = \frac{\tau_0}{\gamma_0} \sin \delta, \tag{4.1}$$

$$G^*(\omega) = G'(\omega) + iG''(\omega).$$

The rheometer outputs are based on the known diameter of the rheometer plates d and the gap between the plates, which corresponds to the thickness of the sample h. For the Malvern KINEXUS DSR+ rheometer with the diameter of the plates $d = 25$ mm, the maximum height of the sample is 5 mm. The rheometer software assumes the sample perfectly filling the gap between the plates as is shown in Fig. 4.2 (a) – the same diameter of the sample and of the plates, the sample is homogeneous over its height.
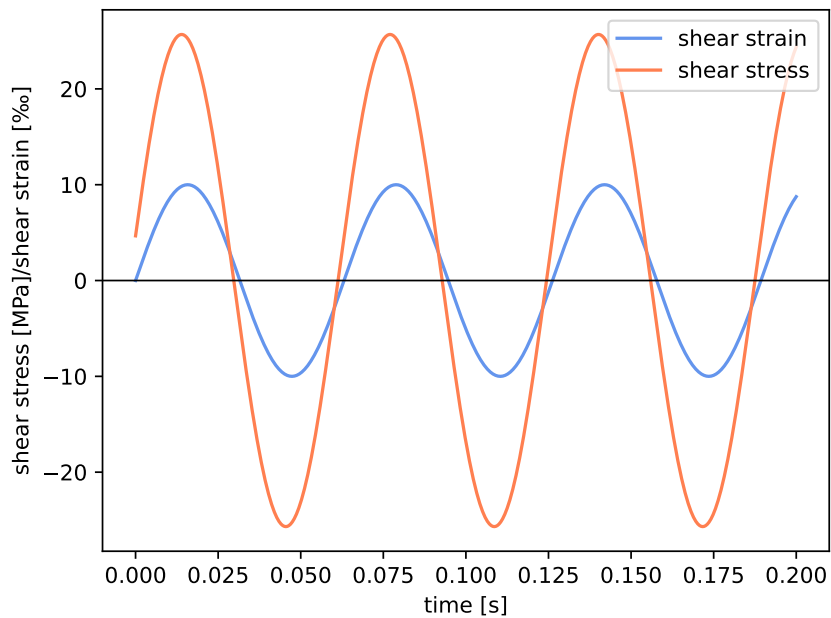
FIGURE 4.3: Rheometer record of strain and stress

4.1.1 Sample preparation

The experiments on PVB are usually performed on the laminated glass (LG) samples, i.e. glass-PVB-glass configuration. The main advantage of LG samples is that the composite is industrially produced (in autoclave under high pressure and temperature) and the specimen is drilled directly from the composite. Therefore, if any property changes during the manufacturing process the sample takes it into account. The disadvantage of LG sample is the inhomogeneity over its height and (usually) different diameter of the sample compared to the rheometer plates. These differences in geometry cause the need of transformation of the rheometer outputs with respect to actual geometry of the PVB interlayer. Laminated glass samples need to be attached to the rheometer by glue, which requires additional time to attach and remove the sample. Experimental analysis on LG

samples is described in more detail in [13], [31], [1]. The data obtained in [13] are used in this thesis for the reference and comparison to our experimental results.

As was mentioned earlier, the Malvern KINEXUS rheometer allows us to use a sample of the maximum height of 5 mm. The LG samples are not able to meet this requirement and therefore, in this research we analyzed the samples of PVB itself (not as a part of LG composite). The material is supplied in the form of rubber-like foil – in this form the material is before the lamination between the glass plates. The experimental analysis was performed on two different thicknesses of PVB foil, 0.76 mm and 1.52 mm. The foil can be easily cut to the exact size to fit the rheometer plates properly. With no glass plates the sample is also homogeneous over its thickness. With PVB we meet the assumption of a homogeneous sample perfectly filling the gap between the plates and therefore the outputs given by the rheometer corresponds directly to the parameters of PVB with no need for transformation.

4.1.1.1 Attachment of sample

When the sample is cut to the required size it has to be attached to the plates. Compared to tests on LG, glue is not needed for the attachment of the PVB sample. Remember that PVB is supplied in the form of foil, ready to be laminated between two glass plates. Therefore, the foil can be attached to rheometer plates using the same principle as for the laminated glass lamination – employing high temperature and compressive force introduced by the adapter.

The laminated glass composite is industrially produced with the use of autoclave which allows exposing the composite to high temperatures and omnidirectional pressure. The manufacturer prescribes the process of lamination using temperatures $130 - 140$ °C with $12 - 14$ bar pressure acting for 20 minutes at least [34]. We are not able to precisely replicate this lamination process. We are limited mainly by the pressure. However, with some modifications a similar process can be used for the PVB sample attachment.
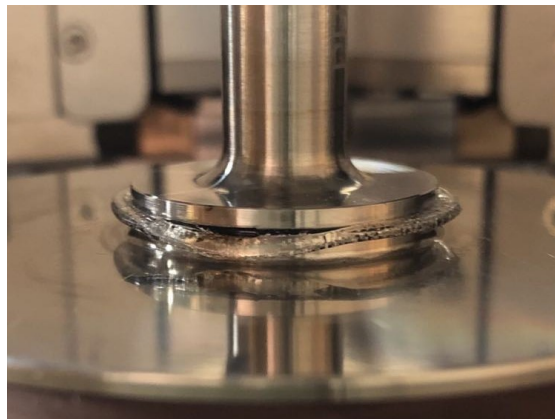

FIGURE 4.4: PVB extruded to the sides of rheometer plates

The lamination process used to attach the sample to rheometer plates exposed the sample to temperature of 100 °C or 140 °C together with a compressive normal force of 5 N for the period of 45 minutes. The temperature of 140 °C corresponds better to the temperature prescribed by the manufacturer. However, for this temperature the sample becomes viscous liquid and due to acting normal force it is extruded to the sides

of rheometer plates. This phenomenon is shown in Fig. 4.4 and it leads to decrease of thickness of the sample. Extruded material needs to be cut off before starting the measurements.
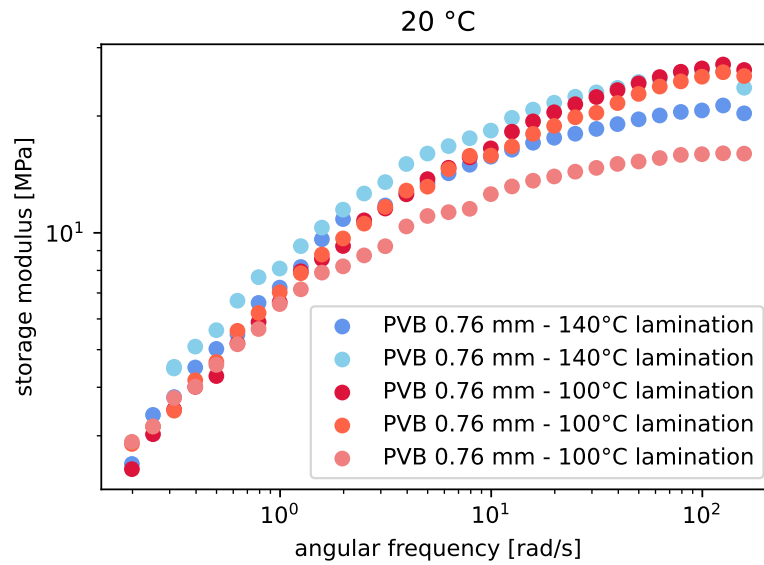

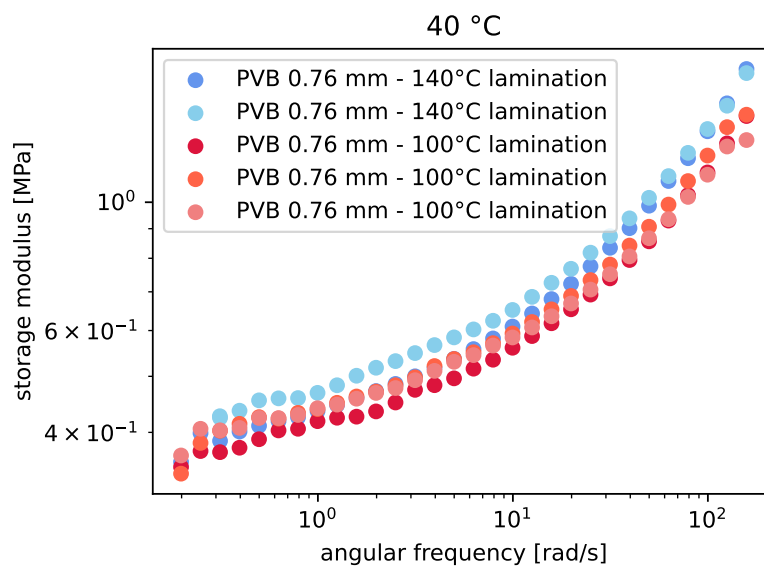FIGURE 4.5: Experimental results comparing different lamination temperature – measurement for 20 °C

FIGURE 4.6: Experimental results comparing different lamination temperature – measurement for 40 °C

We prefer the lamination under the temperature of 100 °C. In this case, the sample remains in a solid state, there is no extrusion of the material and therefore no need for an additional adjustment of the sample. The experimental analysis proved that even for the lower temperature (100 °C) the attachment of the sample is strong enough and no slippage occurs during the measurements. Figures 4.5 and 4.6 show the comparison of data obtained on samples laminated at 100 °C (red) and at 140 °C (blue). In general

we may conclude that the obtained measurements match fairly well. Especially, if the deviations evident for lower temperatures of higher frequencies were observed even for samples laminated under same conditions. Therefore, these deviations cannot be blamed simply on the different lamination processes.

After the lamination process is completed the sample is cooled to the required temperature and becomes ready for the measurement.

4.1.2 Measurement scenario

Our main goal is to obtain the storage and loss moduli of the material. The behaviour of PVB is strongly dependent on temperature and loading time. To provide proper description of the material it is necessary to perform experiments for multiple temperatures and frequencies. The Malvern KINEXUS rheometer has a temperature chamber, which is shown in Fig. 4.7. The temperature chamber ensures constant temperature during the measurement, fluctuation of temperature inside the chamber is limited to ± 0.01 °C.
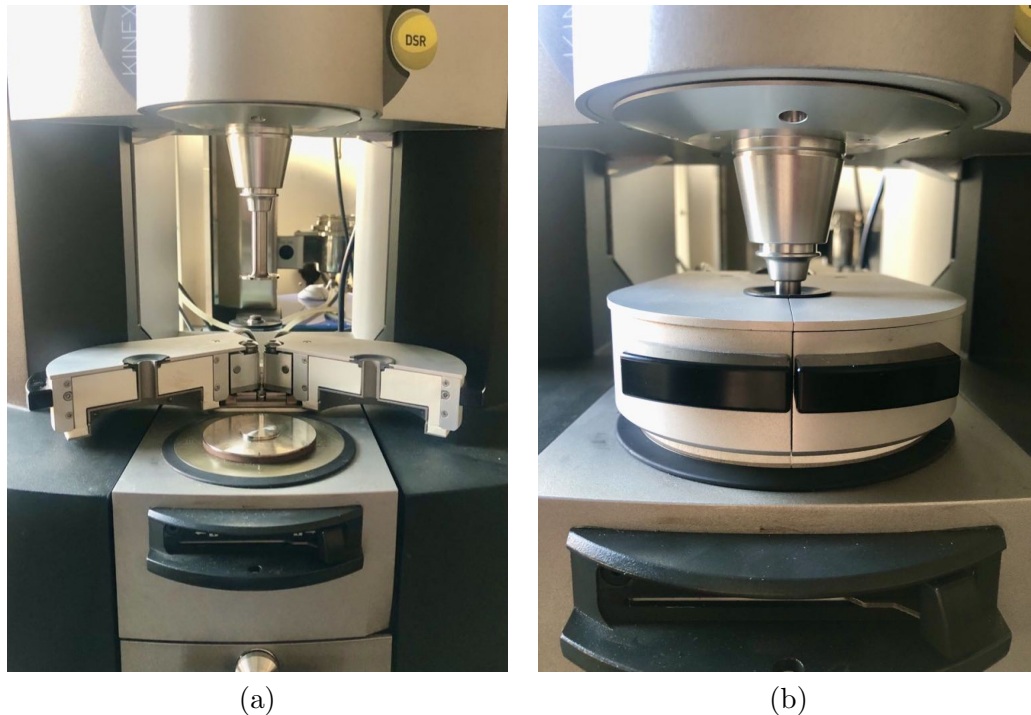

(a) (b)

FIGURE 4.7: Temperature chamber of Malvern KINEXUS rheometer – (a) open, (b) closed

The time dependent behaviour is analyzed by a frequency sweep test. This test prescribes sinusoidal strain of a constant amplitude for various frequencies. Amplitude of the strain load needs to be set with respect to the linear region of viscoelastic behaviour, which can be simply determined by performing the linearity test.

4.1.2.1 Linearity test

If the material is loaded within its linear viscoelastic region (LVR) no permanent deformation occurs and the viscoelastic material parameters are load independent. Load

exceeding the LVR causes changes in microstructure and leads to nonlinear behaviour of the material [38]. In this research, all of the previously derived expressions are valid for the linear viscoelasticity only. Therefore, it is important to determine the LVR of the material behaviour and set the amplitude of frequency sweep test safely within this region.
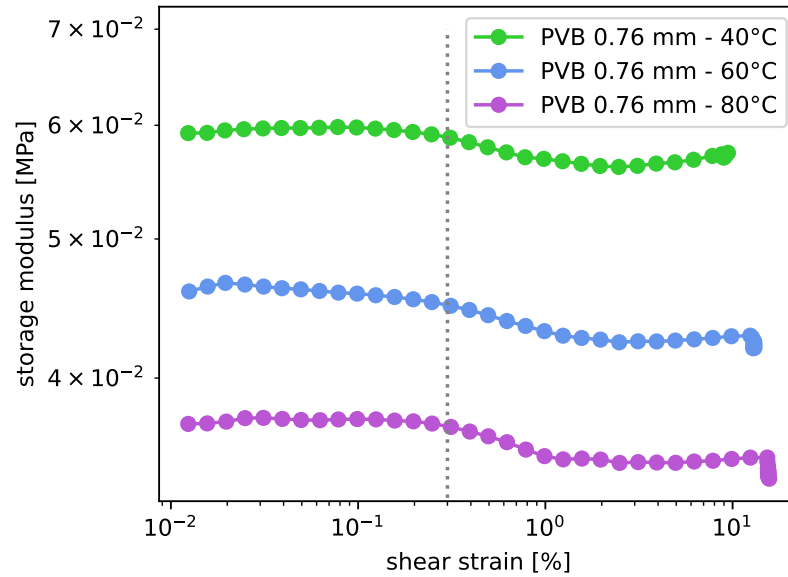

FIGURE 4.8: Linear viscoelastic region of PVB

The linearity test is performed for a constant frequency and a varying (increasing) amplitude of the harmonic load. The linear region can be simply determined from the progress of storage modulus G'. Within LVR the values of the modulus remain constant and do not change with the applied strain. After reaching the limit of LVR, i.e. the critical strain, the storage modulus starts to drop [38].

This test was performed on PVB samples for frequency of 1 Hz and various temperatures. Figure 4.8 shows the results for selected temperatures where the behaviour is clearly shown. For shear strain under approximately 0.3 % we see the constant value of the storage modulus. Fluctuation of the modulus is noticeable for higher values of strain and the limit of the measurement is at approximatelly 10 %.

4.1.2.2 Frequency sweep test

The frequency sweep test allows us to obtain the dynamic moduli of the material. Based on the linearity test we prescribed the amplitude of strain as 0.1 % to measure safely within LVR.

The measurements were performed for frequencies in the range of 0.01-100 Hz (approximately 0.0628-628) rad/s. This range has been established with regard to measurement times – one test for this range of frequencies took a little over 30 minutes and such a test must be run multiple times for several different temperatures. Between the tests we need approximately additional 20 minutes to temper the sample for a given temperature.

The material was analyzed for the following range of temperatures: 0 °C, 10 °C, 20 °C, 30 °C, 40 °C, 60 °C, 80 °C, 100 °C. Note that not all of the measurements were provided for the full temperature range. At the beginning we measured in the range of 0-100 °C with increments of 20 °C. Then, partial evaluation of the measured data was carried out to suggest adding several intermediate temperatures (10 °C and 30 °C) and to focus mainly on temperatures in the range of 10-80 °C. Therefore, the measurements at 0 °C and 100 °C were not provided for all samples.

Sample label	Thickness	Lamination	Tested temperatures
00-PVB-0.76	0.76 mm	140 °C	0, 10, 20, 30, 40, 60, 80, 100 °C
01-PVB-0.76	0.76 mm	100 °C	0, 20, 40, 60, 80, 100 °C
02-PVB-0.76	0.76 mm	100 °C	10, 20, 30, 40, 60, 80 °C
03-PVB-0.76	0.76 mm	100 °C	0, 10, 20, 30, 40, 60, 80 °C
01-PVB-1.52	1.52 mm	100 °C	0, 20, 40, 60, 80, 100 °C
02-PVB-1.52	1.52 mm	100 °C	10, 20, 30, 40, 60, 80 °C
03-PVB-1.52	1.52 mm	100 °C	10, 20, 30, 40, 60, 80, 100 °C

TABLE 4.1: List of samples

The experimental analysis was performed on six samples – three having the thickness of 0.76 mm and three with the thickness of 1.52 mm, all of them laminated at 100 °C. For reference we provide also results from the measurement on 0.76 mm sample laminated at 140 °C. List of the samples with their labels is summarized in Tab. 4.1. The data obtained from the rheometer experiment for each sample are presented in the next section.

4.2 Results from rheometer

This section shows the rheometer outputs for the storage and loss moduli. Figures 4.10 and 4.11 show the results for samples of the thickness of 0.76 mm and 1.52 mm, respectively. Figure 4.9 stands for the 0.76 mm sample laminated at 140 °C. Individual graphs are labeled according to Tab. 4.1. The results clearly show the frequency and temperature dependence of the storage and loss moduli.
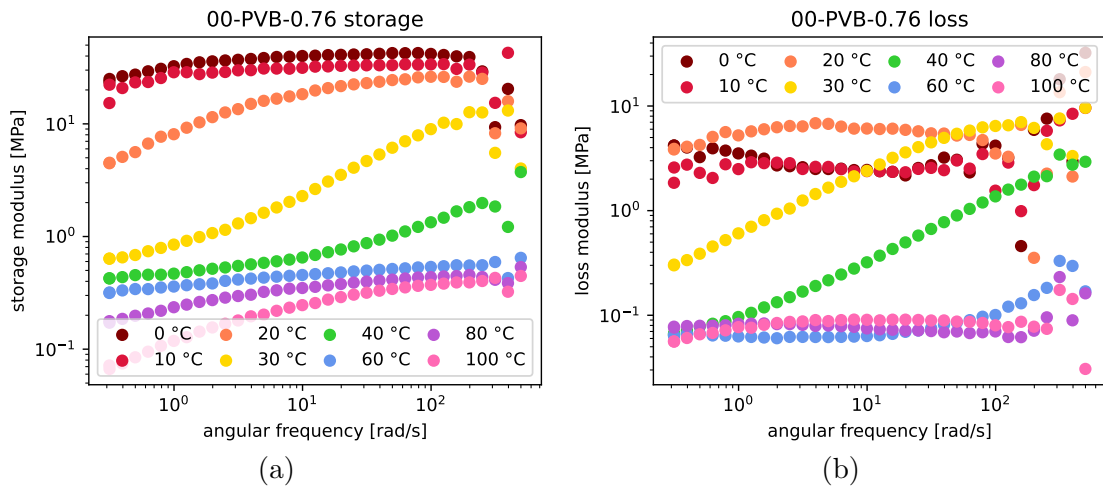

FIGURE 4.9: Experimental results on 0.76 mm PVB foil laminated at 140 °C
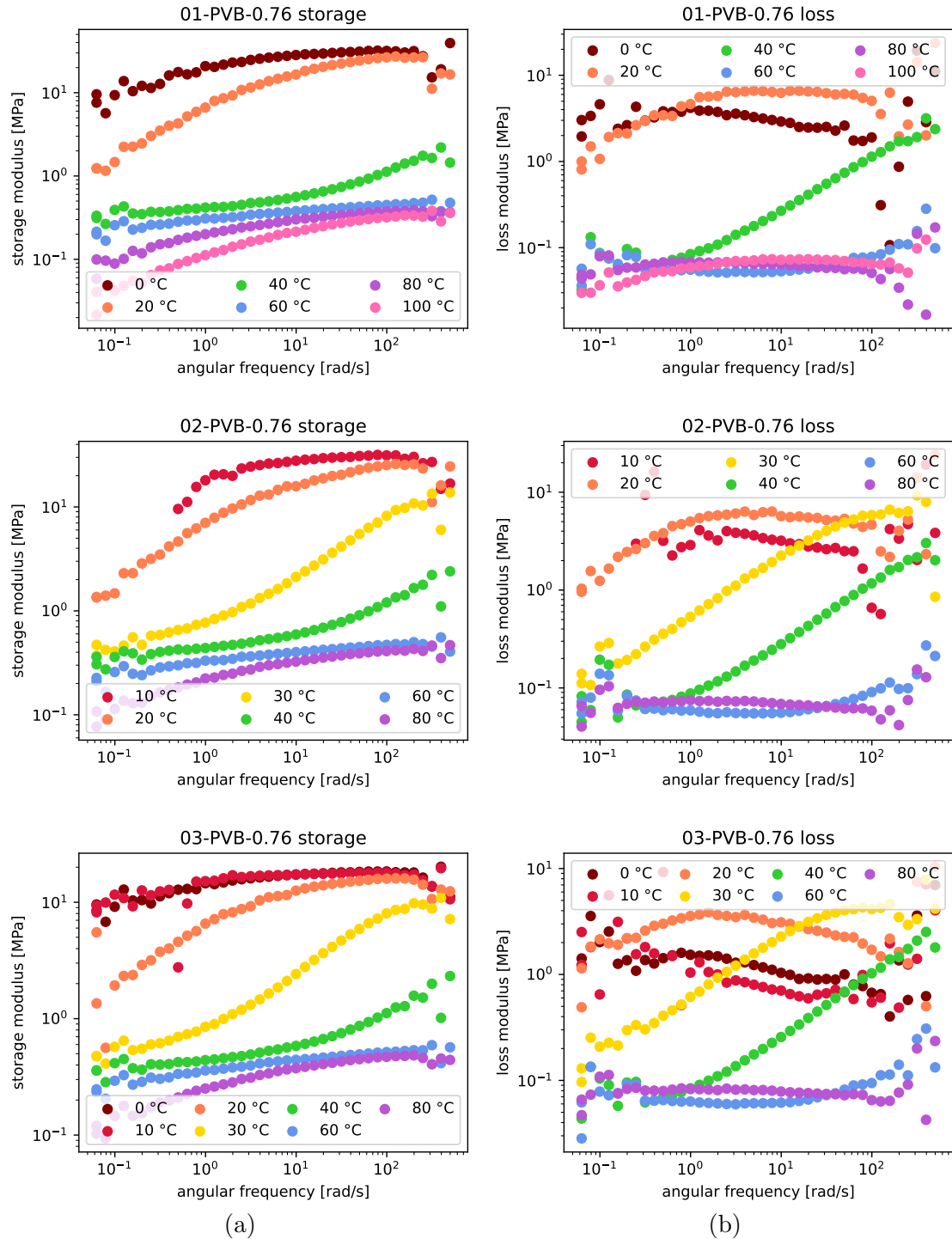(a) storage modulus, (b) loss modulus

FIGURE 4.10: Experimental results on 0.76 mm PVB foil
(a) storage modulus, (b) loss modulus

From the graphs it is also significant that for frequencies over 200 rad/s (approximately 32 Hz) and under 0.2 rad/s (0.032 Hz) the results are very volatile and unreliable. This phenomenon is significant for every provided measurement result and therefore this range of frequencies is excluded from the following analysis. These deviations are even more significant for the loss modulus, especially for the results obtained for low temperatures (say under 20 °C).

If we focus on the results for samples 02-PVB-0.76 and 02-PVB-1.52 we see that the measurements for 10 °C (marked red in the graphs) have not been completed. This can be attributed to overheating the rheometer. Theoretically, the device with its temperature chamber allows us to measure even for temperatures below zero. However, the limits of the cooling system are sometimes met much earlier.
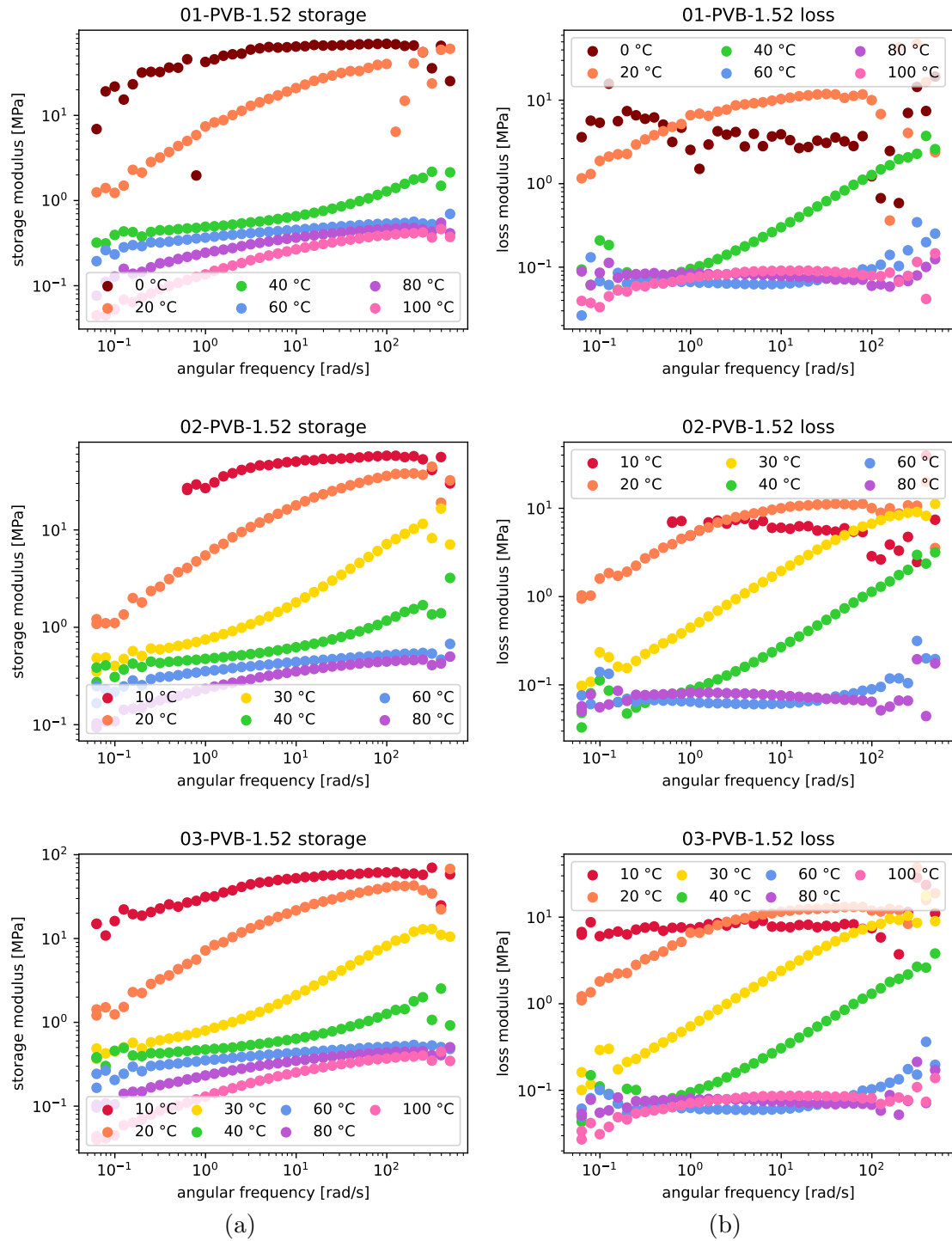

FIGURE 4.11: Experimental results on 1.52 mm PVB foil
(a) storage modulus, (b) loss modulus

When the results for the storage modulus are analyzed, it is obvious that the values of the modulus are higher for lower temperatures and vice versa. Therefore, response of the material is stiffer for lower temperatures and more compliant for higher temperatures. This phenomena is mostly noticeable for temperatures between 20-40 °C which is the reason why we added the intermediate temperature 30 °C to the measurement scenario. For this temperature range we also see the most significant dependence on frequency – for rapid loading (i.e. high frequencies) the material is stiffer then for slow loading (i.e. low frequencies). For temperatures under 10 °C and around 60 °C the frequency dependence is less significant which refers to solid-like behaviour of the material for these temperatures.

As for the loss modulus, we see that the frequency dependence is mostly noticeable for temperatures between 20-40 °C as well. For other measured temperatures the results are almost constant over the frequency range. Temperature dependence of the loss modulus is also important. However, for temperatures in the range of 60-100 °C there is no significant difference and the values of the loss modulus are similar. With decreasing temperature the loss modulus initially increases. Nevertheless, in the range of temperatures between 0 and 10 °C we observe an opposite trend. The values of the modulus in this temperature range are lower than for 20 °C and for some measurements even for 30 °C, especially for higher frequencies.
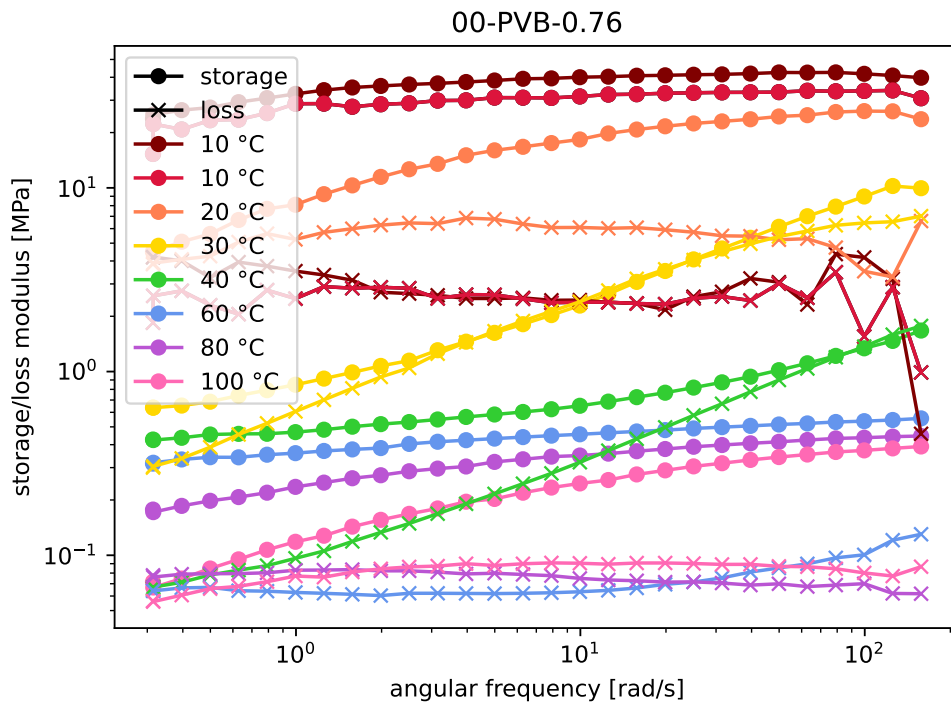

FIGURE 4.12: Experimentally obtained storage and loss moduli for sample 00-PVB-0.76

We know that the loss modulus describes the viscous response of the material while the storage modulus corresponds to the elastic part of the response. This was introduced in Chapter 2 analogously for the storage and loss stiffnesses. For $G' \gg G''$ the elasticity prevails and the material exhibits more solid-like behaviour. On the other hand, the liquid-like behaviour prevails for $G'' \gg G'$.

Figure 4.12 shows the correlation between the storage and loss moduli for sample labelled as 00-PVB-0.76 (the results for other samples are similar). For temperatures in the range of 0-10 °C and 60-80 °C we see the storage modulus significantly exceeding the loss modulus. Therefore, for these temperature ranges the behaviour of PVB is close to elastic. This statement is also indicated by the fact that for these temperatures the response is almost frequency-independent. For the temperature range between 20-40 °C and for 100 °C the values of the storage and loss moduli are closer to each other and the behaviour is more dependent on frequency. This indicates that for this temperature range the behaviour becomes more liquid-like and the viscosity is more significant.
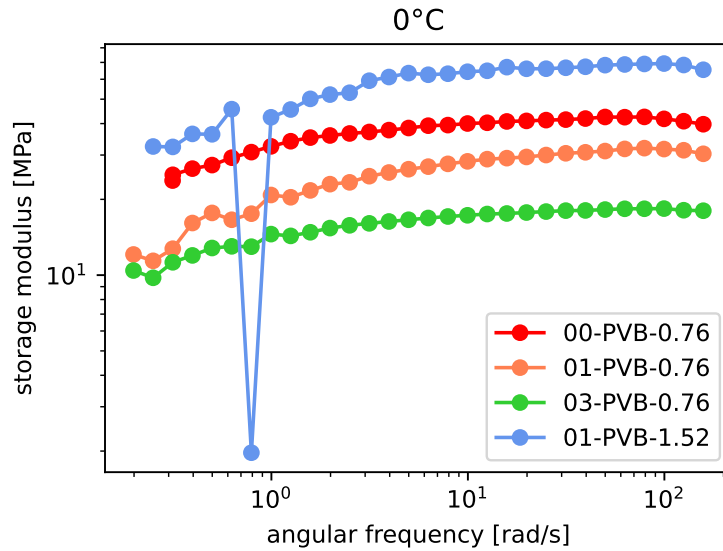

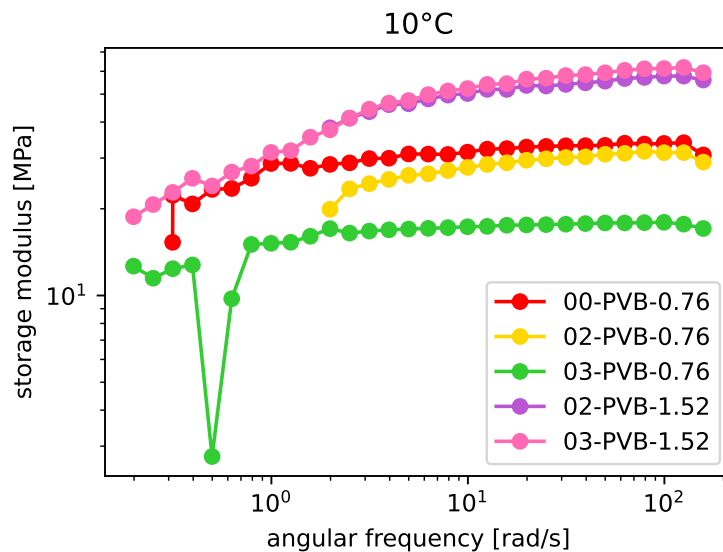FIGURE 4.13: Storage modulus at 0 °C measured for various samples

FIGURE 4.14: Storage modulus at 10 °C measured for various samples

Figures 4.13-4.16 compare the storage modulus for all of the examined samples measured at 0, 10, 20 and 60 °C, respectively. We can see a slightly different behaviour of the samples with different thicknesses. For 0 and 10 °C the samples with the thickness of 1.52 mm show a stiffer response than the 0.76 mm samples. For measurements at 20 °C this phenomenon is significant for high frequencies. For higher temperatures the

different behaviour between the two thicknesses is not frequency-dependent. A significant inconsistency in the measurements, evident particularly for thinner samples at low temperatures, is also worth mentioning. Similar conclusions apply also to the loss modulus. These observations were subsequently utilized in the evaluation and calibration procedures of the examined PVB foils described in subsequent sections.
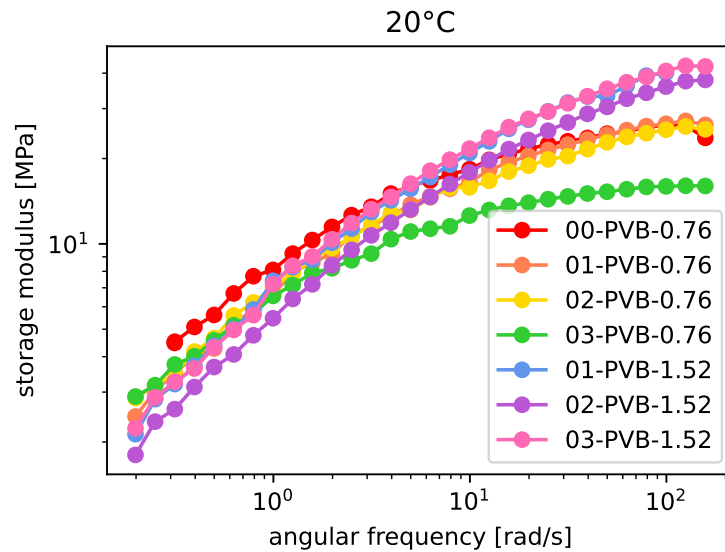

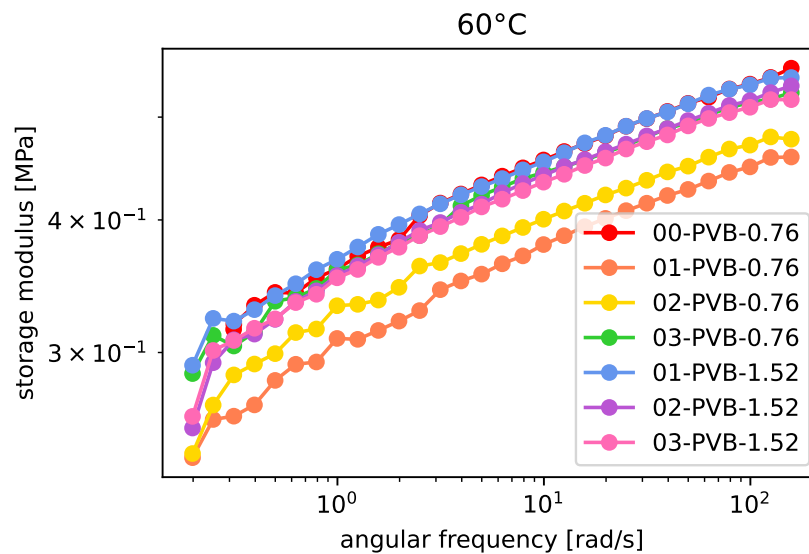FIGURE 4.15: Storage modulus at 20 °C measured for various samples

FIGURE 4.16: Storage modulus at 60 °C measured for various samples

The inconsistency in material behaviour for 0.76 and 1.52 mm samples is the reason why we decided that the following analysis will be provided separately for the two different thicknesses of the material. The average values of storage and loss moduli for both thicknesses of material obtained from the measurements are plotted in Fig. 4.17.

During the experimental analysis the material behaviour was investigated for the specified range of frequencies. The measurement limits for frequency are twofold, the limits given by the experimental apparatus and the time capabilities. The results presented in Figs. 4.9-4.11 clearly show inaccuracies distinctive especially for high frequencies, here

we meet the limits of the rheometer. On the other hand, extending the frequency range to lower frequencies would lead to disproportionate increase in the time required for a single measurement. Such obstacle can be overcome by exploiting the time(frequency)-temperature superposition principle, which allows us to extend the frequency domain beyond the measurement limits.
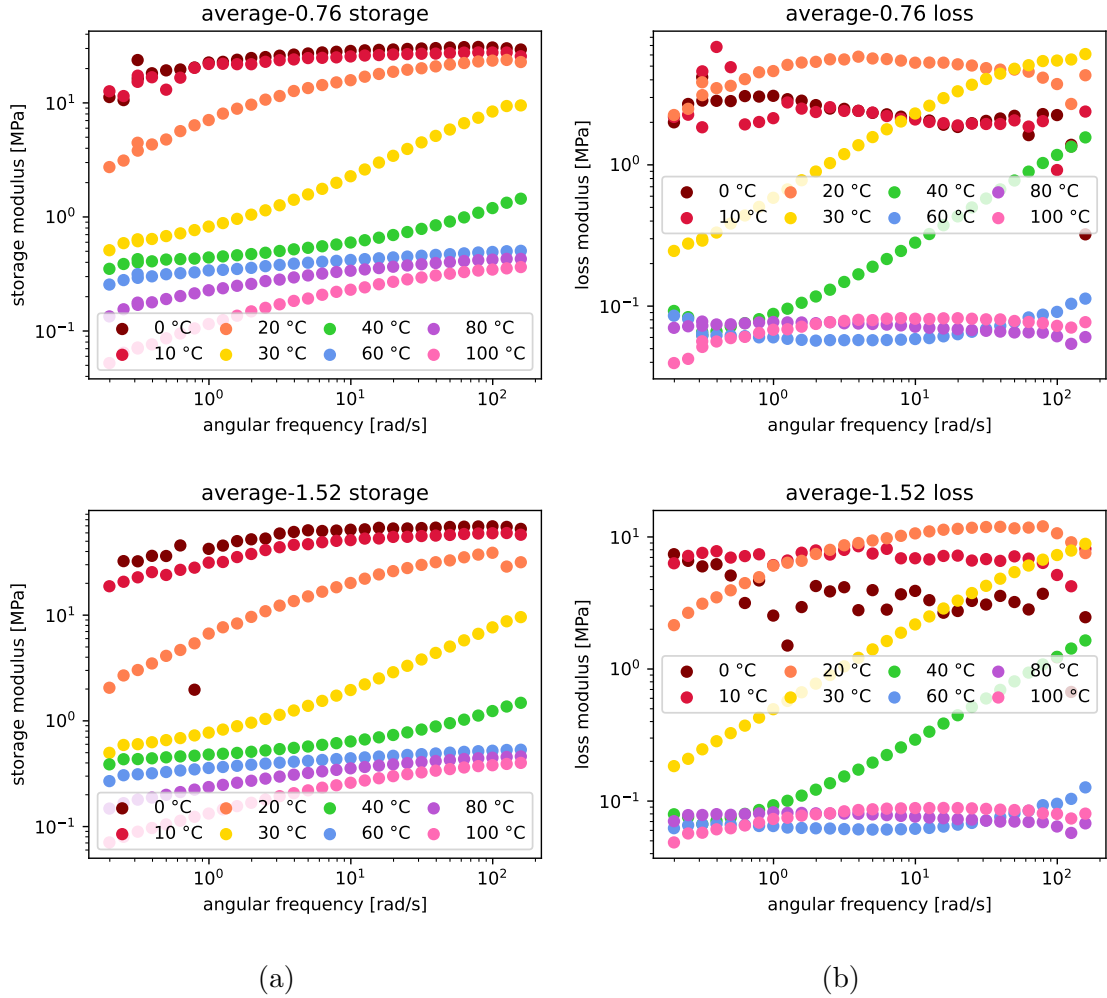

(a)   (b)

FIGURE 4.17: Average results for 0.76 mm and 1.52 mm PVB foil
(a) storage modulus, (b) loss modulus

4.2.1   Time-temperature superposition principle

From the results for storage and loss moduli we see that the response is stiffer for low temperatures and also for high frequencies (i.e. for rapid loading). On the other hand, response to loading at low frequencies is more compliant, as well as the response measured for higher temperatures. The time-temperature superposition principle assumes that the viscoelastic behaviour examined for one temperature can be related to the behaviour for another temperature when its timescale is changed [36]. In other words, from the set of measurements for various temperatures we can establish one temperature as a reference T_R and all of the measurements results can be related to T_R by changing their time (or, in our case, frequency) domain.
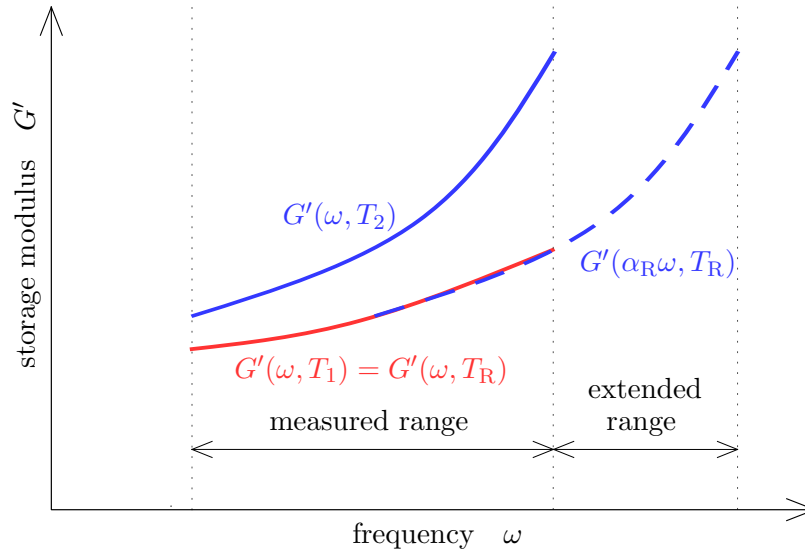
FIGURE 4.18: Time-temperature superposition principle

For example, we have the storage modulus G' depending on frequency ω and temperature T. The frequency and temperature can be bind by the shift factor α_R related to the reference temperature T_R. Since the reference temperature is set, the shifted function then depends on frequency only,

$$G'(\omega, T) \quad \rightarrow \quad G'(\alpha_R \omega, T_R). \tag{4.2}$$

The principle is schematically shown in Fig. 4.18 where the solid red and blue lines represent the data measured for two different temperatures. If we shift the solid blue line to the position of the dashed one we get one continuous curve. This result is related to the reference temperature set as $T_1 \equiv T_R$ and provides the extension of the measured range in the frequency domain. This extended curve for temperature T_R is called a mastercurve.

The shift is obtained by multiplying the original frequency range ω by the shift factor α_R which, in the logarithmic scale, results in a horizontal shift of the curve only. The shift factor depends on the original temperature T and it can be obtained from the Williams-Landel-Ferry (WLF) equation in the form [36]

$$\log \alpha_R(T) = \frac{-C_1(T - T_R)}{C_2 + T - T_R}, \tag{4.3}$$

where log denotes a decadic logarithm and C_1, C_2 are parameters that need to be found for the specific set of results so the shifting provides the smoothest possible mastercurve. The parameters are optimized based on the least squares method. The optimization compares the data points corresponding to the different temperatures and their deviations over the current overlapping region. If we have a set of measurements for more than two temperatures the whole set is then described by the same WLF equation and to find the optimal parameters C_1, C_2 all curves are exploited at once. The optimization was performed using the fminbnd function in MATLAB.

An illustrative example of the mastercurve fitting is shown in Fig. 4.19 for the average results measured on 1.52 mm sample. The grey dashed lines mark the measured frequency domain where we see the originally measured data for various temperatures.

The data marked by × are shifted relative to the reference temperature $T_R = 20$ °C with the optimized parameters of WLF equation $C_1 = 14.7231$, $C_2 = 120.7819$ °C. We see that the shift provide a significantly extended frequency domain.
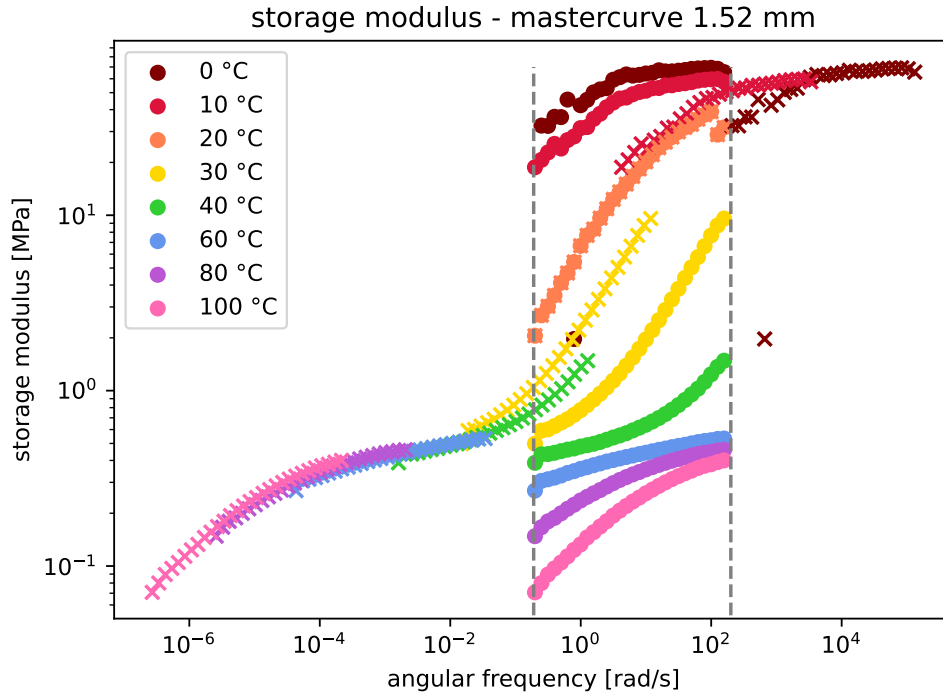

FIGURE 4.19: Example of mastercurve fitting

Figures 4.20-4.23 show the final mastercurves for the two different thicknesses of PVB (0.76 and 1.52 mm) for both the storage and loss moduli. The reference temperature T_R was set to 20 °C. The optimized parameters C_1, C_2 for each mastercurve are plotted in the corresponding graph.

As is shown in Figs. 4.20-4.21, the storage modulus yields reasonable results for both thicknesses of the material. The resulting mastercurves look as expected and we clearly see the trend in the frequency-dependent material behaviour. It should also be mentioned that in order to arrive at these results the optimization process adopted averages of the measurements being available at individual temperatures. As for the loss modulus, the results in Figs. 4.22-4.23 do not allow for constructing a sufficiently smooth mastercurves. To get better approximations it seems necessary to improve the optimization process for finding the shift factor parameters C_1 and C_2. Recall also the already discussed volatility of the results obtained for the loss modulus at low temperatures which calls for special attention to understand the acquired measurements. Both of these issues are, however, beyond the scope of this thesis. Therefore, our attention in further analyses is limited to the storage modulus only while understating the behaviour of the loss modulus is left for further research.

The resulting mastercurves in Figs. 4.20 and 4.21 are replotted in Fig. 4.24 and compared with the results obtained in [13] for the storage modulus extracted from the measurements performed directly on laminated-glass samples. We see that for frequencies under approximately 10^1 rad/s the results match well. A significant difference arises for higher frequencies where the storage modulus is lower for the PVB interlayer measured on the laminated glass samples. From the previous paragraphs we know that this extension of

the frequency domain was obtained by shifting the data measured at low temperatures. Nevertheless, the variability in behaviour for low temperatures (say lower than 20 °C) was observed even for our measurements for various PVB samples. Therefore, we may conclude that the different behaviour significant for high frequencies can be blamed on inconsistent results measured at low temperatures, recall Figs. 4.13-4.14.
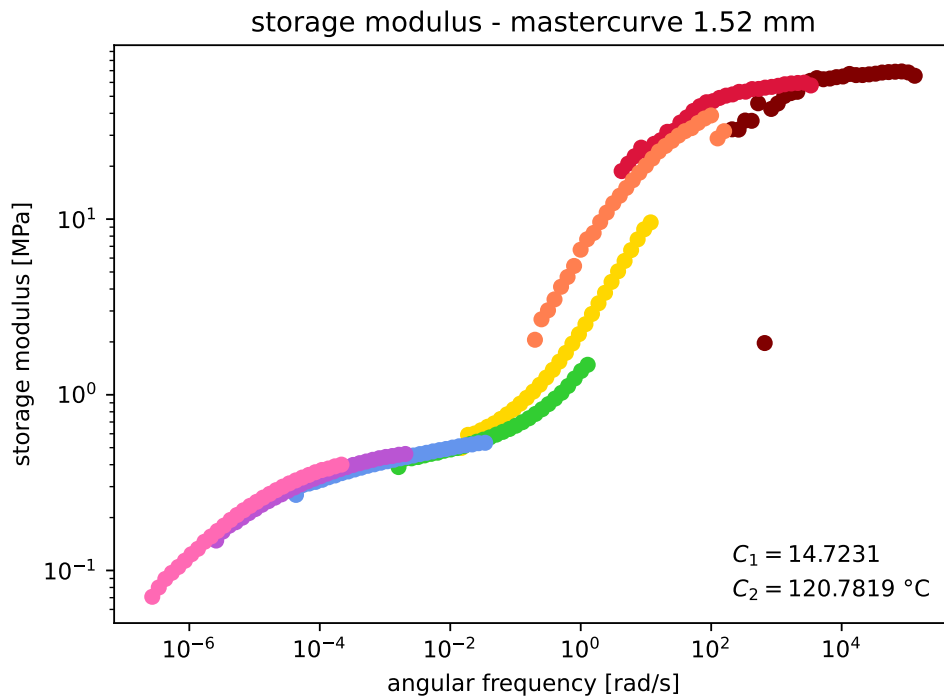

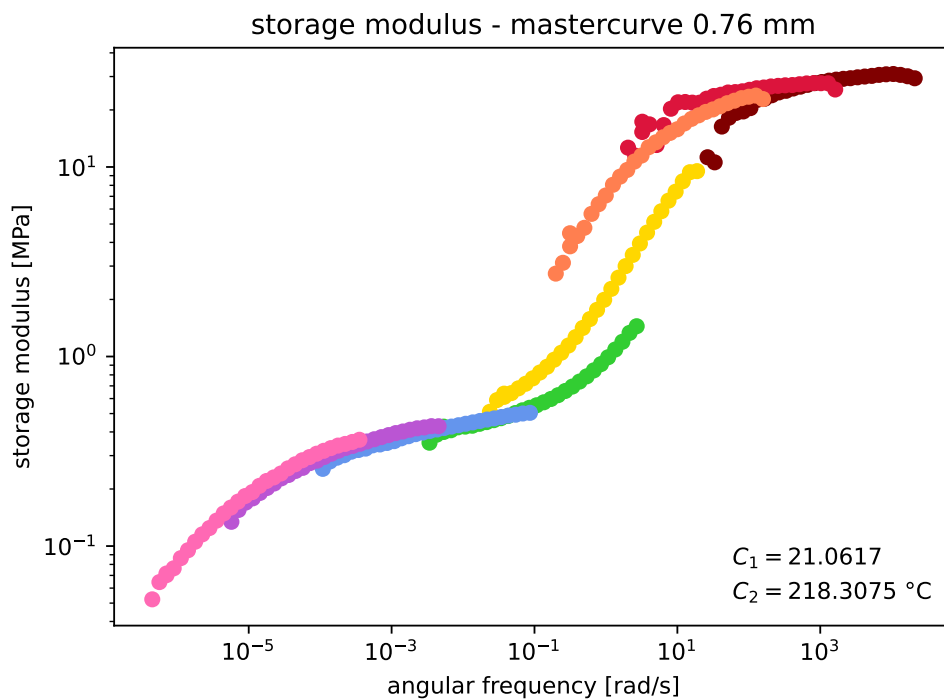FIGURE 4.20: Storage modulus mastercurve for 1.52 mm sample

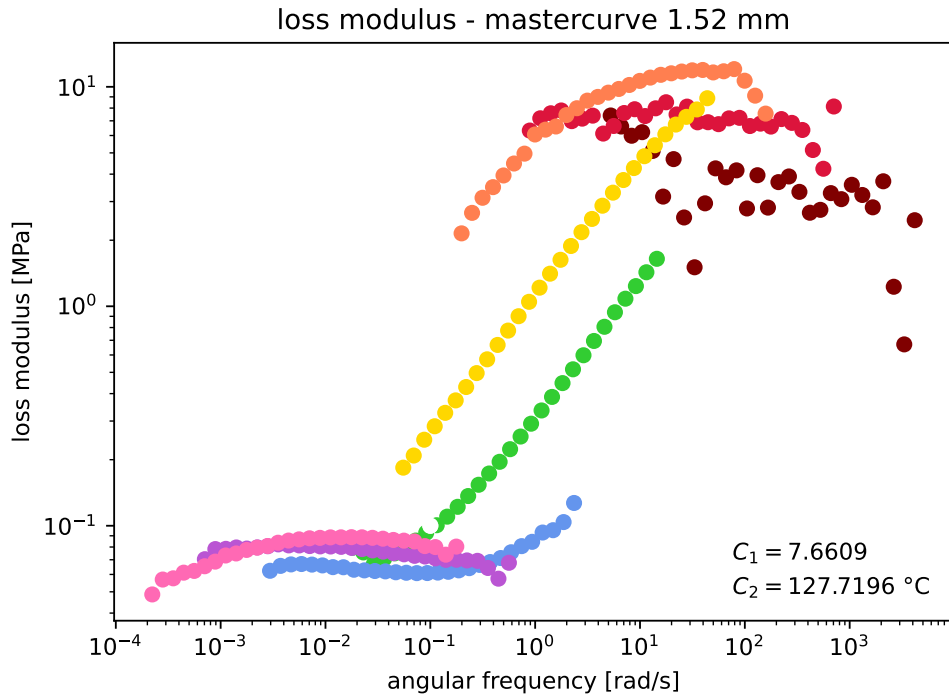FIGURE 4.21: Storage modulus mastercurve for 0.76 mm sample

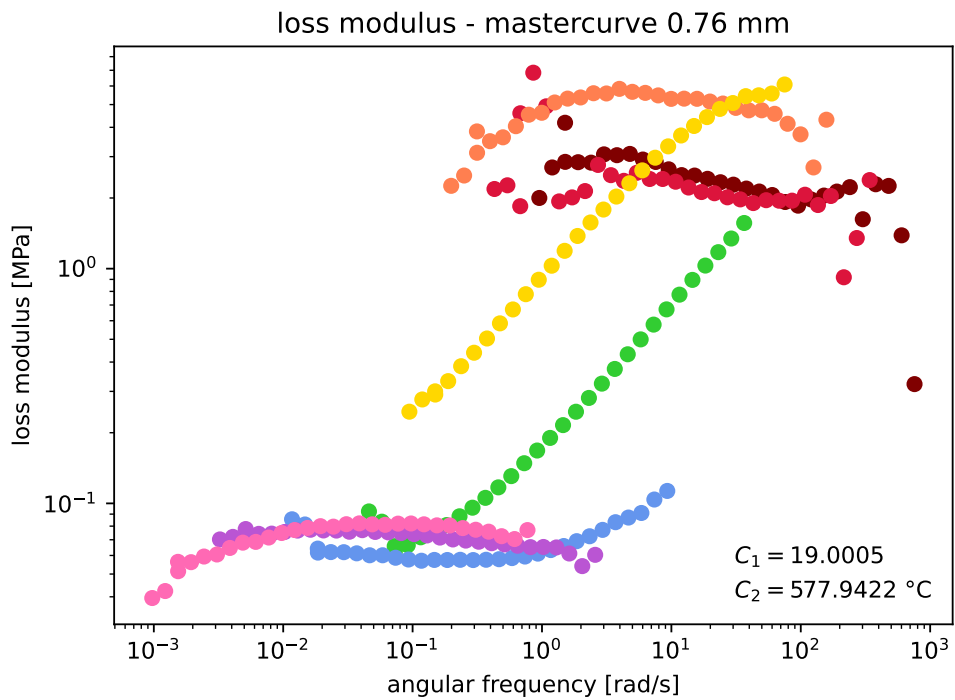FIGURE 4.22: Loss modulus mastercurve for 1.52 mm sample

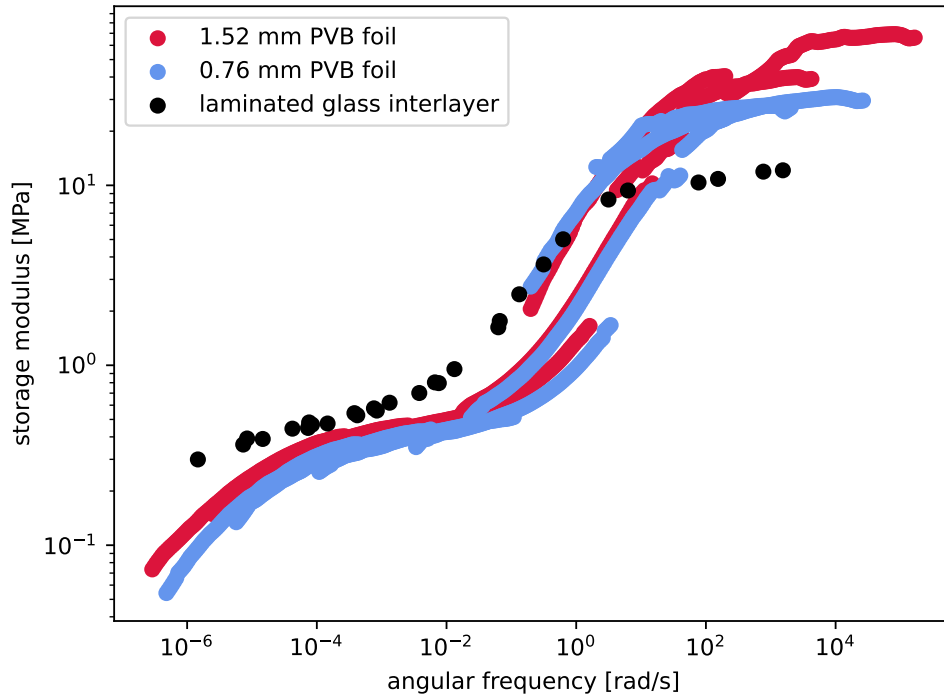FIGURE 4.23: Loss modulus mastercurve for 0.76 mm sample

FIGURE 4.24: Comparison of storage modulus obtained for PVB foil samples and for laminated glass samples with PVB interlayer, $T_R = 20$ °C

4.3 Calibration of theoretical models

In Chapter 3 we analyzed the material models under various loading conditions. The evolution of the load was prescribed, the response of the model was then expressed analytically or by a numerical algorithm obtaining the approximate solution in consecutive time steps. To determine the behaviour of the model we needed to know the analytical equations describing it (e.g. the Hooke law for the elastic model etc.). Both analytical and numerical solutions are based on known model parameters (such as stiffness k or characteristic time τ_c).

The data obtained from the rheometer experiment are given as a set of discrete values, i.e., no analytical description is available. Therefore, the data can not be directly used for further analysis of the material behaviour and must be first replaced with a suitable analytical function. In other words, we are looking for a theoretical model whose prediction would match the measured data.

In light of the previous section we continue to focus on the description of PVB interlayer by the Maxwell model. Again, its standard as well as fractional form is examined. In particular, the analytical functions describing their storage stiffnesses in dependence on frequency ω are derived, recall Eq. (2.90) for the standard Maxwell chain and Eq. (2.94) for the fractional Maxwell chain.

These expressions can be rewritten analogously for the storage modulus G' obtained from the measurements via dynamic shear rheometer. For the standard Maxwell chain we get

$$G'(\omega) = G_0 + \sum_{i=1}^{N} \frac{G_i \omega^2 \tau_{ci}^2}{\omega^2 \tau_{ci}^2 + 1}, \tag{4.4}$$

while for the fractional Maxwell chain the storage modulus has the following form

$$G'(\omega) = G_0 + \sum_{i=1}^{N} G_i \frac{(\tau_{ci}\omega)^{2\alpha_i} + (\tau_{ci}\omega)^{\alpha_i}\cos{(\alpha_i\frac{\pi}{2})}}{(\tau_{ci}\omega)^{2\alpha_i} + 2(\tau_{ci}\omega)^{\alpha_i}\cos{(\alpha_i\frac{\pi}{2})} + 1}. \tag{4.5}$$

In these expressions G_0 stands for the elastic shear modulus of the single spring and G_i represents the elastic shear modulus of the i-th Maxwell cell, α_i is the springpot parameter of the i-th fractional Maxwell cell.

These analytical functions are dependent on several free parameters. The number of parameters depends on the number of connected Maxwell cells. The unknown parameters include the elastic modulus of the single spring G_0 together with the elastic modulus G_i, and the characteristic time τ_{ci} associates with each Maxwell cell. For each fractional Maxwell cell the springpot parameter α_i needs to be determined as well. We thus have one free parameter for the single spring and two more for each standard Maxwell cell, whereas three more parameters are available for each fractional Maxwell cell connected in the chain. The analysis presented in Chapter 3 showed how the model behaviour depends on the parameters. Therefore, these free parameters need to be calibrated based on the experimental results to fit the behaviour of the real material.

To calibrate the model we employ the data presented in Section 4.2.1 in the form of mastercurves, recall Figs. 4.20 and 4.21. The calibration is based on the minimization of the squares of residua between the measured data points and the analytical function prescribing the storage modulus for the generalized Maxwell model for the corresponding frequency ω. To begin, the number of Maxwell cells connected in the chain is first selected. Next, the characteristic times of individual Maxwell cells τ_{ci} are suitably chosen. The mentioned least square method is then utilized to fit the remaining parameters (G_0, G_i for the standard Maxwell chain and G_0, G_i, α_i for the fractional one).

4.3.1 Standard Maxwell chain

The number N of Maxwell cells connected in the model should respect the frequency range that we need to describe. We consider the extended frequency range given by the mastercurves and therefore in our case the range of interest is approximately $10^{-6} - 10^5$ rad/s. Figure 4.25 shows the calibration of the chain with three standard Maxwell cells to describe the experimentally obtained storage modulus for 1.52 mm sample. The characteristic times were, for illustrative purposes, set to $\tau_{c1} = 10^{-2}$, $\tau_{c2} = 10^0$, $\tau_{c3} = 10^6$. The optimized model parameters can be found in Tab. 4.2. We see that the experimentally obtained data are approximated well for the frequencies found in the vicinity of $1/\tau_{ci}$ while the approximation is less accurate for more distant frequencies.

Parameter	Value	Parameter	Value
G_0	0.0632 MPa	G_2	13.3258 MPa
G_1	38.7819 MPa	G_3	0.1273 MPa

TABLE 4.2: Parameters of 3-cells standard Maxwell chain – 1.52 mm sample, fitting to experimental data
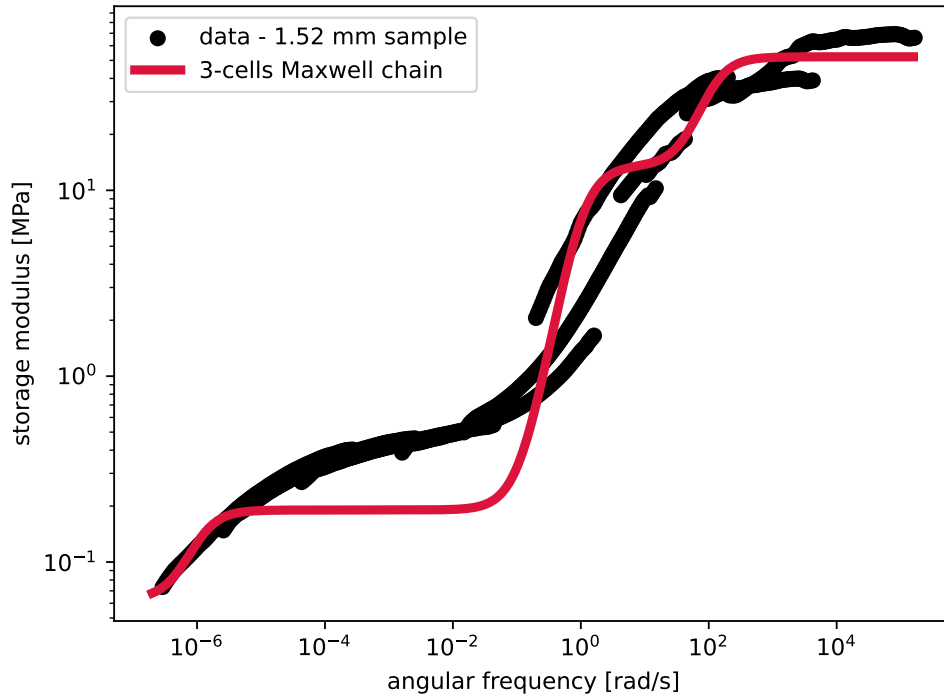
FIGURE 4.25: Calibration of 3-cells standard Maxwell chain to 1.52 mm sample

According to this behaviour, it seems reasonable to add one Maxwell cell per each decade in the range of frequencies we want to describe and set the values of the characteristic time accordingly. For our model in particular, the number of cells was set to 12 and their characteristic times were uniformly distributed according to

$$\tau_{ci} = 10^j, \quad j = \{-5, \, -4, \, \ldots, \, 6\}, \quad N = 12.$$

The remaining parameters of this 12-cells standard Maxwell chain were then optimized again exploiting the experimentally obtained mastercurves in Figs. 4.20 and 4.21. As suggested in the previous section, the calibration was performed separately for the two studied thicknesses of the PVB material. The optimized parameters for each of the two variants are summarized in Tabs. 4.3 - 4.4. Ability of the models to approximate the experimental data is then shown in Figs. 4.26 and 4.27.

Parameter	Value	Parameter	Value
G_0	0.04625 MPa	G_7	0.8527 MPa
G_1	0.0263 MPa	G_8	4.1315 MPa
G_2	0.09625 MPa	G_9	20.6808 MPa
G_3	0.1266 MPa	G_{10}	9.743 MPa
G_4	0.09871 MPa	G_{11}	15.327 MPa
G_5	0.06262 MPa	G_{12}	18.5988 MPa
G_6	3.534e-11 MPa		

TABLE 4.3: Parameters of standard Maxwell chain – 1.52 mm sample, fitting to experimental data
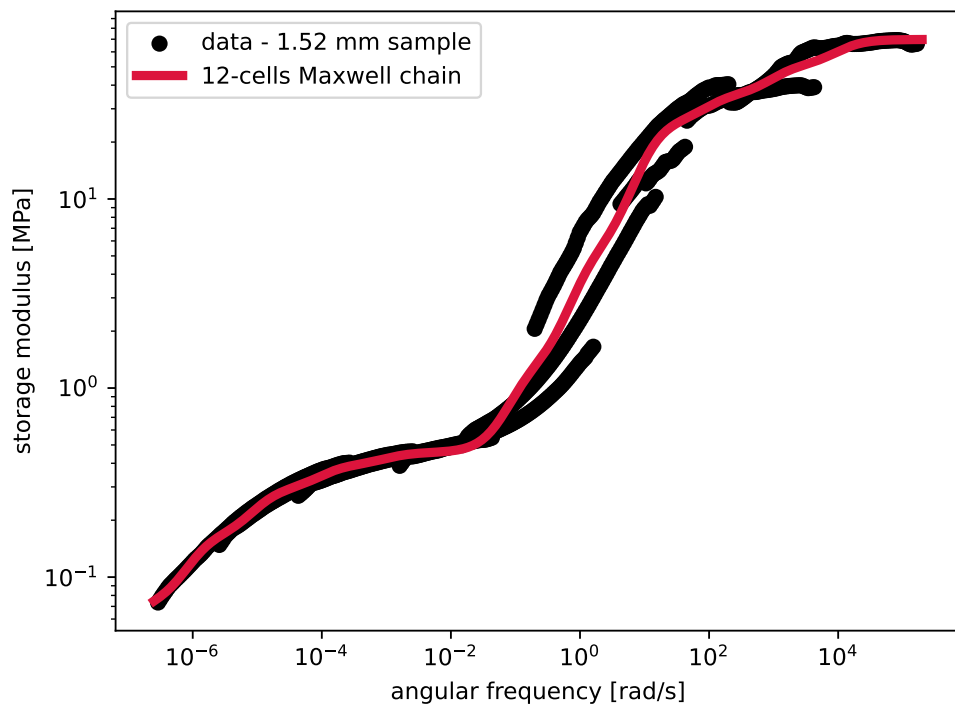
FIGURE 4.26: Approximation of the data for 1.52 mm sample by 12-cells standard Maxwell chain with model parameters according to Tab. 4.3
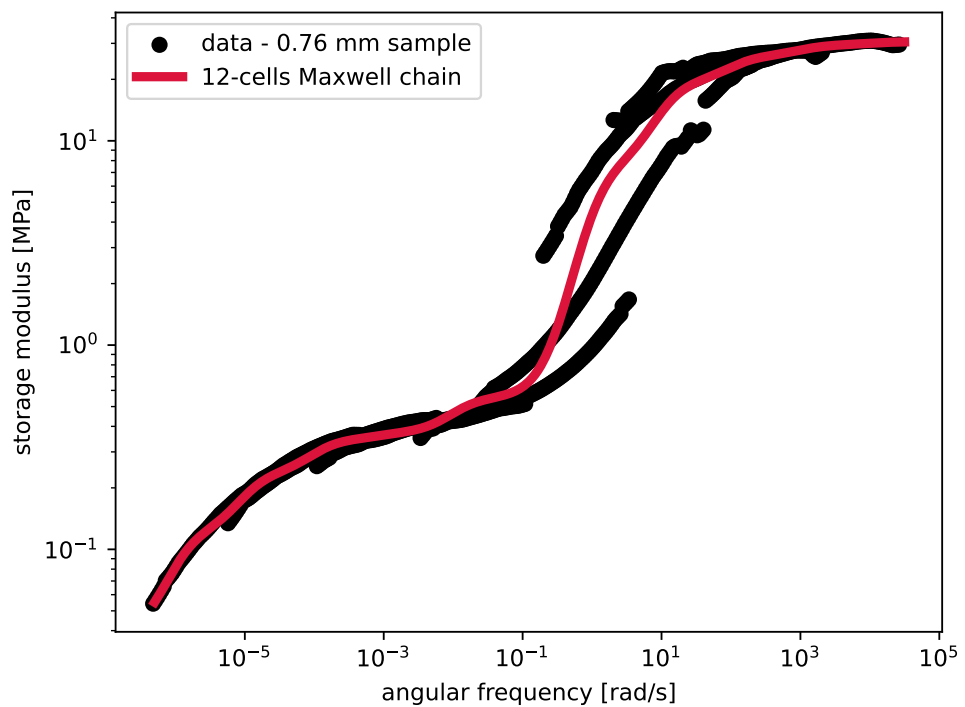

FIGURE 4.27: Approximation of the data for 0.76 mm sample by 12-cells standard Maxwell chain with model parameters according to Tab. 4.4

Parameter	Value	Parameter	Value
G_0	0.03733 MPa	G_7	1.139e-07 MPa
G_1	2.067e-07 MPa	G_8	7.309 MPa
G_2	0.0870 MPa	G_9	11.9472 MPa
G_3	0.1149 MPa	G_{10}	6.3631 MPa
G_4	0.1101 MPa	G_{11}	3.401 MPa
G_5	0.02511 MPa	G_{12}	1.0174 MPa
G_6	0.1788 MPa		

TABLE 4.4: Parameters of standard Maxwell chain – 0.76 mm sample, fitting to experimental data

4.3.2 Fractional Maxwell chain

For the fractional Maxwell chain the characteristic times were also set accordingly to the examined range of frequencies. The chosen values respect the course of the mastercurves, they correspond to the frequencies where the slope of the curve changes. Therefore, the characteristic times were set as

$$\tau_{ci} = 10^j, \quad j = \{-1.5,\ 1,\ 5\}, \quad N = 3,$$

for the material thickness 1.52 mm. For 0.76 mm the characteristic times are set as follows

$$\tau_{ci} = 10^j, \quad j = \{-1,\ 1,\ 5\}, \quad N = 3.$$

The optimized model parameters of the fractional Maxwell chain are summarized in Tabs. 4.5 and 4.6. The approximations of the two data sets are then plotted in Figs. 4.28 and 4.29.
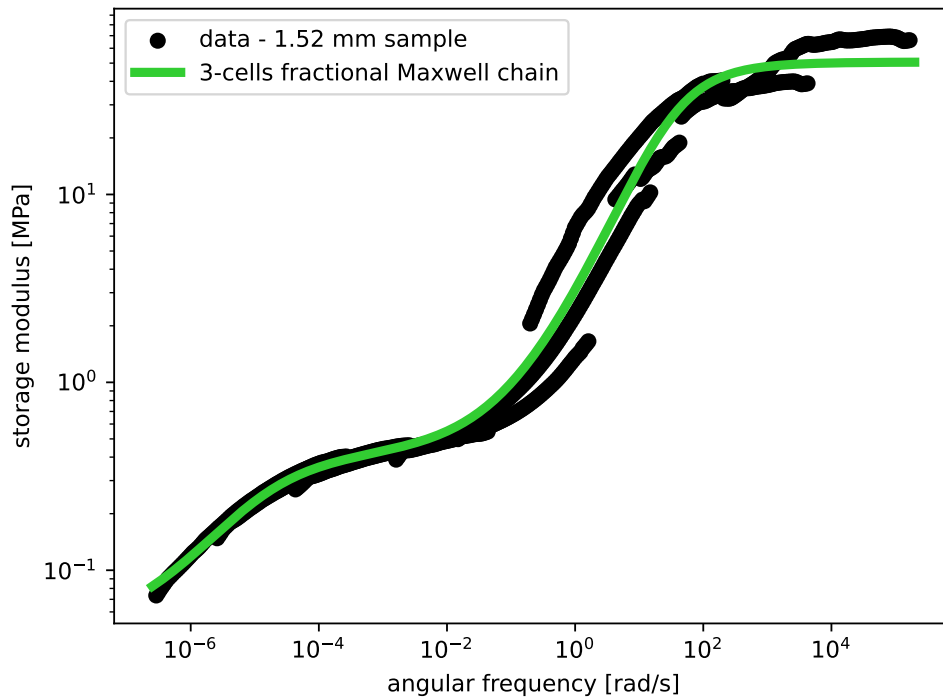

FIGURE 4.28: Mastercurve for 1.52 mm sample smoothed using 3-cells fractional Maxwell chain, model parameters according to Tab. 4.5

Parameter	Value	Parameter	Value
G_0	0.0416 MPa	α_1	0.6713
G_1	50.1031 MPa	α_2	0.2161
G_2	0.1563 MPa	α_3	0.5368
G_3	0.3441 MPa		

TABLE 4.5: Parameters of fractional Maxwell chain – 1.52 mm sample, fitting to experimental data

Parameter	Value	Parameter	Value
G_0	0.007426 MPa	α_1	0.7043
G_1	25.7932 MPa	α_2	0.4625
G_2	0.05564 MPa	α_3	0.5241
G_3	0.3438 MPa		

TABLE 4.6: Parameters of fractional Maxwell chain – 0.76 mm sample, fitting to experimental data
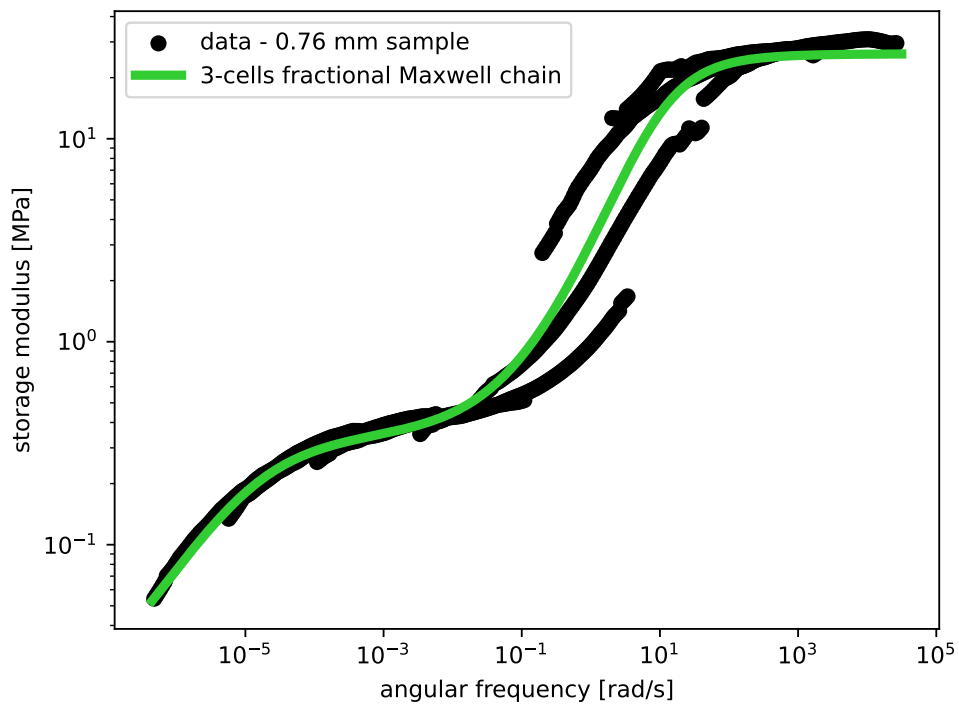

FIGURE 4.29: Mastercurve for 0.76 mm sample smoothed using 3-cells fractional Maxwell chain, model parameters according to Tab. 4.6

Comparing the resulting approximations given by the standard and fractional Maxwell chains clearly shows that the fractional model provides smoother results than the standard model. The number of optimized parameters also differs. While the standard Maxwell chain required 13 parameters to get an acceptable fit, the fractional model yielded suitable approximations for only 7 fitted parameters. We may thus conclude that the fractional model is able to give more accurate approximation in comparison to the standard model with even less parameters to be calibrated.

Nevertheless, it is fair to remember the principal drawback of the fractional model mentioned at the end of Chapter 3, which is associated with the computational time

considerably exceeding the time needed with the application of the standard model. This difference was found significant even for simple 1-cell models and short-timescale problems. Therefore, to solve more extensive problems using the numerical methods the fractional model seems inappropriate.

On the other hand, the fractional model has much better ability to approximate the experimentally obtained data. Smoothing and storing these data in terms of the fitted mastercure while adopting just a few Maxwell chains of the fractional model appears rather advantageous. Such a smooth approximation can be then adopted in the calibration of the standard Maxwell chain. The results of this specific process are shown in Figs. 4.30 and 4.31. In the graphs, the green line represents the behaviour of the fractional Maxwell chain calibrated to the experimentally obtained data (model parameters from Tabs. 4.5-4.6). The parameters of the standard Maxwell chain were then fitted to the green curve (the approximated mastercurve). The result is plotted by the red dashed line and the calibrated parameters are summarized in Tab. 4.7 for 1.52 mm thickness of PVB and in Tab. 4.8 for 0.76 mm thickness of PVB.

Parameter	Value	Parameter	Value
G_0	0.07857 MPa	G_7	0.9848 MPa
G_1	1.715e-05 MPa	G_8	2.561 MPa
G_2	0.08111 MPa	G_9	21.4533 MPa
G_3	0.148 MPa	G_{10}	21.4514 MPa
G_4	0.08325 MPa	G_{11}	2.5442 MPa
G_5	0.09585 MPa	G_{12}	0.9845 MPa
G_6	0.07371 MPa		

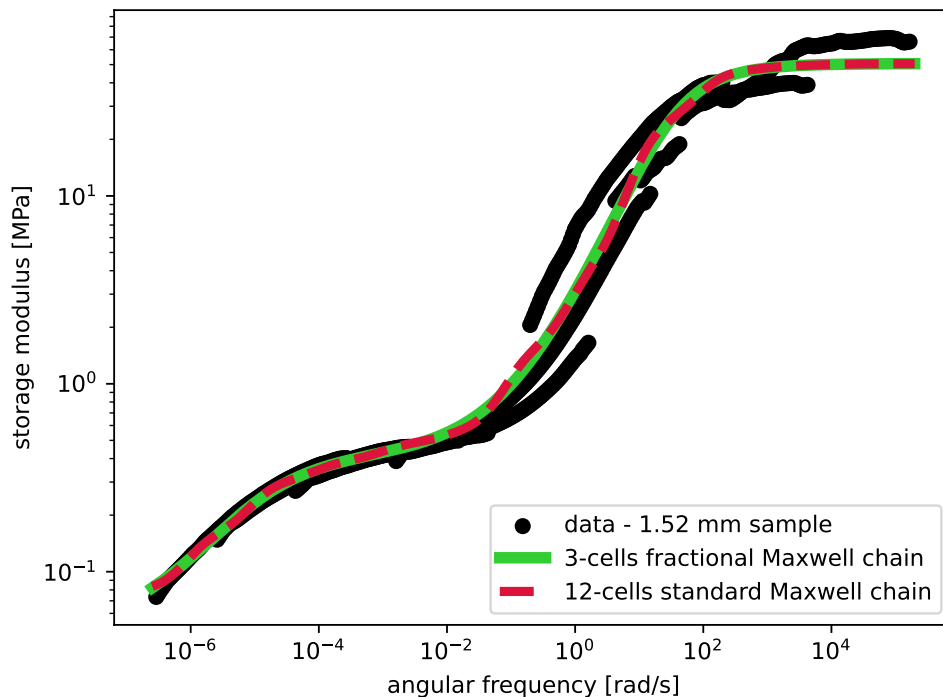TABLE 4.7: Parameters of standard Maxwell chain – 1.52 mm sample, fitting to smoothed mastercurve

FIGURE 4.30: Calibration of 12-cells standard Maxwell chain with model parameters according to Tab. 4.7

Parameter	Value	Parameter	Value
G_0	0.03521 MPa	G_7	0.3552 MPa
G_1	1.1985e-09 MPa	G_8	4.7239 MPa
G_2	0.08069 MPa	G_9	15.2745 MPa
G_3	0.1285 MPa	G_{10}	4.715 MPa
G_4	0.09079 MPa	G_{11}	0.3297 MPa
G_5	0.02009 MPa	G_{12}	0.2274 MPa
G_6	0.2267 MPa		

TABLE 4.8: Parameters of standard Maxwell chain – 0.76 mm sample, fitting to smoothed mastercurve
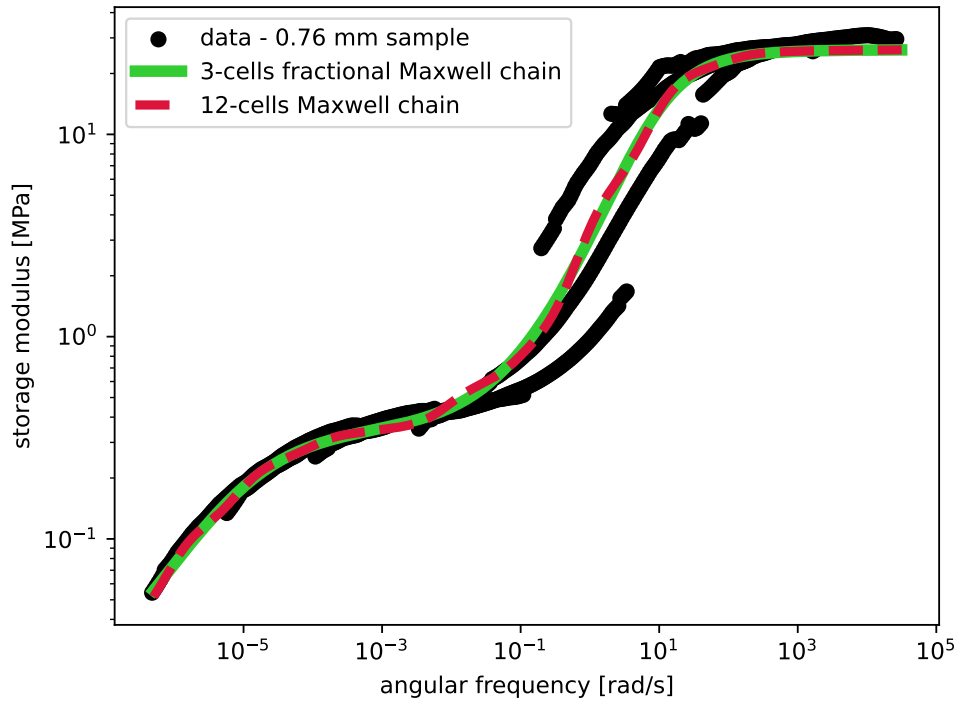

FIGURE 4.31: Calibration of 12-cells standard Maxwell chain with model parameters according to Tab. 4.8

Finally, Fig. 4.32 and 4.33 compare the storage modulus described by 12-cells standard Maxwell chain calibrated using the two different approaches. In particular, the blue line represents the model calibrated to the original mastercurve (the shifted raw data in Figs. 4.30 and 4.31), whereas the red line corresponds to the calibration based on the mastercurve smoothed by the fractional model (green lines Figs. 4.30 and 4.31). The results for the model calibrated to the smoothed mastercurve appear sightly better. On the other hand, both approaches deliver results which match fairly well for both thicknesses examined.
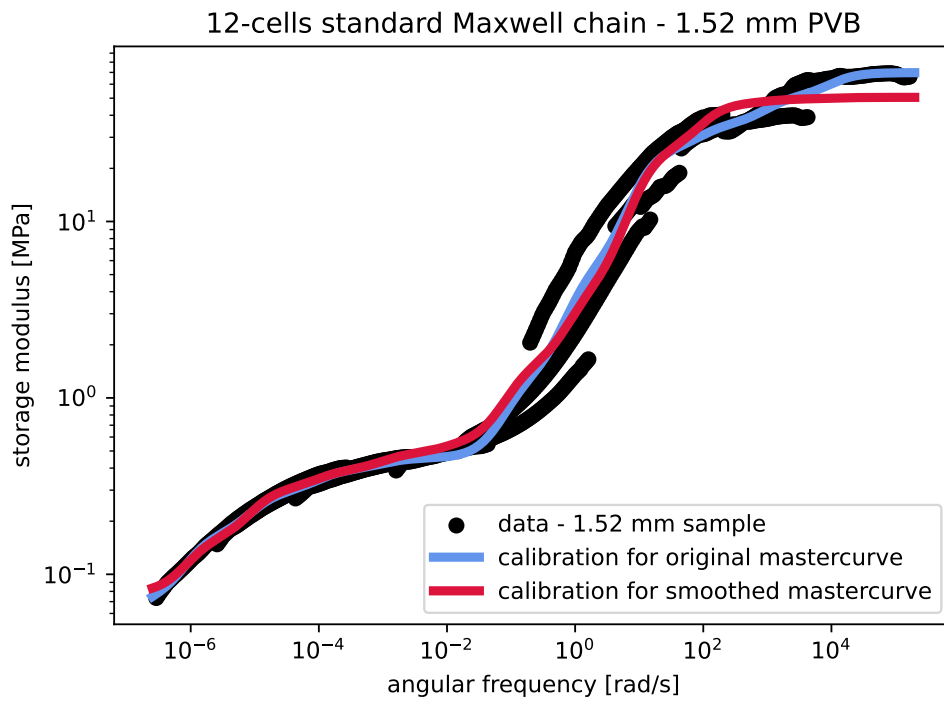
FIGURE 4.32: Calibration of 12-cells standard Maxwell chain – difference for calibration to original or smoothed mastercurve for 1.52 mm PVB
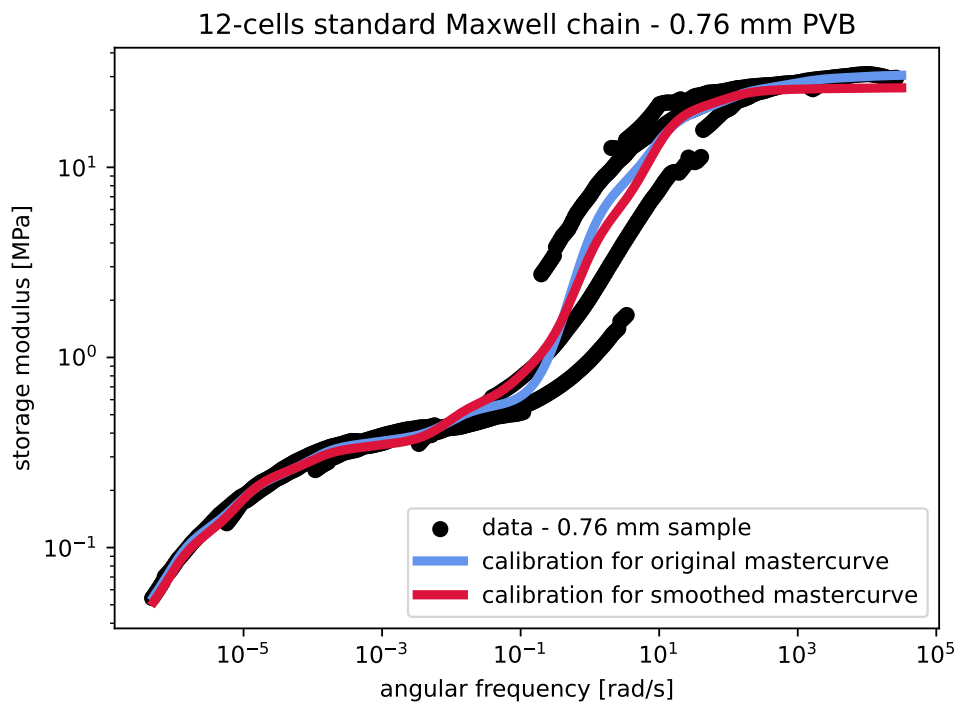

FIGURE 4.33: Calibration of 12-cells standard Maxwell chain – difference for calibration to original or smoothed mastercurve for 0.76 mm PVB

Chapter 5

Conclusions

This thesis provides a detailed description of viscoelastic materials with a specific focus on polyvinyl butyral (PVB). As was introduced in Chapter 1, PVB is a polymeric material used as an interlayer in the production of laminated glass. The interlayer ensures an interaction between the individual glass plates and it also has an important safety function. For theoretical modelling PVB is classified as a viscoelastic material. The viscoelastic material behaves somewhere between the two limit cases given by purely elastic solid and purely viscous liquid. Behaviour of the viscoelastic material is non-negligibly time dependent and phenomena such as creep and relaxation during the static loading or a phase shift of the response to the dynamic load are significant. Chapter 2 provides basic insight into the theory of viscoelasticity and introduces some of the theoretical models.

The two approaches which can be used for the description of the viscoelastic materials are compared in this thesis with emphases put on the behaviour within the limits of linear viscoelasticity. Standard viscoelasticity describes the material using the models consisting of elastic springs and viscous dashpots. This approach is more traditional and the material is usually described by the model with high number of parameters (such as stiffness or characteristic time). Fractional viscoelasticity then introduces the springpot element which behaves as viscoelastic itself. The springpot can be connected with other rheological elements as well to form even more complex theoretical models. The fractional viscoelasticity is based on the theory of derivatives and integrals of non-integer order. This approach, of course, requires more complicated mathematical background. However, the fractional viscoelasticity is able to describe the material behaviour more accurately while considerably reducing the number of model parameters compared to standard viscoelasticity.

Following the theoretical background provided in Chapter 2 we subsequently limited our attention to the generalized Maxwell model (or so-called Maxwell chain) in its standard and also its fractional form. These two models were subjected to a thorough numerical analysis described in Chapter 3. In this chapter several numerical algorithms were derived using the finite difference method. The models were exposed to various types of load and both the static and dynamic response was examined for varying parameters of the models. This endeavour confirmed the essential drawback associated with the fractional model which is the required computational time to be much longer in comparison to the standard model. This suggests that the fractional model might not be directly

applicable in large scale numerical analyses of real engineering structures such as glass laminates.

Regardless of the adopted formulation each theoretical model has several free parameters. To describe a specific material these parameters must be properly identified. This process is called the calibration of the model and is performed based on experimentally obtained behaviour of the material. For the purposes of this thesis the experimental analysis of PVB was carried out using a dynamic shear rheometer. This device loads the sample with harmonic torque and records the response including the amplitudes of the shear stress or strain and the phase shift between the applied load and the measured response. The experimental analysis is in detail discussed in Chapter 4. The measurements were performed on samples having two different thicknesses with the focus on frequency and temperature dependence of the material behaviour. The results were provided in the form of frequency-dependent storage and loss moduli for a set of temperatures.

The measured distributions were then adjusted applying the time-temperature superposition principle to generate the mastercurves relative to the selected reference temperature. The mastercurves provide extended frequency range in comparison to the measured range. While the measured storage modulus appears reasonable, the measurements associated with the loss modulus do not provide the expected behaviour especially at both tails of the selected frequency range. Because of that the loss modulus was omitted in further analyse s focusing solely on the storage modulus. The mastercurves obtained for the storage modulus were then used to calibrate the theoretical models as can be found at the end of Chapter 4. Nevertheless, the ambiguity in the experimental behaviour of the loss modulus might be an interesting topic of further research.

The calibration proved that the fractional Maxwell chain is able to approximate the measured data with significantly less parameters than the standard Maxwell chain. The fractional model can be also used to smooth the experimentally obtained mastercurve. The applicability of the fractional model can also be in the data storing since it is able to describe the material behaviour with only a few model parameters. When needed, the parameters of the standard Maxwell chain can be then calibrated to the smoothed curve provided by the fractional Maxwell model.

Appendix A

Brief introduction to fractional calculus

Fractional calculus is a branch of mathematics generalizing derivatives and integrals to non-integer order. There are multiple approaches and formulas defining the fractional derivatives or integrals. This appendix introduces only the necessary basics that were used for the purpose of this thesis. Interested parties can find more information for example in [28], [21] or [25].

A.1   Special functions

The Gamma function $\Gamma(x)$ plays a significant role in fractional calculus [28]. This function provides the continuous extension of the factorial function $n!$, $n \in \mathbb{N}$, see Fig. A.1. The Gamma function can be prescribed for positive values of $x \in \mathbb{R}$ as the Euler's integral

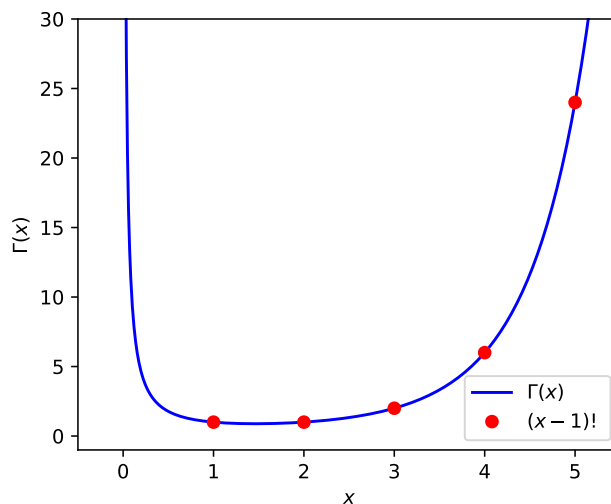$$\Gamma(x) = \int_0^\infty = \mathrm{e}^{-y} y^{x-1} dy. \tag{A.1}$$

FIGURE A.1: The Gamma function for positive values of x

For the purposes of this thesis it is appropriate to introduce some of the basic properties of the Gamma function:

$$\Gamma(x) = (x-1)!, \quad x \in \mathbb{N}, \tag{A.2}$$

$$\Gamma(1) = 1, \tag{A.3}$$

$$\Gamma(2) = 1, \tag{A.4}$$

$$\Gamma(1/2) = \sqrt{\pi}, \tag{A.5}$$

$$\Gamma(0) = \pm\infty, \tag{A.6}$$

$$\Gamma(x+1) = x\Gamma(x). \tag{A.7}$$

For broader information about the Gamma function see [2], [28].

The Mittag-Leffler function naturally occurs in the solutions of fractional differential equations [14]. This function generalizes the exponential function which can be written in the following form

$$\mathrm{e}^x = \sum_{k=0}^{\infty} \frac{x^k}{k!} = \sum_{k=0}^{\infty} \frac{x^k}{\Gamma(k+1)}. \tag{A.8}$$

Introduction of parameters $\alpha, \beta > 0$ leads to the generalization in the form of the Mittag-Leffler function

$$\mathrm{E}_{\alpha,\beta}(x) = \sum_{k=0}^{\infty} \frac{x^k}{\Gamma(\alpha k + \beta)}. \tag{A.9}$$

Some special cases of the Mittag-Leffler function are

$$\mathrm{E}_{1,1}(x) = \mathrm{e}^x, \tag{A.10}$$

$$\mathrm{E}_{0,1}(x) = \mathrm{E}_{0,2}(x) = \frac{1}{1-x}, \quad |x| < 1, \tag{A.11}$$

$$\mathrm{E}_{1,2}(x) = \frac{\mathrm{e}^x - 1}{x}. \tag{A.12}$$

To get more information of the Mittag-Leffler function see [14] or [10].

A.2 Fractional integrals and derivatives

The Riemann-Liouville fractional integral is the most common representation used to define fractional integral [21]. This definition is based on the Cauchy's formula for n-times repeated integration

$$I^n f(x) = \int_0^x \int_0^{x_1} \cdots \int_0^{x_n} f(x_n) \mathrm{d}x_n \cdots \mathrm{d}x_1 dx = \frac{1}{(n-1)!} \int_0^x (x-y)^{n-1} f(y) \mathrm{d}y, \tag{A.13}$$

where I^n denotes the integral operator of order $n \in \mathbb{N}$ [3]. The generalization of this formula for non-integer order integration is called the Riemann-Liouville fractional integral which can be written in the following form

$$I^\alpha f(x) = \frac{1}{\Gamma(\alpha)} \int_0^x (x-y)^{\alpha-1} f(y) \mathrm{d}y, \tag{A.14}$$

while this time I^n denotes the integral operator of non-integer order $\alpha \in \mathbb{R}$ and $\Gamma(\alpha)$ is the Gamma function [28], [23], [3].

Fractional derivative $D^\alpha f(x)$ is a linear operator. If α is integer, the fractional derivative of this order gives the same result as the classical one, zero-order fractional derivative $D^0 f(x) = f(x)$ [33]. There are more prescriptions for fractional derivative, we mostly meet the Riemann-Liouville formulation or the Caputo formulation. Both definitions are introduced in the following paragraphs.

The Caputo fractional derivative is prescribed in the form

$$D^\alpha f(x) = I^{\lceil\alpha\rceil - \alpha}\left[D^{\lceil\alpha\rceil} f(x)\right] \tag{A.15}$$

where $\lceil\alpha\rceil$ is the ceiling function, the least integer greater than or equal to α [11]. D^α then denotes the derivative of α-th order, $\alpha \in \mathbb{R}$ [3], [25].

After the substitution of Eq. (A.14) for $I^{\lceil\alpha\rceil - \alpha} f(x)$ we receive

$$D^\alpha f(x) = \frac{1}{\Gamma(\lceil\alpha\rceil - \alpha)}\int_0^x (x - y)^{\lceil\alpha\rceil - \alpha - 1}D^{\lceil\alpha\rceil} f(y)\mathrm{d}y. \tag{A.16}$$

In this thesis we further restrict to $\alpha \in \langle 0, 1\rangle$, $\lceil\alpha\rceil = 1$ and therefore Eq. (A.16) can be simplified to

$$D^\alpha f(x) = \frac{1}{\Gamma(1 - \alpha)}\int_0^x (x - y)^{-\alpha}\frac{\mathrm{d}}{\mathrm{d}y} f(y)\mathrm{d}y. \tag{A.17}$$

The Riemann-Liouville fractional derivative is prescribed as

$$D_{\mathrm{RL}}^\alpha f(x) = D^{\lceil\alpha\rceil}\left[I^{\lceil\alpha\rceil - \alpha} f(x)\right]. \tag{A.18}$$

Substituting the Riemann-Liouville fractional integral (Eq. (A.14)) for $I^{\lceil\alpha\rceil - \alpha} f(x)$ leads to the following expression

$$D_{\mathrm{RL}}^\alpha f(x) = \frac{1}{\Gamma(\lceil\alpha\rceil - \alpha)}D^{\lceil\alpha\rceil}\int_0^x (x - y)^{\lceil\alpha\rceil - \alpha - 1} f(y)\mathrm{d}y, \tag{A.19}$$

which can be further simplified for $\alpha \in \langle 0, 1\rangle$, $\lceil\alpha\rceil = 1$ to

$$D_{\mathrm{RL}}^\alpha f(x) = \frac{1}{\Gamma(1 - \alpha)}\frac{\mathrm{d}}{\mathrm{d}x}\int_0^x (x - y)^{-\alpha} f(y)\mathrm{d}y. \tag{A.20}$$

For the purposes of this thesis the Caputo fractional derivative was used. The main advantage of the Caputo formulation is that the initial or boundary conditions prescribed for the differential equation with the Caputo fractional derivative are prescribed as integer-order derivatives and therefore the physical interpretation is clear [33].

Appendix B

Laplace transform

The Laplace transform is a tool used for solving differential equations. It allows us to convert the fractional differential equation into elementary algebraic equation that is simple to solve. The solution of the original differential equation is then obtained by the inverse Laplace transform [30]. To solve the differential equation $f(t)$ the following procedure is used

$$f(t) \rightarrow \mathcal{L}\{f(t)\} = \bar{f}(s) \rightarrow \text{solve } \bar{f}(s) \rightarrow \mathcal{L}^{-1}\{\bar{f}(s)\} = f(t), \tag{B.1}$$

where $\mathcal{L}$ denotes the Laplace operator and $\bar{f}(s)$ is transformed equation.

The Laplace transform of function $f(t)$ is defined as

$$\mathcal{L}\{f(t)\}(s) = \int_0^\infty f(t)\mathrm{e}^{-st}\mathrm{d}t = \bar{f}(s), \tag{B.2}$$

where e is the Euler constant. The Laplace operator follows the linearity and therefore it holds that

$$\mathcal{L}\{c_1 f_1 + c_2 f_2\} = c_1 \mathcal{L}\{f_1\} + c_2 \mathcal{L}\{f_2\}. \tag{B.3}$$

An important property is that two distinct continuous functions have distinct Laplace transforms [30].

For the purposes of this thesis it is appropriate to introduce the Laplace transform of the Heaviside step function $H(t)$ as

$$\mathcal{L}\{H(t)\} = \frac{1}{s}, \tag{B.4}$$

and the Laplace transform of the Mittag-Leffler function, see Appendix A, in the form [18]

$$\mathcal{L}\{t^{\beta-1}\mathrm{E}_{\alpha,\beta}(\lambda t^\alpha)\} = \frac{s^{\alpha-\beta}}{s^\alpha - \lambda}. \tag{B.5}$$

The Laplace transform of the Riemann-Liouville fractional integral, see Eq. (A.14), is then introduced in [23] in the following form

$$\mathcal{L}\{I^\alpha f(t)\} = s^{-\alpha}\bar{f}(s). \tag{B.6}$$

Bibliography

[1] Laura Andreozzi, Silvia Briccoli Bati, Mario Fagone, Giovanna Ranocchiai, and Fabio Zulli. Dynamic torsion tests to characterize the thermo-viscoelastic properties of polymeric interlayers for laminated glass. *Construction and Building Materials*, 65:1–13, 2014.

[2] Richard A. Askey and Ranjan Roy. Gamma function., 2010.

[3] Leigh C. Becker and Ioannis K. Purnaras. Fractional relaxation equations and a cauchy formula for repeated integration of the resolvent. *Advances in the Theory of Nonlinear Analysis and its Application*, 2(1):11–32, 2018.

[4] Zdeněk Bittnar and Jiří Šejnoha. Numerické metody mechaniky 1. *Vydavatelství ČVUT, Praha ISBN*, 1992.

[5] Alessandra Bonfanti, Jonathan Louis Kaplan, Guillaume Charras, and Alexandre Kabla. Fractional viscoelastic models for power-law materials. *Soft Matter*, 16(26):6002–6020, 2020.

[6] John Charles Butcher. *Numerical methods for ordinary differential equations*. John Wiley & Sons, 2016.

[7] Libor Čermák. *Numerické metody pro řešení diferenciálních rovnic*. Litera Brno, 2013.

[8] James F. Epperson. *An introduction to numerical methods and analysis*. John Wiley & Sons, 2021.

[9] Aloyse J. Franck. Viscoelasticity and dynamic mechanical testing. *TA Instruments, New Castle, DE, USA AN004*, 1993.

[10] Rudolf Gorenflo, Francesco Mainardi, and Sergei Rogosin. Mittag-leffler function: properties and applications. *Handbook of fractional calculus with applications*, 1:269–296, 2019.

[11] Ronald L. Graham, Donald E. Knuth, Oren Patashnik, and Stanley Liu. Concrete mathematics: a foundation for computer science. *Computers in Physics*, 3(5):106–107, 1989.

[12] Robert M. Gresham. Viscosity: A fluid's resistance to flow. *Tribology & lubrication technology*, 64(11):55, 2008.

[13] Tomáš Hána, Tomáš Janda, Jaroslav Schmidt, Alena Zemanová, Michal Šejnoha, Martina Eliášová, and Miroslav Vokáč. Experimental and numerical study of viscoelastic properties of polymeric interlayers used for laminated glass: Determination of material parameters. *Materials*, 12(14):2241, 2019.

[14] Hans J. Haubold, Arak M. Mathai, Ram K. Saxena, et al. Mittag-leffler functions and their applications. *Journal of applied mathematics*, 2011, 2011.

[15] Barbora Hálková. Viskoelastic description of polymer interlayer of laminated glass. B.S. thesis, České vysoké učení technické v Praze. Vypočetní a informační centrum., 2022.

[16] Milan Jirásek and Jan Zeman. *Přetváření a porušování materiálů: dotvarování, plasticita, lom a poškození*. České vysoké učení technické v Praze, 2006.

[17] Piaras Kelly. Solid mechanics part i: An introduction to solid mechanics. *A Creative Commons Attributions, Mountain View, CA*, 94042, 2013.

[18] Li Kexue and Peng Jigen. Laplace transform and fractional differential equations. *Applied Mathematics Letters*, 24(12):2019–2023, 2011.

[19] Jamal Khatib. *Sustainability of construction materials*. Woodhead Publishing, 2016.

[20] Wilfried Laufs and Andreas Luible. Introduction on use of glass in modern buildings. Technical report, EPFL, Laboratoire de la construction métallique ICOM, 2003.

[21] J.L. Lavoie, R. Tremblay, and T.J. Osler. Fundamental properties of fractional derivatives via pochhammer integrals. In *Fractional Calculus and Its Applications: Proceedings of the International Conference Held at the University of New Haven, June 1974*, pages 323–356. Springer, 2006.

[22] D. Levy. Numerical differentiation. *University of Maryland*, 2010.

[23] Adam Loverro et al. Fractional calculus: history, definitions and applications for the engineer. *Rapport technique, Univeristy of Notre Dame: Department of Aerospace and Mechanical Engineering*, pages 1–28, 2004.

[24] Christian Lubich. Discretized fractional calculus. *SIAM Journal on Mathematical Analysis*, 17(3):704–719, 1986.

[25] Yuri Luchko. *Fractional Integrals and Derivatives:"True" versus "False"*. MDPI, 2021.

[26] Jiří Máca, Jaroslav Kruis, and Tomáš Krejčí. Dynamika stavebních konstrukcí: řešené příklady. *Praha: ČVUT*, 2015.

[27] Orlando Merino. A short history of complex numbers. *University of Rhode Island*, 2006.

[28] Keith Oldham and Jerome Spanier. *The fractional calculus theory and applications of differentiation and integration to arbitrary order*. Elsevier, 1974.

[29] Miloš Pirner. Dynamika stavebních konstrukcí. *Praha: SNTL*, 1989.

[30] Joel L. Schiff. *The Laplace transform: theory and applications*. Springer Science & Business Media, 1999.

[31] Jaroslav Schmidt. Experimental and numerical analysis of laminated glass under dynamic loading. Master's thesis, České vysoké učení technické v Praze. Výpočetní a informační centrum., 2018.

[32] Gebhard Schramm et al. *A practical approach to rheology and rheometry.* Haake Karlsruhe, 1994.

[33] Beata Sikora. Remarks on the caputo fractional derivative. *MINUT*, 5:76–84, 2023.

[34] TROSIFOL. Technical manual, The processing of Trosifol PVB film.

[35] Xing-er Wang, Jian Yang, Qing-feng Liu, Yang-mei Zhang, and Chenjun Zhao. A comparative study of numerical modelling techniques for the fracture of brittle materials with specific reference to glass. *Engineering Structures*, 152:493–505, 2017.

[36] Ian M. Ward and John Sweeney. *Mechanical properties of solid polymers.* John Wiley & Sons, 2012.

[37] Eric W. Weisstein. Euler formula. *https://mathworld. wolfram. com/*, 2004.

[38] Kevin Whitcomb. Determining the linear viscoelastic region in oscillatory measurements. *Application Note, TA Instruments, RH107*, 2022.